

## Review

# Physics of surface vibrational resonances: pillared phononic crystals, metamaterials, and metasurfaces

Yabin Jin<sup>1,\*</sup> , Yan Pennec<sup>2</sup> , Bernard Bonello<sup>3</sup> , Hossein Honarvar<sup>4,5,6</sup> , Leonard Dobrzynski<sup>2</sup> , Bahram Djafari-Rouhani<sup>2</sup>  and Mahmoud I Hussein<sup>4,5,\*</sup> 

<sup>1</sup> School of Aerospace Engineering and Applied Mechanics, Tongji University, 200092 Shanghai, People's Republic of China

<sup>2</sup> Institut d'Electronique, de Microélectronique et de Nanotechnologie (IEMN), UMR CNRS 8520, Université de Lille, 59650 Villeneuve d'Ascq, France

<sup>3</sup> Sorbonne Université, Faculté des Sciences, CNRS, Institut des Nanosciences de Paris (INSP), 75005 Paris, France

<sup>4</sup> Ann and H. J. Smead Department of Aerospace Engineering Sciences, University of Colorado Boulder, Colorado 80309, United States of America

<sup>5</sup> Department of Physics, University of Colorado Boulder, Colorado 80302, United States of America

<sup>6</sup> JILA, University of Colorado and NIST, Boulder, CO 80309, United States of America

E-mail: [083623jinyabin@tongji.edu.cn](mailto:083623jinyabin@tongji.edu.cn) and [mih@colorado.edu](mailto:mih@colorado.edu)

Received 11 July 2020, revised 15 December 2020

Accepted for publication 12 January 2021

Published 6 September 2021



CrossMark

## Abstract

The introduction of engineered resonance phenomena on surfaces has opened a new frontier in surface science and technology. Pillared phononic crystals, metamaterials, and metasurfaces are an emerging class of artificial structured media, featuring surfaces that consist of pillars—or branching substructures—standing on a plate or a substrate. A pillared phononic crystal exhibits Bragg band gaps, while a pillared metamaterial may feature both Bragg band gaps and local resonance hybridization band gaps. These two band-gap phenomena, along with other unique wave dispersion characteristics, have been exploited for a variety of applications spanning a range of length scales and covering multiple disciplines in applied physics and engineering, particularly in elastodynamics and acoustics. The intrinsic placement of pillars on a semi-infinite surface—yielding a metasurface—has similarly provided new avenues for the control and manipulation of wave propagation. Classical waves are admitted in pillared media, including Lamb waves in plates and Rayleigh and Love waves along the surfaces of substrates, ranging in frequency from hertz to several gigahertz. With the presence of the pillars, these waves couple with surface resonances richly creating new phenomena and properties in the subwavelength regime and in some applications at higher frequencies as well. At the nanoscale, it was shown that atomic-scale resonances—stemming from nanopillars—alter the fundamental nature of conductive thermal transport by reducing the group velocities and generating mode localizations across the entire spectrum of the constituent material well into the terahertz regime. In this article, we first overview the history and development of pillared materials, then provide a detailed synopsis of a selection of key

\* Author to whom any correspondence should be addressed.

Corresponding editor: Professor Masud Mansuripur.

research topics that involve the utilization of pillars or similar branching substructures in different contexts. Finally, we conclude by providing a short summary and some perspectives on the state of the field and its promise for further future development.

Keywords: surface vibrational resonance, pillared plate, pillared surface, phononic crystal, acoustic/elastic metamaterial, acoustic/elastic metasurface, nanophononic metamaterial

(Some figures may appear in colour only in the online journal)

## 1. General introduction

Light and sound are two key information carriers that provide physical platforms for vast opportunities for technological advancement [1–6]. In recent decades, we have witnessed a revolution in our ability to manipulate and control photons and phonons, respectively, through the design of functional material systems with properties that extend well beyond what is found in nature and in conventional materials. Inspired by an analogy with the quantum mechanical band theory of solids, in which electronic wave fields interact with a periodically arranged atomic lattice to form energy bands separated by band gaps [7], Yablonoitch [8] and John [9] proposed the concept of a *photonic crystal* in 1987. In a photonic crystal, the atoms are replaced by macroscopic media with differing dielectric constants and the periodic potential is replaced by a periodic dielectric function. The outcome was a new type of engineered material that exhibits photonic band gaps in which light is prevented from propagating in certain directions at specific frequency ranges. The notion of *phononic crystals* has then followed by further analogy. In contrast to electromagnetic waves, which only permit transverse polarization, elastic waves admit coupled longitudinal and transverse polarizations—a trait that makes the design of band gaps more challenging, but also provides a wider scope of opportunities for discovery and manipulation of new phenomena. The search for material structures with elastic band gaps and the concept of phononic crystals were independently proposed by Sigalas and Economou [10, 11] and by Kushwaha *et al* [12]. This added to earlier investigations of waves in periodic media in the structural dynamics community [13]. The material systems investigated exhibit partial and full band gaps for propagation of acoustic/elastic waves in periodic composites consisting of an array of inclusions placed in a background host medium, or a periodic arrangement of structural components. It is worth mentioning that the constituting media, either in the inclusions or in the background, may be a solid or a fluid (liquid or gas). While ‘fluid materials’ support only longitudinal modes, solid materials admit both longitudinal and shear waves [14]. Similarly, a periodic medium composed of interconnected structural components may comprise multiple phases.

The field has experienced a burst of interest following these discoveries and increasingly acquired a multidisciplinary

character involving both bulk and surface materials with engineering of features at the macroscale, microscale, and/or nanoscale. Now generally referred to as *phononics*<sup>7</sup>, this emerging field encompasses a wide range of interrelated disciplines including condensed matter physics, materials science, acoustics, mechanical engineering, and electrical engineering, among others. In more general terms, a phononic crystal is an artificial material consisting of a periodic inhomogeneous elastic medium that can manipulate the propagation of acoustic waves in fluids (or fluid-like solids) and elastic waves in solids. The propagation of acoustic/elastic waves in a phononic crystal is governed by *Bloch’s (or Floquet’s) theorem* (simply expressed as having the eigenstates of the Hamiltonian satisfy  $\psi(\mathbf{r} + \mathbf{R}) = e^{i\mathbf{k}\cdot\mathbf{R}}\psi(\mathbf{r})$ , where  $\mathbf{r}$ ,  $\mathbf{R}$ , and  $\mathbf{k}$  denote the position vector, lattice vector, and Bloch wave vector, respectively) [7]. This fundamental theorem provides the foundation to computing the band structure (dispersion relationship) over the *Brillouin zone* [15], which may be described as the primitive cell of the periodic medium expressed in reciprocal space [16]. Similar to photonic crystals, band gaps appearing in a phononic band structure represent frequency ranges where acoustic/elastic waves are prohibited from propagation and are instead attenuated. In periodic materials, the origin of a band gap is the well-known mechanism of *Bragg scattering*, which is based on destructive interferences of waves scattered by inclusions, holes, internal interfaces, etc, orderly arranged in a spatially repeated fashion. The underlying condition for this linear form of scattering is that the path difference between the interfering waves must be equal to an integer multiple of their wavelength [17]. Since the path difference depends on the lattice constant of a crystal, when the wavelength is comparable to the lattice constant, the Bragg scattering mechanism occurs.

In an alternate and fundamentally different mechanism, band gaps may form from the avoided crossing of two or more bands of the same symmetry, where at least one of the bands originates from a localized resonance mode of an individual particle, inclusion, or substructure. The emerging band gap in this case is termed a *local resonance* band gap or a

<sup>7</sup> Phononics has developed into a discipline with an established society, the International Phononics Society, and a biannual conference series, Phononics 20xx whose inaugural edition was Phononics 2011 in Santa Fe, New Mexico, May 29–June 2, 2011 (<http://phononics.org>) [370].

hybridization band gap<sup>8</sup>. This concept sparked the field of *acousticlelastic metamaterials*, and was first manifested by the proposition of ‘locally resonant sonic materials’ by Sheng and colleagues [19]. In parallel, a similar thrust emerged for resonant electromagnetic metamaterials initiated by Pendry *et al* [20] and demonstrated experimentally by Smith *et al* [21]. The first embodiment of an acoustic metamaterial took the form of a matrix of silicone-coated metallic spheres embedded in epoxy. Distinct from the Bragg scattering mechanism, the relevant wavelength corresponding to the lowest local resonance may be orders of magnitude larger than the size of the unit cell or the size of the resonating element; this in turn has opened the door for *low-frequency, subwavelength band gaps*. This in particular raised the opportunity of achieving sound isolation in the kilohertz range, while keeping the size of the unit cell reasonably small (of the order of a few centimeters). Indeed, with the acoustic velocities of common materials, the unit cell needs to be of the order of meters to pull a Bragg gap into the sonic regime. Some of the above concepts may be easily understood within the framework of simple academic models in one dimension as briefly described in section 2.1. The reader is referred to a collection of recent books [2–4, 6] and review articles [22–25] on this continuously growing field of research.

The prime focus of this review article is to present properties and functionalities of a unique type of phononic material proposed just over a decade ago consisting of a periodic array of pillars (or any form of standing substructures) on a plate or on a substrate [26, 27]. This configuration is characteristically a two-dimensional (2D) material, i.e. has a Brillouin zone that can be fully defined in two dimensions, with the branching pillars acting as the local resonators. Therefore, similar to Sheng’s bulk acoustic metamaterial, the mechanism of local resonance and hybridization gaps exists in a pillared 2D medium or surface. The concept also applies to a 1D medium or surface. Furthermore, Bragg band gaps may form as well due to the spatial periodicity of the placement of the pillars (see the simple models covered in section 2.1). Because of this dual aspect, material systems belonging to this class effectively behave both as phononic crystals and metamaterials, although the metamaterial aspect is in principle independent of periodicity. Furthermore, when the pillars lie on a surface, the outcome may be defined as an elastic metasurface. For example, a line of gradient pillars on a surface may be regarded as an elastic metasurface with the characteristic pillar diameter falling well within the subwavelength regime. When considering a reduced dimension material, i.e. 2D or 1D, the attachment of pillars or any similar form of branching substructure provides a practical way for the introduction of local resonators<sup>9</sup>; thus this topic practically encompasses the notion of reduced-dimension locally resonant acoustic and elastic

metamaterials. Since their proposition, a sizable body of work has been devoted to the investigation of this class of materials/surfaces/structures and their functionalities as described throughout this review. A general summary is given first as follows.

Pillared metamaterials with low-frequency band gaps were first studied by Pennec *et al* [26] and Wu *et al* [27] in 2008. In both studies, periodic plates with a single pillar in the unit cell were considered. It was reported that if one suitably chooses the geometric parameters of the pillar’s diameter and height, and the thickness of the plate on which it is supported, a low-frequency band gap may appear below the first Bragg band gap in the dispersion curves—this subwavelength band gap originates from an avoided crossing between a pillar’s local resonance mode and a dispersion branch (or more than one branch) of the plate. Low-frequency band gaps in the kilohertz [27–31] and megahertz [32] frequency ranges were subsequently experimentally validated. Since a low-frequency band gap depends on both the pillar’s mode and a plate’s mode involved in the coupling, a range of possibilities are available for modifying the geometric parameters or material composition to tune the properties of the band gap, especially its width. It is found that designing the connection between the pillars and the plate such that it consists of a relatively narrow neck [33, 34], a conic angle [35, 36], or a soft material such as rubber [37–42] allows us to shift the low-frequency gap downwards. These changes are effectively analogous to reducing the ‘stiffness’ in a branching mass–spring system, which may be used as an idealized model for studying the mechanism of local resonance band-gap formation [43–45]. The shapes of the deposited resonators (cylindrical pillar, square rod [46–50], sphere [51], spiral [52] or Gaussian surface [53]) and the lattice symmetry of the periodic arrangement (triangular [54–56], square [54–58], hexagonal [57], honeycomb [54, 58], hybrid [59, 60], or random [61, 62]) have direct impact on the properties of the engineered local resonance band gap, such as its width and position in the frequency domain. Having pillars on both sides of a plate provides an additional avenue for enriching the design space [63–67]. Given that local resonance behavior does not depend on periodicity, a hybridization band gap may appear in aperiodic or disordered systems [30, 61, 62]. Localized modes corresponding to low-frequency band gaps may be further synthesized by introducing hollow parts in the pillars [68–70]. Moreover, the band-gap width may be enhanced with multiconcentric hollow pillars [71, 72]. Filling the hollow pillars with a liquid enables the generation of solid–liquid coupling modes, which can be actively tuned by controlling the filling height [69, 73] and utilized toward the realization of tunable phononic circuits [74]. In addition to altering the design of the pillar(s), removal of material from the plate portion also provides an opportunity for performance enhancement and further broadening of the band-gap width, giving rise to the notion of a *trampoline metamaterial* [75] where the base acts as a springboard with reduced stiffness. The trampoline concept was pursued in a variety of settings and configurations [50, 52, 59, 70, 76–79]. Moreover, active tuning of band-gap properties is possible by an applied external magnetostatic field [49] or by shunted piezoelectric

<sup>8</sup> The shortened term ‘hybridization gap’ has also been widely used in the field of acoustic and elastic metamaterials [18] inspired by the use of the term in condensed matter physics.

<sup>9</sup> An alternative is to embed softly coated inclusions (as done in 3D bulk materials in reference [18]), soft inclusions [371], or concentrated masses in viscoelastic cavities [372] in the main body of the 2D or 1D material.

transducers [48, 80–85]. Similar to pillars on a plate, pillars on a substrate were also theoretically and experimentally investigated with a view on their local resonance band gaps [32, 86–91]. It is further reported that the number of elements in a phononic crystal can be reduced by designing a pillar-in-hole instead of a pillar-on-surface as its band-gap attenuation is about one order of magnitude larger [92]. The coupling of photonics and phononics has added yet another thrust of applications. For example, a periodic array of pillars deposited on a thin plate may be designed to exhibit dual phononic and photonic band gaps, holding promise for the simultaneous confinement and tailoring of sound and light waves [54, 93, 94]. The reader is referred to [95] for a discussion on ‘phononic plate waves’ including waves in pillared plates.

In the characterization of acoustic/elastic metamaterials, generally a monopole resonance relates to negative effective compressibility and a dipole resonance relates to negative effective mass density when evaluated within the range of a hybridization band gap. However, a pillared metamaterial element tends to bring more difficulties in analyzing negative effective compressibility or mass density than conventional 1D, 2D, or 3D metamaterial elements. This is due to the lack of a precise effective medium theory describing the complex pillar’s vibrations in free space associated with its base. Nevertheless, a pillared metamaterial may be considered as a homogeneous plate with anisotropy in the effective mass density matrix [96] or effective wavenumber [97], exhibiting negativity in the effective density [96–98], effective Young’s modulus [97], or effective stiffness [99]. Indeed, the monopolar or dipolar resonant frequencies of a pillar may be easily tuned by a proper choice of height and/or diameter [100], resulting in easily being able to probe the conditions for either the effective mass density negativity or the effective modulus negativity. The effect of pillar resonances in the context of scattering and transmission of a single or a line of resonant pillars subject to an incident surface wave is also a problem of interest. In such a configuration, the pillars emit waves that can interact with an incident wave, allowing for a phase/amplitude shift in the transmission. Fano resonance can be induced by introducing two dissimilar pillars in one unit cell along one row of pillars [101]; see reference [102] for evidence of Fano resonance-like attenuation profiles in a nonpillared locally resonant elastic metamaterial. A new geometry proposed recently consists of replacing a homogeneous pillar with a multilayer material, a kind of 1D phononic crystal [103], allowing confinement of modes inside a cavity or at the interface between the pillar and the substrate. In such a geometry, these highly confined modes of pillars result in very sharp Fano resonances—or the acoustic analog of electromagnetically induced transparency (EIT)—when they interact with an incident surface Rayleigh [104, 105] or Love [106, 107] mode. More generally, owing to the recent growing interest in the topic of metasurfaces, where a very thin (subwavelength) structure containing phase-array elements can manipulate the propagation of sound (or light) and give rise to various new effects such as anomalous refraction and reflection and focusing or imaging phenomena, a line of resonant pillars on a plate or a substrate provides a new tool

for exhibiting similar features by manipulating the propagation of plate and surface waves.

As mentioned earlier, the pillared medium architecture may also be realized for a 1D system, e.g. consisting of a slender tube or beam with stubs (another term often used to describe pillars) grafted on a single side or both sides—in this case, the Brillouin zone stretches along only one dimension. The first study on acoustic band gaps with such structures was published by Kushwaha *et al* [108] in 1998. They found that a periodic pattern of large stop bands is obtained with the lowest gap extending possibly down to zero frequency. Large magnonic [109] and photonic [110] band gaps were subsequently found with the same structure. The grafted stubs can behave as resonators to induce Fano resonances when the resonance is situated between two zeros of transmission [111], and can even exhibit the acoustic analog of EIT [101, 112] and trapped mode phenomena [113]. If the stubstructures are placed between two slender tubes, selected transfer of a single propagating state from one tube to the other is possible, with all other neighboring states remaining unaffected. This result has been applied to filtering or multiplexing [114]. The characteristics of the band structure and wave transmission when the stubs are grafted to the tube in a single side [115–117], double symmetric sides [118–121], and asymmetric sides [122] were theoretically and experimentally investigated. Theoretical investigations on the connection between the transmission properties of continuous stubbed models and macroscale thermal transport have been proposed [123, 124].

In the realm of applications, pillared phononic crystals, metamaterials, and metasurfaces make it possible to control and manipulate acoustic and/or elastic waves with many potential benefits in modern information processing and communication, among other avenues. To follow is a synopsis of six possibilities: (I) *negative refraction and superlenses*. With a proper choice of pillar geometry in pillared periodic media, a negative refractive effect can be achieved (i) when a dispersion branch reveals opposite signs between the group velocity and the phase velocity, yielding a negative effective refractive index [125–127], and (ii) when the group velocity is never in the opposite direction to the phase velocity but the convexity of the isofrequency contours of a branch leads to negative refraction with a positive effective index [128]. This latter scenario demonstrates subwavelength high resolution in superlensing applications. A far-field super-resolution experiment has been demonstrated for a metamaterial made out of long pillars attached to a plate with the one-channel inverse filter [129]. (II) *Waveguides, defect states, and filtering applications*. If the traveling frequencies are located within a Bragg or hybridization band gap of the background pillared structures, waveguides may be constructed consisting of different sizes of pillars or line- or curved-shape defects [68, 87, 90, 130–141]. Such design interventions can produce localized modes inside the Bragg or hybridization band gaps of the phononic crystal, hence allowing the propagation of confined modes in the waveguide. (III) *Vibration attenuation*. The existence of Bragg and local resonant band gaps in pillared phononic crystals and metamaterials plays an important role in the design of sound [98, 143] and elastic [27–32, 37, 142,

144] wave insulators. As mentioned earlier, an extra-wide band gap combining both Bragg and local resonant band gaps was proposed by tailoring the plate connection between neighboring pillars [59, 70, 75–79]; these systems serve as excellent candidates for vibration attenuation in solids, in passive form and even with tunable properties [145]. If the pillar resonators are on the meter scale, a pillared metamaterial may in principle prevent Rayleigh modes in seismic wave propagation [146, 147] or even shape seismic wave flow [148]. Guided or localized modes enhanced by band gaps can also be used for energy harvesting [149–151]. (IV) *Graded resonant devices*. Combining a resonant pillar with a gradient-index (GRIN) lens [152–157], a focusing point can be achieved beyond the diffraction limit [158]. By gradually varying the height of the pillars, resonant GRIN metalenses for flexural waves [159] and metasurfaces for converting surface Rayleigh waves to bulk shear waves [160] have been proposed. The guiding of elastic waves with a graded radius of pillars in a phononic crystal plate has also been investigated [161]. (V) *Phononic graphene*. Pillars placed in a hexagonal lattice on a plate can be regarded as spring-loaded resonators, providing a promising platform for investigation of the elastic analog of graphene [162], as well as the quantum valley Hall effect [163] and the quantum spin Hall effect [164] (in analogy to corresponding systems in quantum mechanics and condensed matter physics) with novel phonon transport behavior such as pseudo diffusion [165], the Zitterbewegung effect [165], the zigzag edge state [162], and topologically protected edge [166–169] and corner [170, 171] modes. (VI) *Pillared metasurfaces*. One view of a metasurface is that it can be considered as a slice of a bulk metamaterial with a subwavelength thickness; such a surface is able to steer wavefronts at will by designing an abrupt phase profile on the surface [172–178]. A growing interest is devoted to these metasurfaces due to their broad functionalities such as anomalous reflection and refraction, or focusing and imaging phenomena. Following the generalized Snell's law [179], a line of pillars can be designed to manipulate various wavefront functionalities from the discrete phase response of an array of resonant pillars [100]. This is quite attractive in view of the potential practical applications of controlling the propagation of Lamb waves on a plate or surface acoustic waves (SAWs) on a substrate. Such pillared metasurfaces also demonstrate diverse resonant phenomena [101, 112]; for example, the acoustic analog of a bound state in a continuum, EIT, Autler–Townes splitting (ATS), and others [180].

Finally, the pillared plate configuration has also found application on smaller scales. In the gigahertz regime, pillared configurations have been investigated giving rise to ‘hypersonic phononic crystal and metamaterials’ [181–185] where band gaps have been observed by Brillouin light scattering spectroscopy. At the far extreme of scales, reaching down to a few nanometers, the concept of a *nanophononic metamaterial* (NPM) was proposed by Hussein *et al* for the reduction of the lattice thermal conductivity [186–191]. An NPM in the form of a suspended silicon membrane with a periodic

array of nanopillars was proposed as a particularly advantageous configuration for not only thermal conductivity reduction but also thermoelectric energy conversion. In this configuration, the nanopillars generate local resonances that, similar to macroscopic systems, couple and hybridize with the underlying dispersion curves. However, here the interest is in creating a very large number of local resonances (possibly of the order of millions or more) spanning the entire spectrum of thermal transport—which may reach up to tens of terahertz. A recent theoretical study using lattice dynamics (LD) calculations and molecular dynamics (MD) simulations predicted two orders of magnitude of reduction in the in-plane thermal conductivity of a silicon membrane stemming from the introduction of nanopillars with a shape, size, and spacing carefully selected with respect to the base membrane thickness [190, 191]. In particular, it was shown that increasing the height and width of the nanopillars (up to a limit dictated by the phonon mean free path (MFP) distribution) increases the level of thermal conductivity reduction [190, 191]. Other research examined diffuse phonon scattering at the interface between pillars and a substrate [192].

In this article, we provide a review of the authors' original contributions to the study and development of pillared materials—for both macroscale elastic waves and nanoscale thermal transport—as well as the progress that emerged afterward by the phononics community at large. The paper is organized into seven sections. The current section has provided a background and an overview of the state of the art in pillared materials and structures. In the second section, we review the vibrational properties of pillared phononic crystal plates for wave transport and multiphysical interaction. In the third section, we cover pillared metamaterial plates with enhanced low-frequency band gaps and super-resolution focusing. In the fourth section, we review pillared acoustic metasurfaces with anomalous resonant and transmitted properties. The fifth section focuses on topological pillared phononic plates that exhibit topologically protected edge states with immunity to local perturbations. In the sixth section, we review the concept of a NPM, which, as an example, is based on a silicon thin film or membrane with a periodic array of nanopillars erected on one or two of the free surfaces. Finally, we conclude with a summary and an outlook on the future promise of continued research on pillared systems at various length scales and for a variety of applications.

## 2. Wave propagation properties of pillared plates

### 2.1. Basic model

Some of the concepts related to phononic crystals, and in particular pillared structures, can easily be understood in the frame of very simple and academic models in one dimension. For instance, assume a linear monoatomic chain of period  $a$ , composed of atoms of mass  $m$  connected to each other by a force constant  $\beta$  (figure 1(a)). By writing the equation of motion for atom  $n$ ,  $m\partial^2 u_n / \partial t^2 = \beta(u_{n+1} + u_{n-1} - 2u_n)$  where  $u_n(t)$  is the displacement of atom  $n$  at time  $t$ , and inserting a propagating wave solution for the displacement,  $u_n(t) = A e^{i(kna - \omega t)}$ , the phonon dispersion curve is straightforwardly

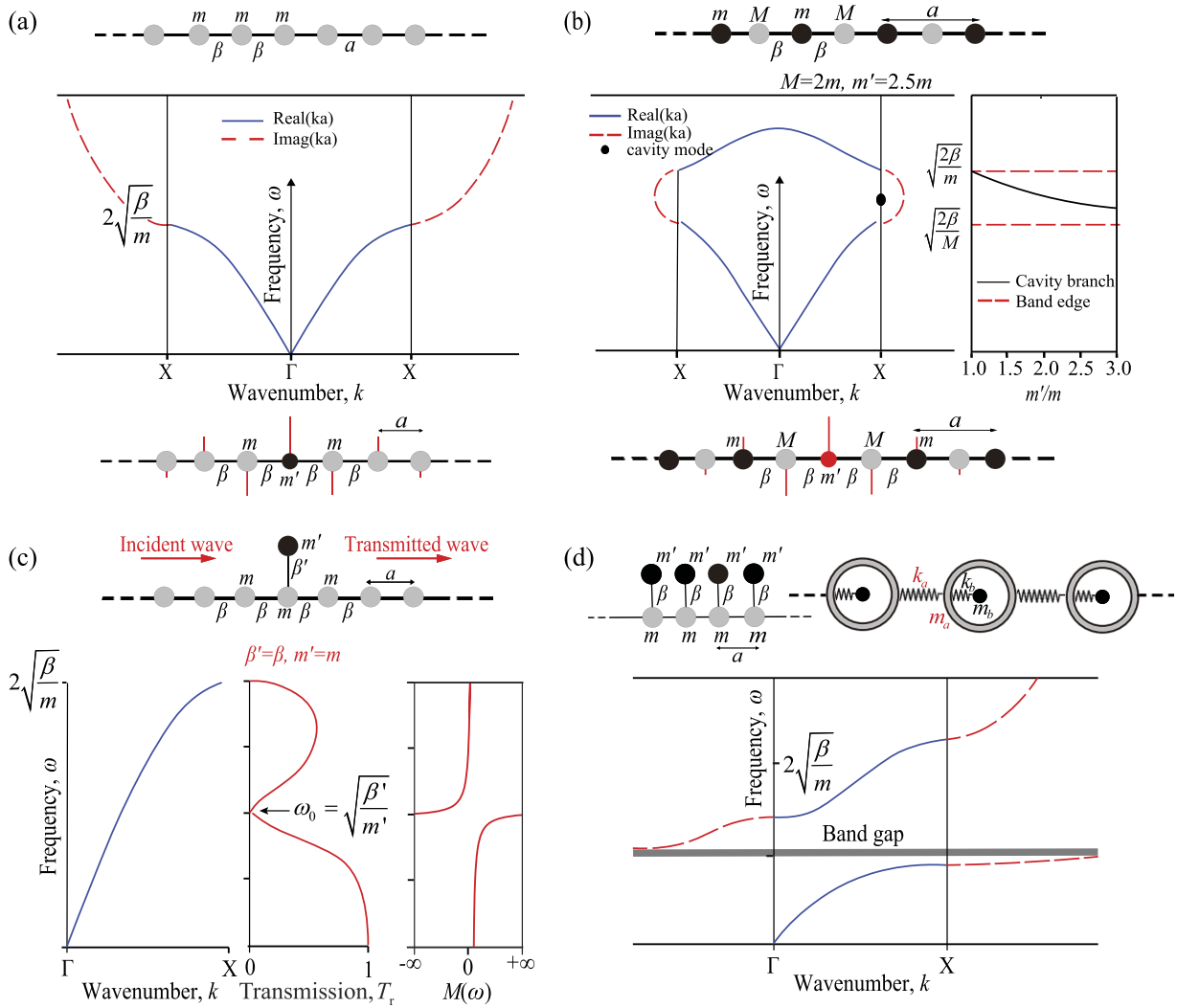


**Figure 1.** Mass–spring models and corresponding dispersion curves. (a) (Top) A linear monoatomic chain composed of identical atoms. (Middle) Dispersion curves inside the first Brillouin zone; the blue and red curves respectively correspond to the real and imaginary parts of the wave vector. (Bottom) Eigenfunction of a localized mode associated with a light defect atom ( $m' = m/2$ ) at site  $n = 0$ . For the sake of clarity, the displacement amplitude of each atom is represented by a vertical bar. (b) (Top) A biatomic linear chain comprising two different atom types with  $m < M$ . (Middle) Dispersion curves of the perfect crystal as well as the frequency of a localized mode in the band gap when the central atom of mass  $m$  is replaced by a defect atom of mass  $m'$ . The latter should be heavier than  $m$ . (Bottom) Eigenfunction of a localized mode associated with a defect of mass  $m' = 2.5m$  the frequency of which is shown by a dot in the band gap of the dispersion curves. (c) (Top) A side atom is attached to the monoatomic linear chain. (Middle) In front of the dispersion curves of the monoatomic linear chain shown on the left, we present the transmission coefficient (middle) displaying a zero at the resonance frequency and the behavior of the dynamical effective mass  $M(\omega)$  (right). (d) (Top) A periodic array of side atoms is attached to the linear chain to form a locally resonant periodic chain. An equivalent model where each atom has a resonating internal degree of freedom is also displayed on the right. (Bottom) Dispersion curves of the infinite periodic structure with side atoms showing the opening of a hybridization band gap around the resonance frequency represented by the gray horizontal bar. The blue and red curves correspond to the real and imaginary parts of the wave vector, respectively. The imaginary parts are presented in continuation of the real parts.

derived as  $m\omega^2 = 2\beta[(1 - \cos(ka))]$ , where  $k$  and  $\omega$  are respectively the phonon wavenumber and frequency (figure 1(a)). The wavenumber takes a real value as long as the frequency does not exceed  $\omega_{\max} = \sqrt{4\beta/m}$ . Above this frequency, it becomes complex ( $k = k' + ik'' = \pi/a + ik''$ ), which means that the vibration will be attenuated and is not permitted to propagate along the chain. Now, if a defect in the form of a light mass  $m' < m$  is inserted at the site  $n = 0$  of the chain, the equations of motion will admit a solution associated with a localized mode at a frequency above  $\omega_{\max}$ , with an eigenfunction that decays exponentially on both sides far from the

defect. An example corresponding to  $m' = m/2$  is shown in the lower panel of figure 1(a). This is a simple analog of a cavity mode inside a phononic crystal. It should be noted that if  $m' > m$ , the defect cannot produce a localized mode but will disturb the local density of states (DOS) in the frequency range of the pass band. This approach can be extended to the case of a biatomic linear chain consisting of two different alternate masses  $m$  and  $M$  (with  $m < M$ ) connected by the same spring of force constant  $\beta$ . The acoustic and optical phonon branches are now separated by a gap at the edge of the Brillouin zone (figure 1(b)). Again, by inserting a defect of mass  $m'$  at site

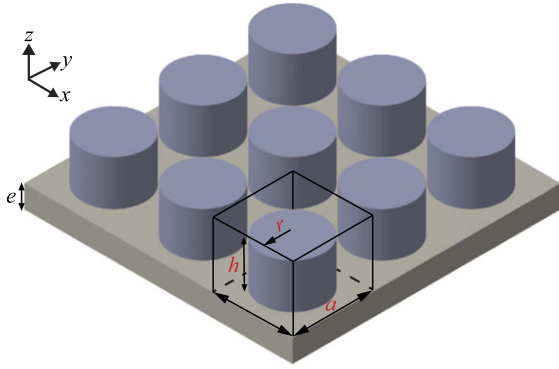


**Figure 2.** Geometry of a phononic crystal plate consisting of periodic pillars deposited on a thin plate. The plate thickness is denoted by  $e$ , the radius of the pillars by  $r$ , and the height of the pillars by  $h$ .

0 occupied by an atom of mass  $m$ , the crystal can exhibit a localized mode associated with the defect inside the band gap and the variation of the corresponding frequency is presented in the figure as a function of the ratio  $m'/m$ . An example of the eigenfunction decay on both sides of the defect is shown in the lower panel of figure 1(b) for  $m' = 2.5m$ .

A new situation is encountered when a side atom of mass  $m'$  is attached to the monoatomic linear chain at site  $n = 0$ , with a force constant  $\beta'$  (figure 1(c)). This is the simplest analog of a pillar attached to a plate and provides a simple model for the introduction of the concept of a local resonance band gap. Let us call  $v$  the displacement of the side atom. Then, the equations of motion of this atom and the atom at site '0' are respectively  $-m'\omega^2 v = \beta'(u_0 - v)$  and  $-m\omega^2 u_0 = \beta(u_1 + u_{-1} - 2u_0) + \beta'(v - u_0)$ . By eliminating the degree of freedom  $v$  associated with this additional mass, the equation of motion for atom '0' becomes  $-M(\omega)\omega^2 u_0 = \beta(u_1 + u_{-1} - 2u_0)$  with  $M(\omega) = m + \frac{\beta'm'}{\beta - m'\omega^2}$ .

This exactly describes the situation of an atomic linear chain containing a mass defect  $M(\omega)$  at site  $n = 0$ , but now the latter mass becomes a dynamical mass depending on the frequency. At very low frequency, this mass starts at  $m + m'$ , then increases until it diverges to  $+\infty$  at a 'resonance' frequency  $\omega_0 = \sqrt{\beta'/m'}$ , then jumps to  $-\infty$  and remains negative until a frequency of  $\omega'_0 = \sqrt{\beta'(m + m')/mm'}$  where it vanishes before becoming again positive and going to  $m$  at very high frequencies (figure 1(c)). The most interesting observation is that at the local resonance frequency  $\omega_0 = \sqrt{\beta'/m'}$ , the dynamical mass behaves like a very heavy mass which will prevent any transmission (assuming that the parameters are chosen in a such a way that  $\omega_0$  falls in the range of the propagating waves in the linear chain) and produces a zero in the transmission coefficient (figure 1(c) corresponding to  $m = m'$  and  $\beta = \beta'$ ). Moreover, the additional mass and the atom at site 0 vibrate in phase just below  $\omega_0$  and out of phase just above this frequency. Finally, if a periodical array of side atoms is attached to the linear chain (figure 1(d)), the zero of transmission widens into a local resonance hybridization band gap, as sketched in figure 1(d). Of profound importance is the notion that the resonance frequency may be chosen to be very

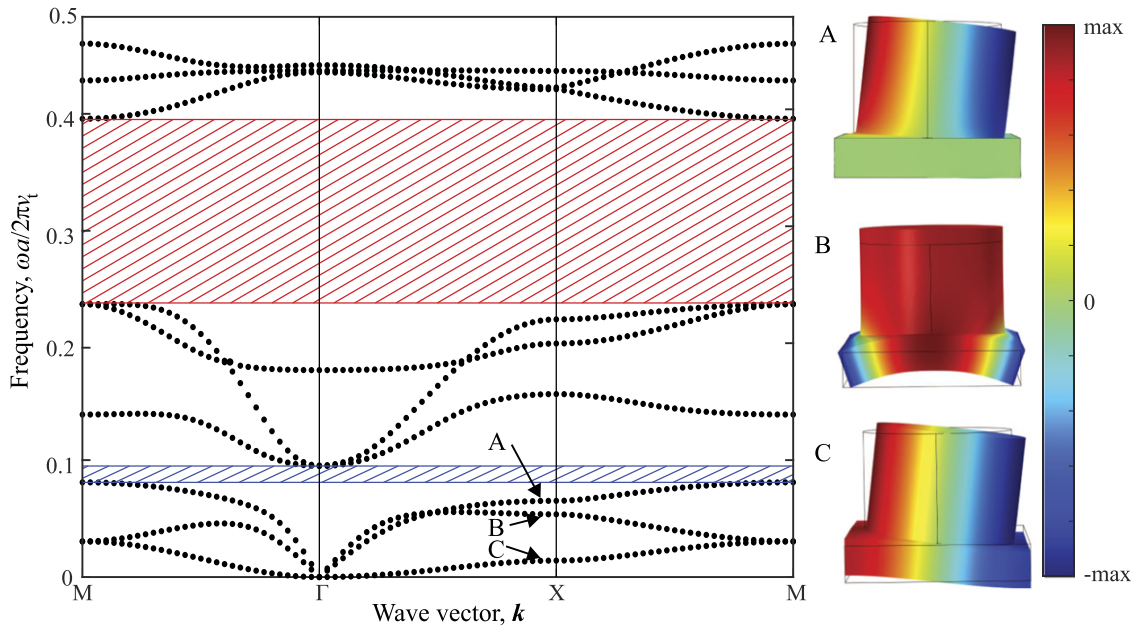
low, which opens up the field of effective medium theory for metamaterials as will be discussed in depth later. An equivalent model to the one discussed above is also presented in figure 1(d) where each atom of the lattice has a resonating internal degree of freedom. The reader is referred to references [193, 194] for analytical derivations of band-gap properties, such as bounds on bandwidth and attenuation strength, in strings or beams with attached mass resonators, and to reference [195] for a characterization of the transition between a Bragg band gap and a subwavelength local resonance band gap for a beam with attached resonators.

## 2.2. Dual aspects of phononic crystals and metamaterials

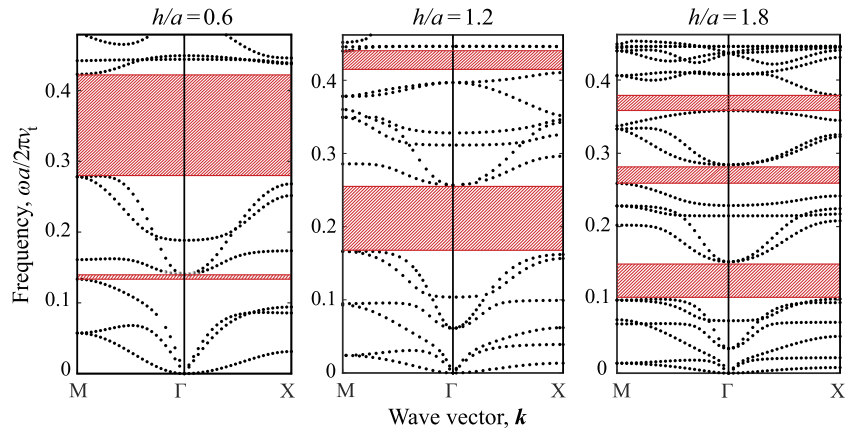
Many efforts have been devoted to the study of absolute band gaps in phononic crystals, particularly for applications such as confinement, waveguiding, and filtering. In this subsection, we review the basic band structure properties of phononic crystal plates, which comprise a periodic arrangement of pillars placed on top of a thin homogeneous plate as displayed in figure 2, forming a square array. Bragg and hybridization band gaps can be simultaneously observed in such phononic plates and as such they may be dually classified as phononic crystals and acoustic metamaterials. The illustrations are given for pillars made of steel on a silicon plate. The elastic constants and mass densities of these materials are found in reference [26]. Dispersion curves are calculated by the finite-element method along the 2D irreducible Brillouin zone and presented in the form of reduced frequency  $\Omega = \omega a/(2\pi v_t)$ , where  $v_t$  is the transverse bulk velocity of silicon.

The dispersion curves in figure 3 are calculated for the parameters: pillar radius  $r/a = 0.42$ , pillar height  $h/a = 0.6$ , and plate thickness  $e/a = 0.1$ . At low frequencies, the three lowest bands appear at the  $\Gamma$  point (the center of the Brillouin zone)—these are the antisymmetric ( $A_0$ ), shear-horizontal ( $SH_0$ ), and symmetric ( $S_0$ ) Lamb modes. As the frequency increases, the three branches bend in such a way as to give rise to the opening of a narrow hybridization band gap (shaded in blue). At this frequency, the wavelengths of the  $S_0$  and  $A_0$  Lamb modes are about 15 and 2 times the lattice constant  $a$ , respectively. In fact, the bending mode of the pillars generates a negative effective in-plane mass density within one frequency range, and the compressional mode of the pillars provides a negative effective out-of-plane mass density within another frequency range where, within the overlapped frequency range, the total effective mass densities are negative, resulting in the opening of the low-frequency hybridization band gap [196]. The simultaneous bending of the acoustic branches and the existence of this band gap are intimately related to the choice of geometrical parameters, as will be discussed below. Besides, with a choice of parameters within the common range for actual materials and devices, one can also observe the existence of a broad Bragg band gap; see the region shaded in red in figure 3.

To provide a deeper insight into the origin of the modes leading to the opening of the hybridization gap, we have calculated the spatial distribution of the eigenmodes at the high-symmetry point X of the Brillouin zone and plotted them in



**Figure 3.** Dispersion curves for the following pillared plate: steel pillar radius  $r/a = 0.42$ , pillar height  $h/a = 0.6$ , and silicon plate thickness  $e/a = 0.1$ . The red and blue dashed zones indicate Bragg and local resonance hybridization band gaps, respectively. Eigenmodes (real part of the out-of-plane displacement  $u_z$ ) corresponding to the three points A, B and C at X are displayed on the right. The blue and red colors stand for  $-\max$  and  $\max$  values, respectively. Reprinted figure with permission from [26], Copyright (2008) by the American Physical Society.



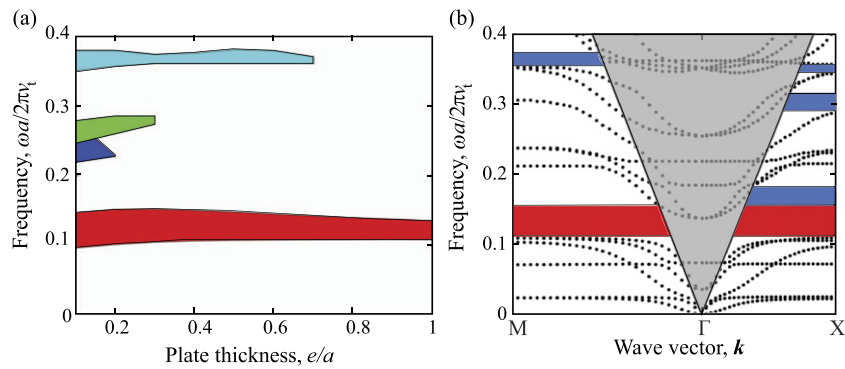
**Figure 4.** Evolution of the band structure for different values of the height of the pillar: (left)  $h/a = 0.6$ , (middle)  $h/a = 1.2$  and (right)  $h/a = 1.8$ . The other geometrical parameters are  $e/a = 0.2$  and  $r/a = 0.42$ . Reprinted figure with permission from [26], Copyright (2008) by the American Physical Society.

figure 3. The modes A and C are clearly associated with a bending of the pillar together with, respectively, a weak and a strong bending of the plate. The vibration of mode B corresponds to a compressional mode, in the  $z$  direction, correlated with a strong vertical displacement of the plate. More specifically, the motions of branches A and B are strongly correlated with the opening of the absolute low-frequency hybridization band gap.

In figure 4, we have fixed the values of the radius of the pillar  $r/a = 0.42$  and the thickness of the plate  $e/a = 0.2$  while changing the height of the pillar as  $h/a = 0.6, 1.2,$  and  $1.8$ . For  $h/a = 0.6$ , we note the existence of the low-frequency hybridization and the high-frequency Bragg band gaps discussed previously. The lowest one closes for  $h/a = 1.2$  and

the central frequency of the higher one decreases, but appears to change its type. This is observed in the middle panel of figure 4, which also shows that the band structure there exhibits a new band gap, occurring at the reduced frequency 0.42. When increasing  $h/a$  to 1.8, the central frequencies of the first two band gaps move downward together with the dispersion curves, whereas a new additional absolute band gap appears again at higher frequencies. It is interesting to remark that, for some of these band gaps, their opening results from the crossing of the normal acoustic branches with almost flat bands, which is the key mechanism that characterizes locally resonant materials.

We have also studied the evolution of the band gaps with the thickness of the plate  $e$ , keeping constant  $h/a = 1.8$  mm and



**Figure 5.** (a) Evolution of the absolute band gaps in the right panel of figure 4 as a function of the thickness of the plate, keeping constant the other geometrical parameters ( $h/a = 1.8$  and  $r/a = 0.42$ ). (b) Representation of the dispersion curves for a thick plate ( $e/a = 1$ ). The triangular gray area corresponds to the sound cone of the silicon plate. The blue (red) area shows the existence of a partial (absolute) band gap for SAWs. Reprinted figure with permission from [26], Copyright (2008) by the American Physical Society.

$r/a = 0.42$  (right panel of figure 4). This is useful for demonstrating the evolution of the branches when transitioning from a thin plate to a thick plate mimicking a substrate. When increasing  $e/a$  from 0.1 to 1.0 (figure 5(a)), we observe a slow variation of the central frequency of the gaps. In addition, most of the gaps close at  $e/a = 0.7$ , because many dispersion branches move upwards, except for the hybridization one at low frequency, which appears more robust and closes for  $e/a > 1$ . In parallel, when increasing the thickness of the plate from  $0.3a$  to  $a$  and higher, the Lamb waves gradually tend to become confined at the two opposite surfaces of the thick plate, rendering them as SAWs or Rayleigh waves on each of the two sides. In the illustration of the dispersion curves, the separation between SAW and bulk waves can be achieved by drawing a sound line that corresponds to the lower phase velocity in the bulk substrate, silicon in our example. Figure 5(b) represents the dispersion curves obtained for a thickness  $e/a = 1$  in which the sound cone of silicon is represented by the gray shaded area. This means that the modes below the sound cone can only propagate at the surface. In contrast, inside the cone, the modes can be radiative and coupled to the bulk silicon modes. From this analysis, we extend the notion of band gaps to SAWs by highlighting among the corresponding branches the frequency areas that are free of modes. Indeed, in figure 5(b), the blue shaded areas correspond to partial band gaps in one direction  $\Gamma X$  or  $\Gamma M$  of the Brillouin zone while the red area corresponds to an absolute band gap for SAWs.

Finally, we have also investigated the robustness and persistence of the low-frequency hybridization band gap upon different combinations of materials constituting the pillars and the plate among a set of five materials displaying very different acoustic properties: tungsten, steel, silicon, aluminum, and epoxy. In the left panel of figure 6, we show the limits of the low-frequency gap by changing the material of the plate when the pillars are made of steel. Similarly, the right panel of figure 6 displays the gap limits for various materials in the pillars for a plate made of silicon. One can notice the persistence of the hybridization band gap even if the constituting materials are identical. This supports the understanding that the origin of the gap is related to the geometrical rather than the constituent material parameters of the extended structure.

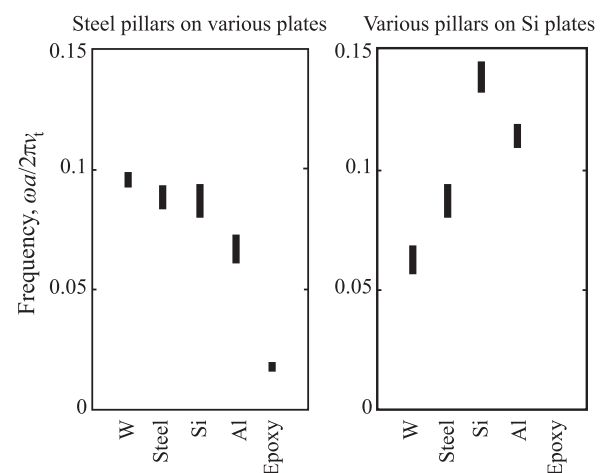


**Figure 6.** Evolution of the lowest-frequency band gap limits for different combinations of constituting materials. (Left) Steel pillars on a plate of different materials. (Right) Various pillars on a silicon plate. The length of each vertical mark represents the width of the band gap for each case. The geometrical parameters are  $e/a = 0.1$ ,  $h/a = 0.6$ , and  $r/a = 0.42$ . For an epoxy pillar on a silicon plate, the lowest-frequency band gap disappears. Reprinted figure with permission from [26], Copyright (2008) by the American Physical Society.

On the other hand, the central frequency of the gap is very dependent upon the choice of the materials and happens at lower frequencies when we combine a high-density material, steel, in the cylinders with a low-density material, epoxy, in the plate. It is noteworthy that with this choice one can obtain a gap in the audible frequency range, around 2 kHz, for a period of  $a = 20$  mm and the other parameters being scaled accordingly. Such solid systems could be used practically as a vibrationless environment for high-precision mechanical systems.

### 2.3. Phononic transmission and waveguiding

From the calculation of both transmission coefficients and dispersion relations of pillared phononic crystal plates, we illustrate here the phenomenon of wave guiding when removing one row of pillars in a perfect crystal. The flexibility of

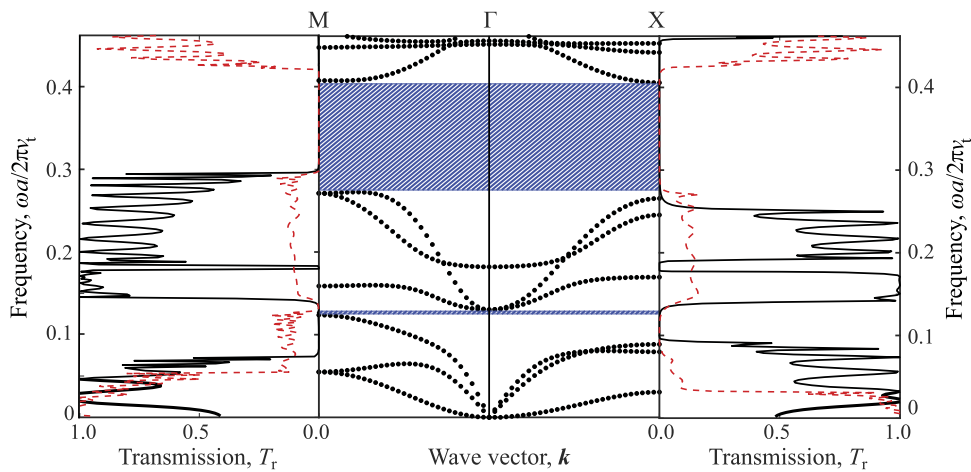


**Figure 7.** (Left and right) Transmission calculation (black solid line for  $S_0$  Lamb wave excitation and red dashed line for  $A_0$  Lamb wave excitation) through a phononic crystal plate consisting of a square lattice of steel pillars deposited on a silicon plate. The geometrical parameters are  $h/a = 0.6$ ,  $r/a = 0.42$  and  $e/a = 0.2$ . (Middle) Dispersion curves calculated along the high-symmetry axes  $\Gamma X$  and  $\Gamma M$  of the Brillouin zone. The blue areas correspond to the position of the low- and high-frequency absolute band gaps. Reprinted figure with permission from [130], Copyright (2009) by the American Physical Society.

tuning the acoustic/elastic properties, especially for waveguides, makes it particularly suitable for diverse applications from transducer technology to filtering and guiding of acoustic/elastic waves.

Figure 7 shows the transmission coefficient for a pillared phononic crystal plate made of a square array of steel pillars deposited on a thin silicon plate. The band structure is reported in the middle panel in the reduced frequency range (0, 0.45) along the high-symmetry axes  $\Gamma X$  and  $\Gamma M$  of the first Brillouin zone. The choice of the geometrical parameters ensures the existence of two absolute band gaps, respectively at low and high frequencies (relative to the frequency range displayed). We also show the computed transmission spectra in the directions  $\Gamma X$  and  $\Gamma M$  of the Brillouin zone, displayed on each side of the central band diagram. The transmission spectra are given both for an  $S_0$  and an  $A_0$  incident Lamb wave.

We now investigate the possibility of guiding wave modes in both the low- and high-frequency gaps inside an extended linear defect designed by removing one line of pillars as seen in figure 8(a). The length of the waveguide is assumed to be seven periods of the unit cell. In the super-cell calculations, the neighboring waveguides are separated from each other by four lines of full pillars in order to minimize their coupling and hence the leakage effect. Figure 8(b) presents the transmission spectra where the incident wave is an  $S_0$  (upper) or an  $A_0$  Lamb wave (lower). For comparison, we also provide the transmission through the perfect (red dashed lines) phononic crystal. The shaded blue areas represent the positions of the two band gaps from the corresponding dispersion curves. One can see the occurrence of a transmitted signal in the higher band gap for both the  $S_0$  and  $A_0$  Lamb wave excitations. In contrast, the transmission in the low-frequency gap essentially occurs for  $S_0$  Lamb wave excitation while it remains very low for  $A_0$ . To highlight the wave guiding properties through the gaps, we show in figure 8(c) the propagation of two monochromatic waves,

corresponding respectively to an  $S_0$  Lamb mode at the reduced frequency of 0.393 and to an  $A_0$  mode at frequency 0.108.

#### 2.4. Example configuration: hollow pillars and whispering-gallery modes

**2.4.1. Whispering-gallery modes of hollow pillars.** The study of whispering-gallery modes (WGMs) dates back to the work of Rayleigh in 1910 on the propagation of sound around a gallery in St Paul's Cathedral, London [197]. High-quality-factor WGM resonators may be applied to sensing [198], filters [199], and modulators [200], among other applications in optics and photonics, areas that have been receiving increasing attention in recent years. In this subsection, hollow pillars are employed instead of full-solid pillars in phononic crystal plates. Indeed, the hollow structure can introduce WGMs with a high quality factor owing to their confinement and this parameter can even be significantly enhanced by insertion of an additional full pillar at the bottom of the hollow pillar to isolate the WGM from the plate. We consider a hollow pillared phononic crystal plate with a square lattice array and the entire structure made of silicon. An example of a hollow pillar unit cell is displayed in figure 9(d).

We first present the band structure of a full pillared phononic crystal plate along the direction  $\Gamma X$  of the reduced Brillouin zone as shown in figure 9(a). The geometrical parameters are: height of pillar  $h/a = 0.45$ , radius of pillar  $r/a = 0.4$ , and plate thickness  $e/a = 0.1$ , where  $a$  is the lattice constant. Similar to earlier figures, the dispersion curves are plotted in the form of the reduced frequency  $\Omega = \omega a / (2\pi v_t)$ . As explained in the previous subsections, this pillar structure exhibits both a Bragg band gap and a low-frequency hybridization band gap simultaneously and therefore behaves as a phononic crystal or as an elastic metamaterial depending on the context. Then, the full pillar is replaced by a hollow pillar, the geometric parameters of which are the same except for the inner radius, which is chosen as  $r_i/a = 0.145$ .

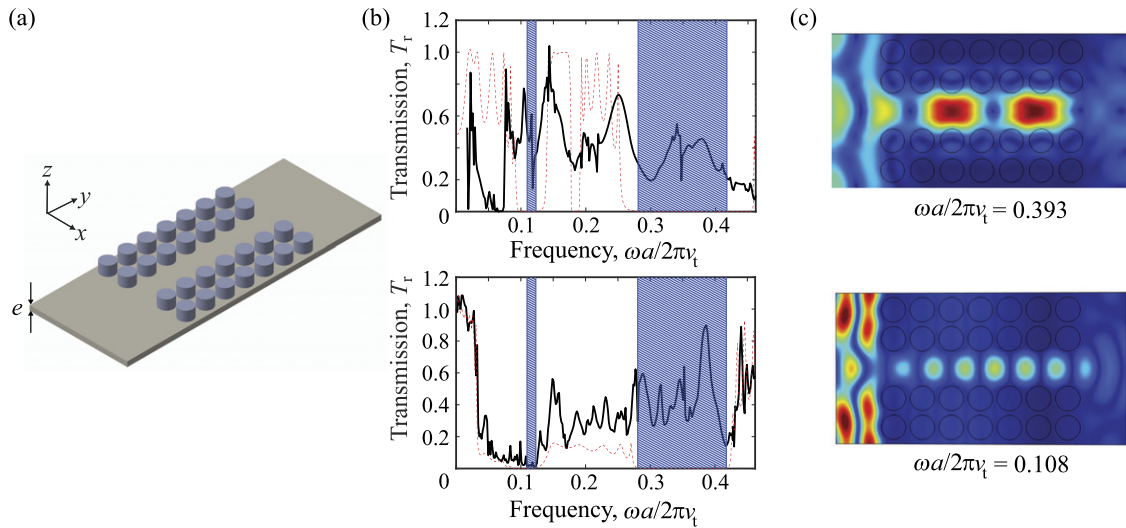


**Figure 8.** (a) Schematic view of a line-defect waveguide; (b)  $S_0$  Lamb wave excitation (upper) and  $A_0$  Lamb wave excitation (lower) transmission through the waveguide (black solid lines) and through the perfect (red dashed lines) phononic crystal. (c) Example of guided mode for an  $S_0$  Lamb wave (top right) and an  $A_0$  Lamb wave (bottom right) at the reduced frequencies of 0.393 and 0.108, respectively. The blue and red colors stand for 0 and max values, respectively. Reprinted figure with permission from [130], Copyright (2009) by the American Physical Society.

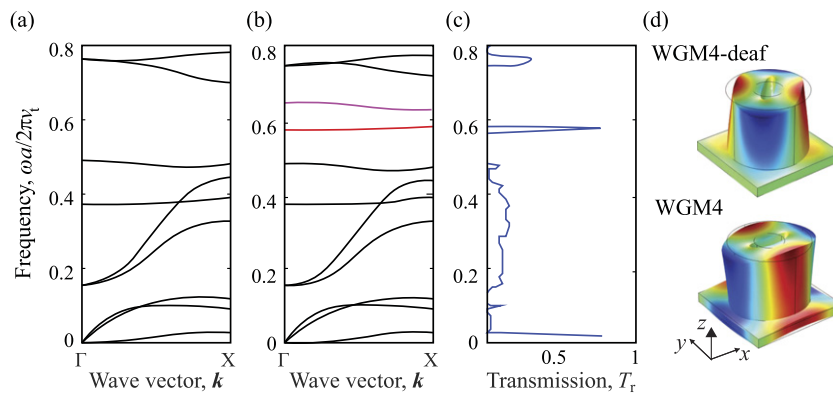


**Figure 9.** (a) Dispersion curves along the  $\Gamma X$  direction for a full pillar unit cell in a square lattice; (b) same as in (a) but for a hollow pillar case; (c) the corresponding transmission curve with respect to (b); (d) real part of the  $z$ -displacement component of the eigenmode of the red and pink bands at the  $\Gamma$  point. The geometric parameters are: height of pillar  $h/a = 0.45$ , radius of pillar  $r/a = 0.4$ , inner radius of hollow pillar  $r_i/a = 0.145$ , and plate thickness  $e/a = 0.1$ , where  $a$  is the lattice constant. The blue and red colors stand for  $-max$  and  $max$  values, respectively. Reprinted figure with permission from [68], Copyright (2016) by the American Physical Society.

The dispersion curves of the hollow pillar unit cell are presented in figure 9(b), where two new bands in red and pink appear in the Bragg band gap; meanwhile, all the black bands remain almost unchanged. In figure 9(c), the corresponding transmission curve is calculated with the fundamental antisymmetric ( $A_0$ ) Lamb mode excitation and the propagation direction along the  $x$ -coordinate. One observes that only the red band can generate a transmission peak  $p$ , while the pink band behaves as a *deaf mode*. This is attributed to the symmetry of the eigenmodes of the two bands, as illustrated by the real part of the  $z$ -displacement component of the two bands at the  $\Gamma$  point in figure 9(d). Both the red and pink bands are characterized by the quadrupolar WGM (WGM4). The displacement field of WGM4 (red band) is symmetric with respect to the  $x$ - $z$  plane and is therefore compatible with the symmetry of the incident  $A_0$  Lamb wave, so

that WGM4 can be excited. However, it is antisymmetric for WGM4-deaf (pink band), resulting in a mode that cannot be observed in transmission. It should be mentioned that the quality factor of WGM4 can be significantly enhanced by inserting an additional full pillar part between the hollow pillar and the plate.

The acoustic path of WGM around the hollow pillar of WGM is a multiple integer of the wavelength, equal to 2 for the presented WGM4. Therefore, the wavelength qualitatively behaves in the form of  $\lambda = \pi(r + r_i)/2$ . By increasing the inner radius, the frequency of WGM4 will redshift even to a low-frequency band gap. It has been shown [68] that the WGMs can be efficiently tuned to cross a wide frequency band by varying the inner radius of the hollow pillars.

As the WGMs can be designed to cover the full Bragg band gap by varying the inner radii of the hollow pillars, several

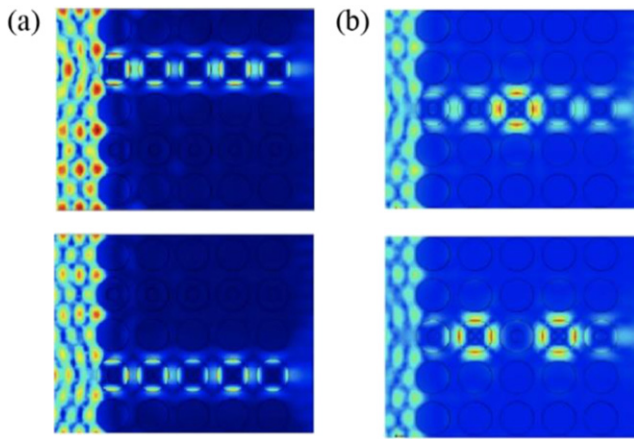


**Figure 10.** Application of WGM4 in a multichannel wavelength multiplexer (a) and a monochannel wavelength multiplexer (b). The upper and lower panels correspond to two different narrow pass bands for each column. The blue and red colors stand for 0 and max values, respectively. Reprinted figure with permission from [68], Copyright (2016) by the American Physical Society.

narrow pass bands can be expected for a mixed system composed of different inner radii. Here, we demonstrate the design of mono- and multichannel wavelength division multiplexers by inserting appropriate waveguides in a  $(5 \times 5)$  supercell phononic crystal plate.

For the multichannel wavelength multiplexer, the phononic crystal plate contains two linear hollow pillar waveguides separated from each other by a line of full pillars, which prevents leakage between the two waveguides as shown in figure 10(a). We present the displacement fields of the transmitted wave through the two waveguides corresponding to two narrow pass bands in the Bragg band gap. Actually, the transmission of two narrow pass bands does not need two separate waveguides. In figure 10(b), a monochannel wavelength multiplexer is considered, where the waveguide is constituted by alternating hollow pillars with two different inner radii. It is able to transport two different wavelengths through the same channel, as clearly observed in the displacement fields in figure 10(b). The wave transmission originates from evanescent waves that allow for the overlapping of the elastic fields between two next nearest neighbor hollow pillars with the same inner radius. In figure 10(b), the displacement fields at two different passing frequencies are exhibited, where the enhancement of the fields inside the corresponding hollow pillars is obviously observed for each frequency.

Other ways to obtain a high-quality-factor pass band may also be realized based on WGMs, for instance by designing a cavity oriented perpendicularly to the direction of propagation [68]. It is worth noting that such applications of WGMs can also be realized inside a low-frequency hybridization band gap instead of a Bragg gap [68].

#### 2.4.2. Tunable properties by liquid filling of hollow pillars.

The existence of hollow pillars provides the possibility of filling them with a liquid. As the liquid and solid parts are coupled, the frequencies of the WGMs are affected by the acoustic

properties of the liquid (e.g. the type of the liquid and its temperature) as well as its height level inside the hollow pillar. In general, for a given inner radius, increasing the height level of the liquid will decrease the frequency of the WGM; however, there is room for anomalies. For example, for a given inner radius and height level of the liquid, the frequency of the WGM is lower when the liquid is mercury than that when it is water—since the impedance of mercury is much higher than that of water [69].

The liquid-filled hollow pillars will also give rise to new localized modes inside the band gaps, such as compressional modes of the liquid. Figure 11(a) shows the dispersion curves of a phononic crystal where the hollow pillars are fully filled with water. In this example, the height of each pillar is  $h/a = 0.4$ , the outer and inner radii are respectively  $r/a = 0.4$  and  $r_i/a = 0.1$ , and the plate thickness is  $e/a = 0.1$ . The parameters of water are taken at room temperature ( $25^\circ\text{C}$ ), namely a density of  $998\text{ kg m}^{-3}$  and an acoustic velocity of  $1490\text{ m s}^{-1}$ . In figure 11(a), the new blue and cyan bands appear in addition to the black bands associated with the solid. The pressure fields for these two bands reveal that they respectively correspond to the first compressional mode (blue band) and the second compressional mode (cyan band). This can be well explained by the simple physical model of a tube of height  $h_{\text{liq}}$  with rigid lateral and bottom boundaries and a free upper boundary. The expression of the  $(n+1)$ th compressional mode is  $f_{n+1} = (2n+1)c_{\text{liq}}/4h_{\text{liq}}$ , where  $n$  is the resonant integer number as  $0, 1, 2, \dots$  and  $c_{\text{liq}}$  is the acoustic velocity of the liquid. One can easily notice that the frequency of the second mode is three times that of the first mode,  $f_2 = 3f_1$ , which is also verified by the blue and cyan bands in figure 11(a).

The liquid compressional modes have high quality factors and, owing to their sensitivity to acoustic velocity, they are good candidates for sensing applications. For instance, the acoustic velocity of water will increase when the temperature  $T$  rises. In figure 11(b), we show that the frequency of the second liquid compressional mode increases within the Bragg band gap when temperature rises from  $0$  to  $70^\circ\text{C}$ , demonstrating the application of this structure for temperature sensing in water [69]. In addition, this configuration may also be applied to other application fields involving a dependence with the acoustic velocity, such as the identification of molar ratio for a mixture of two different liquids. It is to be noted that a solid/liquid coupled mode can also be generated by liquid filling in the hollow pillars whose frequency is sensitive to both the height level of the liquid and the inner radius of the hollow part.

#### 2.5. Vibration of multilayer pillars

We show here an illustration of a phononic crystal made of an array of multilayered pillars for SAW control. Here, each pillar is comprised of a periodic stack of alternating layers as seen in figure 12(a). We refer to this as a *phononic pillar*. The yellow layers correspond to polymethyl methacrylate (PMMA) and the blue ones to silicon. The novelty of this structure is that the pillar in the unit cell behaves like a 1D phononic crystal, so it allows band gaps that prohibit wave propagation along the

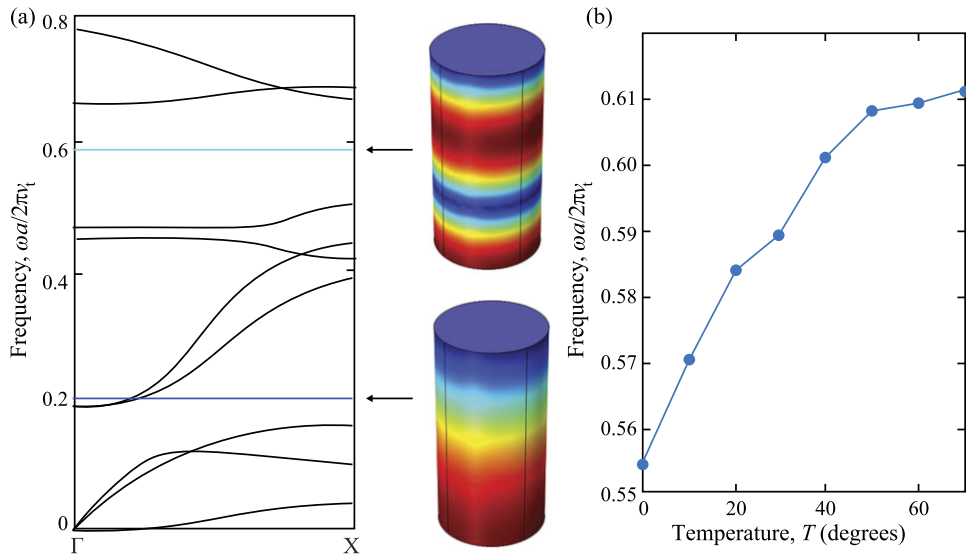


**Figure 11.** (a) Dispersion of a hollow pillar unit cell fully filled with water. The first and second liquid compressional modes are displayed in blue and cyan bands, respectively, along with the corresponding pressure fields. The blue and red colors stand for 0 and max values, respectively. (b) Temperature sensing application of the second compressional mode. This figure is based on results from [69].

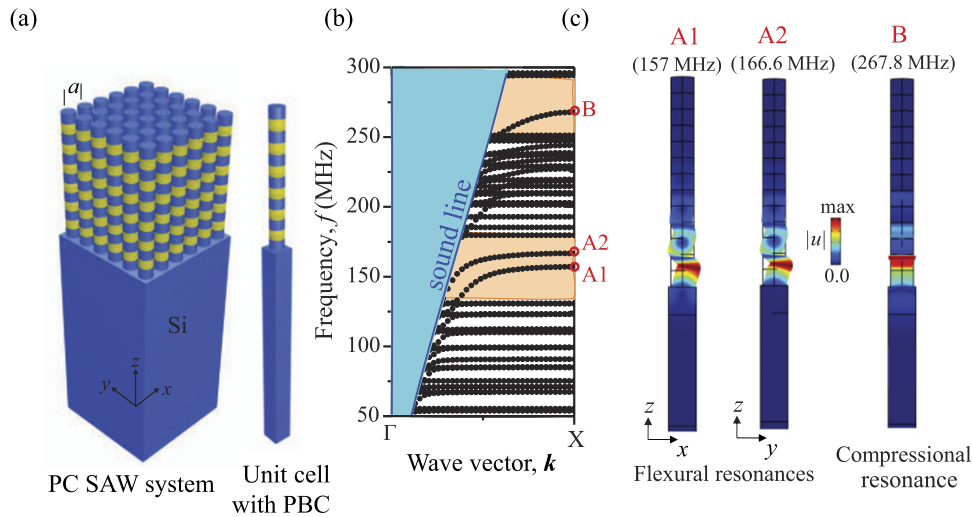


**Figure 12.** (a) Phononic crystal structure consisting of a square array of multilayer phononic pillars on a silicon substrate surface. The yellow and blue layers correspond to PMMA and silicon, respectively. The set of geometrical parameters are  $a = 1 \mu\text{m}$ ,  $h = h_{\text{silicon}} = h_{\text{PMMA}} = 3.5 \mu\text{m}$  and the pillar diameter is  $d = 5 \mu\text{m}$ . (b) Band structure for SAW propagation along the  $\Gamma X$  direction. (c) Total displacement field in the unit cell for modes denoted A1, A2, and B in (b). Reprinted figure with permission from [105], Copyright (2018) by the American Physical Society.

pillar’s vertical axis. Therefore, it can support localized modes in a cavity or at its top surface that are very well confined and can interact with the SAWs of the substrate to give rise to Fano resonances or other sharp features relevant for sensing applications.

Figure 12(b) represents the corresponding dispersion curves in the  $\Gamma X$  direction within the Brillouin zone. Below the silicon sound line, the modes are localized at the surface of the silicon substrate and/or inside the pillars. However, among these modes, three specific modes noted A1, A2, and B appear in the orange shaded regions which correspond to the band gap of the periodic multilayer pillars. In contrast, the displacement fields of the other SAW branches are distributed throughout

the pillars. The displacement field amplitude together with the vibration of these three modes plotted in figure 12(c) show that their vibrations are mainly localized at the bottom of the pillar, i.e. at the interface of the pillars with the substrate. Moreover, one can see that the motions of modes A1 and A2 resemble the bending vibrations of the pillar, while mode B looks like a compressional vibration.

Next, we consider one row of such pillars arranged on the surface and study the interaction of an incident Rayleigh wave with this line of pillars as shown in figures 13(a) and (b). The transmission spectrum plotted in figure 13(c) shows SAW attenuation in the shaded region where the amplitude of the  $u_z$  component decreases to 0.4 at 161 MHz. The shaded area

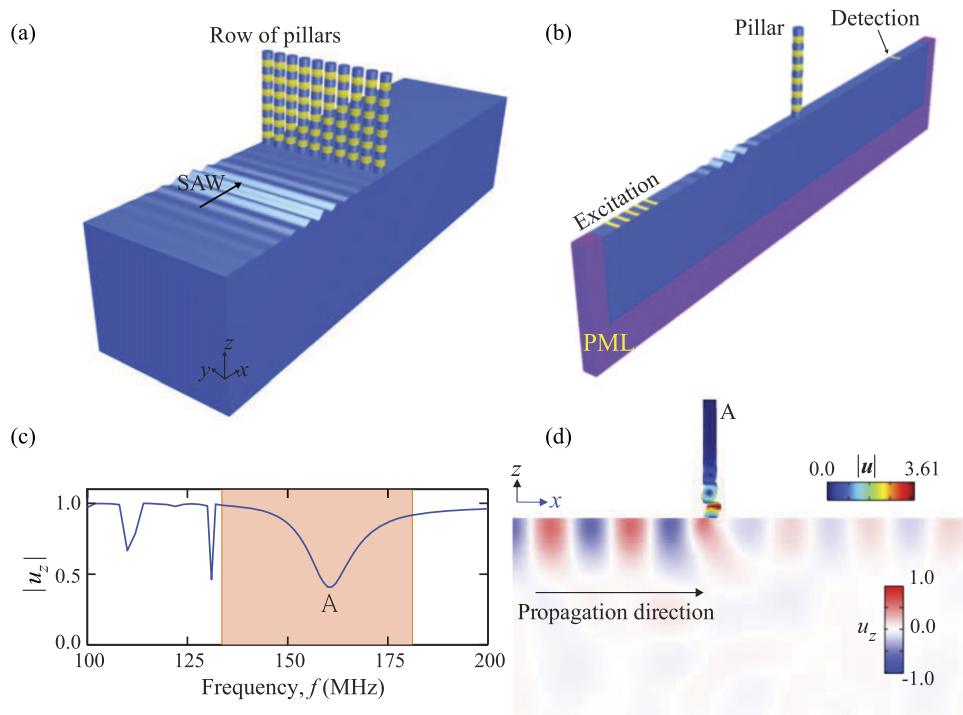


**Figure 13.** (a) Schematic view of the transmission through one row of phononic pillars. (b) Unit cell used in the simulation. (c) Transmission results: normalized amplitude of out-of-plane displacement  $u_z$ . The shaded region corresponds to the band gap of the PMMA/Si pillar. (d) Total displacement field in the pillar as well as the  $u_z$  component in the silicon substrate for SAW. Reprinted figure with permission from [105], Copyright (2018) by the American Physical Society.

corresponds to the band gap of the phononic pillar. At this frequency, we plot in figure 13(d) the total displacement field in the phononic pillar as well as the  $u_z$  component in the substrate. We deduce that the SAW attenuation is caused by the excitation of a localized mode as the confined mode denoted A1 in figure 12(b). This mode is localized at the bottom of the pillar.

## 2.6. Pillared plate encompassing multiphysics

The simultaneous existence of photonic and phononic band gaps and the confined phonon–photon interaction has opened up the field of cavity optomechanics [201]. This section first provides a brief overview on the existence of *phoXonic* (dual phononic–photonic) band gaps in a material configuration comprised of a periodic array of pillars deposited on a plate of finite thickness [54]. Then, we give an example of the interaction between elastic waves and localized surface plasmon modes in a system of gold nanocylinders separated from a thin gold film by a very thin dielectric spacer of few nanometers [202, 203]. This model is used to investigate the efficiency of the coupling between an elastic deformation and the plasmonic modes.

**2.6.1. Dual phononic and photonic band gaps.** Here, we theoretically examine the simultaneous existence of phononic and photonic band gaps in a periodic array of silicon pillars deposited on a homogeneous thin silica plate. Square, triangular, and honeycomb lattices have been investigated. We discuss the most suitable cases for dual phononic–photonic band gaps, especially in comparison to the traditional structures made out of periodic holes in a plate. The calculations are focused

on a structure where silicon pillars are deposited on a silica plate. Besides the technological interest in silicon structures, the selection of these materials is also important for the simultaneous existence of phononic–photonic band gaps. The existence of phononic gaps is not greatly affected by the choice of materials, as discussed earlier, although the frequency and width of the gaps are material-dependent.

In the closely related field of photonics, Johnson *et al* [204] have studied the band structure of a periodic array of silicon rods in air and shown the existence of a band gap for odd symmetric modes only (in a plane magnetic field). However, in this work, the height of the pillars was taken as equal to two times the lattice parameter and the result displayed similarity with the case of an infinite 2D structure where only a transverse magnetic gap can be created. It is observed that decreasing the height of the rods to values lower than the lattice parameter allows the opening of a complete photonic gap for the guided modes. Therefore, one can expect that the low refractive index of  $\text{SiO}_2$  may enable us to keep such a property even in the presence of the thin plate. In reference [54] a detailed study of both the phononic and photonic band structures was conducted. A search for the situations displaying band gaps for both excitations was also reported [54]. In figure 14, we give an illustration of the dispersion curves for the three types of lattices investigated: namely, square, triangular, and honeycomb. In these figures, the reduced (dimensionless) frequency is defined as  $\Omega = \omega a / 2\pi v$  where  $a$  is the lattice parameter and  $v = c_{\text{light}}$  is the velocity of light in vacuum for electromagnetic waves and  $v = v_t$  is the transverse velocity of sound in silicon for elastic waves. It can be seen that it is more suitable to search

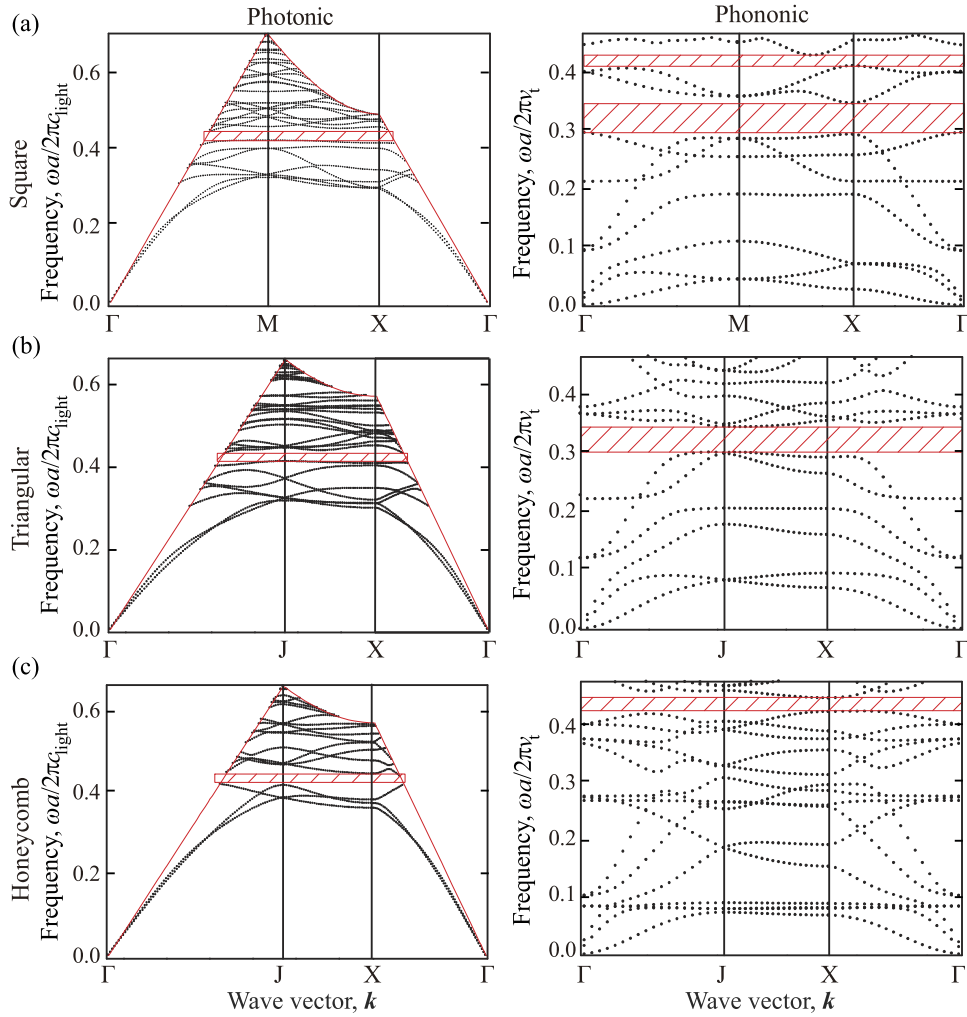


**Figure 14.** Photonic (left) and phononic (right) dispersion curves calculated for (a) a square array with the set of parameters  $ea = 0.2$ ,  $h_{Si}/a = 0.8$  and the filling fraction as 0.4, (b) a triangular array with the set of parameters  $ea = 0.5$ ,  $h_{Si}/a = 0.8$  and the filling fraction as 0.5, and (c) a honeycomb array with the set of parameters  $ea = 0.4$ ,  $h_{Si}/a = 0.7$  and the filling fraction as 0.3. Reprinted figure with permission from [54], Copyright (2010) by the American Physical Society.

for a photonic gap around or below the reduced frequency 0.4, since above this range the band gap will be restricted only to a small part of the Brillouin zone below the light cone. The actual frequencies in figure 14 are inversely proportional to the lattice parameter. To give a practical example, one can focus on a device operating at the telecommunication wavelength around 1550 nm for the optical waves. Then, all the other geometrical parameters become fully determined and the acoustic band gaps fall in the range of a few gigahertz. For instance, in the case of the square lattice, the geometrical parameters become: lattice constant  $a = 682$  nm, radius and height of the pillars  $r = 245$  nm and  $h = 546$  nm, and thickness of the  $\text{SiO}_2$  plate  $e = 136$  nm. The corresponding photonic and phononic band gaps, respectively, occur in the range 1508–1590 nm and 2.51–3.0 GHz. More details for the other lattices are given in [54]. In particular, it is shown that the triangular lattice provides the best flexibility for the choice of geometrical parameters. Moreover, unlike the square lattice, the triangular and honeycomb lattices do not require a very thin layer of  $\text{SiO}_2$ .

**2.6.2. Elastoplasmonic interaction.** First, let us note that a great level of attention has been devoted to the study of localized surface plasmons that can be supported by metallic nanoparticles due to their high abilities to confine and enhance electromagnetic waves in subwavelength volumes [205]. In the case of pillared-type structures, plasmonic designs have been realized to cover a wide range of optical resonances [39] and even to manipulate heat generation depending on the pillar aspect ratio [206]. Furthermore, mechanical vibrations of metallic nanoparticles [39, 207, 208] or plasmonic molecules [209] have been investigated by exploiting phonon–plasmon interactions.

Here, we provide an illustration of the theoretical and numerical investigation of the coupling between elastic and localized surface plasmon modes in a system of gold nanocylinders separated from a thin gold film by a dielectric spacer a few nanometers thick [202, 203]. This system supports plasmon modes confined between the bottom of the nanocylinder and the top of the gold film, which arise from

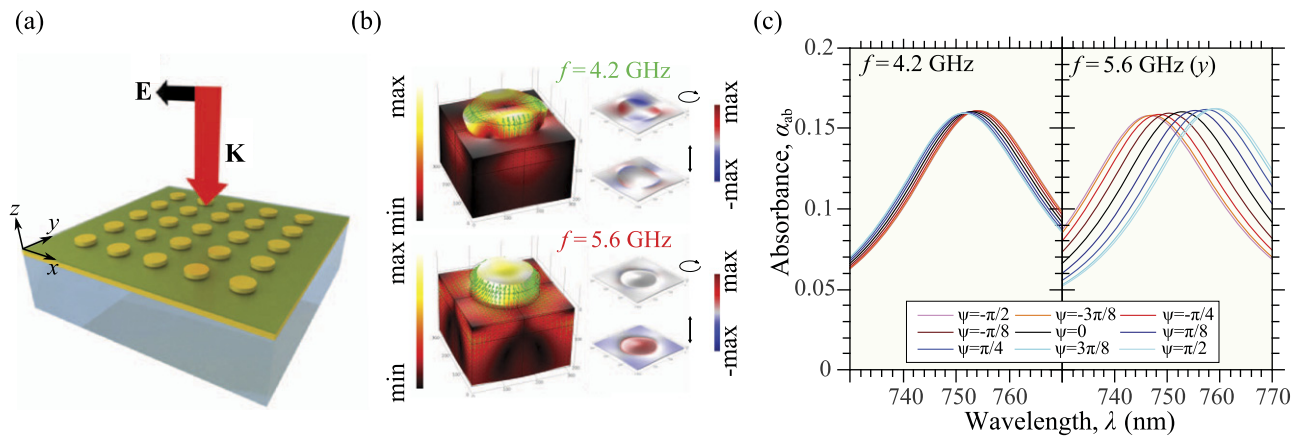


**Figure 15.** (a) Geometry of the model. (b) Elastic modes at two frequencies where the left is the total displacement field and the right is the deformation under the pillar. (c) Evolution of the absorbance spectra for different values of the elastic phase for the elastic modes at 4.2 and 5.6 GHz, around the wavelength of the main  $(n, p) = (1, 2)$  MIM-LSP mode. Reprinted figure with permission from [202], Copyright (2016) by the American Physical Society.

the formation of interference patterns by short-wavelength metal-insulator-metal propagating plasmons. The deformations induced by the elastic vibrations periodically modify the plasmonic properties such as absorption spectra or eigenvalues. Hence, these properties are modulated at the period of the elastic mode. The highest coupling rates are obtained for those elastic modes that produce the strongest modulations of the plasmonic features.

The structure is displayed in figure 15(a), and consists of a square array of gold nanopillars deposited on a multilayered membrane composed of gold and silica. The simultaneous consideration of the plasmonic, elastic, and coupled elastoplasmonic aspects has been numerically studied using the finite-element method. In order to characterize the elastoplasmonic interaction, we use a quasistatic approximation, which consists of a recalculation of the shape of the elastic modes at several selected instants of an elastic period (or several selected phases) where the shape of the structure is fixed at these instants. This is justified by the fact that the plasmonic frequency is several orders of magnitude larger than the elastic frequency.

Figure 15(b) shows two elastic modes at  $f = 4.2$  GHz and  $f = 5.6$  GHz (adopting the notation used in [202]), which correspond to a quadrupolar mode and a vertical compressional mode, respectively. The incident visible light is launched normally to the substrate as shown in figure 15(a). The evolution of the absorbance spectrum around the wavelength of the metal-insulator-metal localized-surface-plasmon (MIM-LSP) mode at 750 nm for these two modes is shown in figure 15(c). The deformed geometry of each mode is calculated for different phases  $\psi = \omega t = 2\pi ft$  during half an acoustic period. At 4.2 GHz, the mode has observable modifications in the absorption spectrum for different phases. More obvious modifications are induced for 5.6 GHz in the range of wavelengths where the MIM-LSP modes are excited. Indeed, the latter elastic mode produces an efficient compression and dilatation of the dielectric spacer

between the Au film and the Au nanocylinder, hence producing a significant modulation of the localized plasmon mode frequency.

This study may highlight the coupling mechanisms between localized plasmon modes and elastic modes, which is based primarily on the fact that the localization of the elastic vibrations and the plasmon resonance occurs in two different parts of the structure; namely, the ‘elastic function’ [202, 203] is mostly supported by the gold nanoparticle while the ‘plasmonic function’ is essentially supported by the dielectric cavity under the nanoparticle. This aspect, which is in contrast to previously investigated systems, gives additional flexibility for the engineering of elasto-plasmonic devices with the possibility of loading or changing the volume of the nanoparticle in order to tune the frequencies of elastic modes without significantly affecting the plasmonic aspects. Furthermore, the interaction between the elastic and plasmonic modes may be influenced by using spacers with different mechanical properties but similar refractive indices. Finally, this work was recently extended to the interaction between localized plasmon and propagating SAWs (referred to as Rayleigh–Sezawa waves) to show that some of the latter may also provide a strong phonon–plasmon coupling [203].

### 3. Pillared metaplates: advanced geometric configurations

#### 3.1. Engineering of large low-frequency band gaps

**3.1.1. Trampoline metamaterials.** In most applications in phononics, including metamaterials and metasurfaces, a large band-gap size is generally desirable. Maximization of band-gap size by unit-cell optimization has been actively pursued for phononic crystals [38, 40, 41, 63–66, 210–213]; in contrast, less attention has been focused on band-gap widening in locally resonant acoustic/elastic metamaterials. In this subsection, we review the dispersion characteristics of locally resonant elastic metamaterials formed by the erection of pillars on the solid regions in a plate patterned by a periodic array of

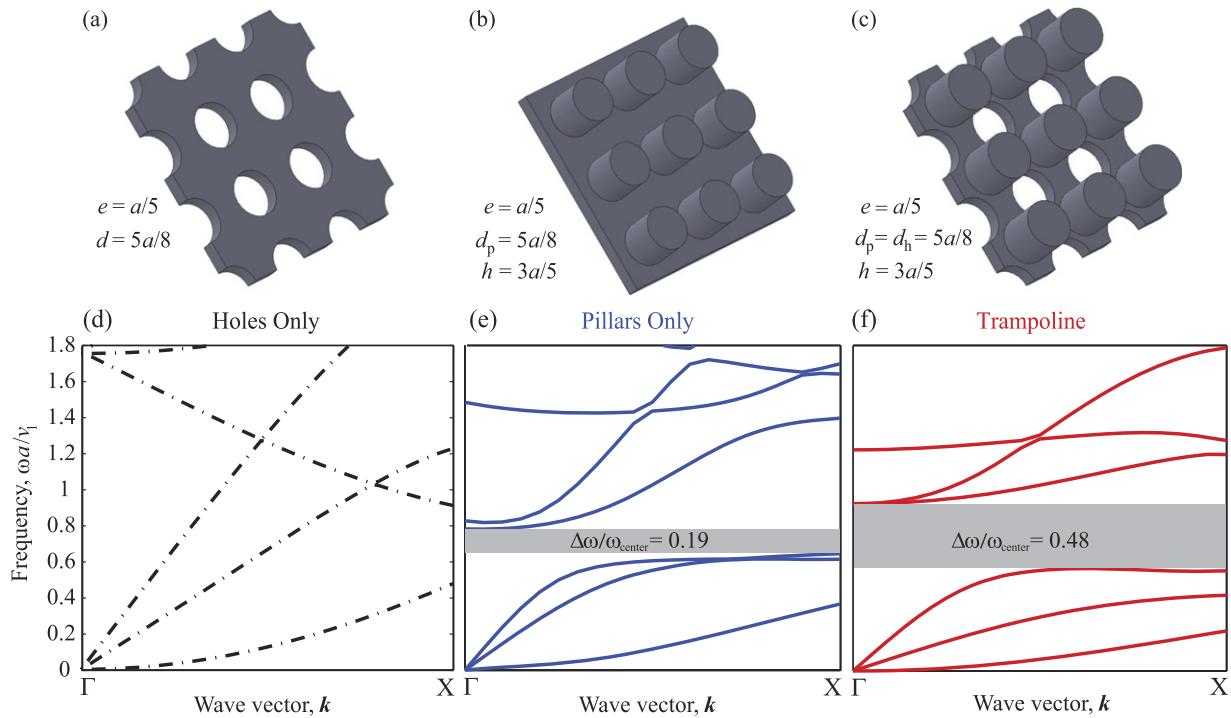


**Figure 16.** Demonstration of a trampoline metamaterial. The top panel shows schematics of (a) a standard phonic crystal plate (consisting of a periodic array of holes), (b) an elastic metamaterial in the form of a periodic array of pillars on a plate, and (c) a trampoline metamaterial consisting of a periodic array of pillars on a plate intertwined with a periodic array of holes. Hole and pillar diameters are denoted  $d_h$  and  $d_p$ , respectively. The solid material is silicon with properties: density  $\rho = 2330 \text{ kg m}^{-3}$ , and Lamé constants  $\lambda_L = 85.502 \text{ GPa}$ ,  $\mu_L = 72.835 \text{ GPa}$ . The dispersion diagram for the three configurations for wave propagation in the  $\Gamma X$  direction is shown in the bottom panel with the frequency normalized with the respect to the longitudinal bulk velocity  $v_l$ . In the frequency range displayed, the phonic crystal has no band gaps. (d) The standard pillared plate exhibits a subwavelength band gap with a relative size of 0.19 (e), and the proposed trampoline plate features an enhanced subwavelength band gap with a relative size of 0.48. Reprinted from [75], with the permission of AIP Publishing.

holes [67]. The solid regions effectively act as springboards that enhance the resonance behavior by the pillars when compared to the nominal case of pillars on a plate with no holes. This local resonance amplification phenomenon, which has been defined as the *trampoline effect*, has been shown to cause subwavelength band gaps to increase in size by up to a factor of 4.

To demonstrate the trampoline effect, we will examine a plate configuration formed by the merger of a periodically pillared plate foundation (figure 16(b)) with a standard phonic crystal plate created by removal of a periodic array of holes (figure 16(a)) [67]. The outcome is a locally resonant elastic metamaterial consisting of pillars standing on the solid regions of a phonic crystal plate (figure 16(c)). This architecture allows each pillar to be rooted in a more compliant base due to the presence of the holes, thus rendering the base to behave effectively as a springboard that allows the pillars' resonant motion to be enhanced. This enhancement is reflected in the relative size of the locally resonant subwavelength band gap, which is seen to experience an enlargement in size by a factor of approximately 2.5 compared to the pillared plate with no holes.

To further examine the trampoline effect, the problems shown in figures 16(b) and (c) were extended for a range of values of pillar height and hole diameter. A map of the size and location of the lowest band gap (also along the  $\Gamma X$  direction)

as a function of pillar height for a hole diameter of  $d_h = 5a/8$  is given in figure 17(a). The same results are also presented in figure 17(b) but in the form of a plot of the relative band-gap size  $\Delta\omega/\omega_{\text{center}}$  versus pillar height, where  $\omega_{\text{center}}$  is the band-gap central frequency. The blue solid line in figure 17(b) is for the standard, unholed pillared plate and is provided for comparison. The dotted, dashed, and solid red lines represent the relative band-gap size for the trampoline metamaterial configuration for different values of  $d_h$ . In addition to  $d_h = 5a/8$ , two other hole diameters are considered,  $d_h = 3a/8$  and  $d_h = 4a/8$  (noting a constant increment of  $a/8$  between the three diameters). It is observed that for the two additional trampoline plate cases, the relative band-gap size is larger than the case of the standard unholed pillared plate. This shows that the trampoline effect is present also in the lower-hole-diameter cases. However, the incremental enlargement of relative band gap size is more significant at higher values of hole diameter, which is due to the quadratic decrease in the springboard area as  $d_h$  is increased.

The increase in relative band-gap size attainable by the trampoline effect is remarkable. For the parameter set of  $d_h = 5a/8$  and  $h_p/a = 0.4$ , the size of the relative band gap is close to 0.6 (i.e. 60%). This is a significant improvement over reported relative band gap sizes in the literature for acoustic/elastic metamaterials in general and specifically for pillared metamaterials, which usually fall within the range

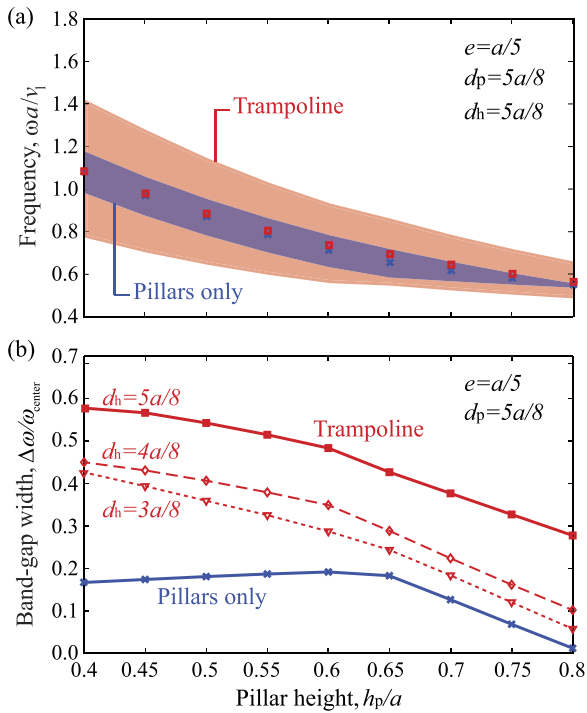


**Figure 17.** Map of absolute (a) and relative (b) band gap as a function of normalized pillar height for a trampoline plate (consisting of pillars and holes) compared to a standard pillared plate (consisting of only pillars). In (a), the shaded region represents the size and location of the lowest band gap. The trampoline effect results in an increase of the subwavelength locally resonant band gap by a factor ranging from roughly 2 to 4 for geometries, where the original  $\Delta\omega/\omega_{\text{center}}$  is greater than or equal to 0.1. Reprinted from [75], with the permission of AIP Publishing.

of 20%–30% for a partial band gap in single-sided pillared plates. The trampoline effect may be enhanced even further by introducing pillars on both sides of the plate, where partial band gaps exceeding 50% were reported in the absence of the trampoline effect [63].

These results demonstrate that the trampoline effect in a plate facilitates the utilization of subwavelength metamaterial properties over relatively broader frequency ranges than in the case when only pillars are employed.

**3.1.2. Tailored metamaterials.** In the previous section, trampoline metamaterial plates were reviewed as a concept for widening and lowering a local resonance hybridization band gap. In this section, we discuss a mechanism to significantly widen the Bragg band gap and extend it to the low-frequency domain; meanwhile, the relative width of the low-frequency hybridization band gap is also enlarged. The physical model is based on the pillared unit cell configuration of section 2.4.1. As seen in the inserts of three geometries in figure 18, the pillars are connected to each other by cross bars with tunable widths instead of the use of a homogeneous plate as a common base medium. The widths of the bars are  $b/a = 1, 0.5,$  and  $0.1$  at the left, middle and right panels, respectively. The lattice constant is  $a$ . The entire unit cell in this example is made of silicon.

To explain the mechanism behind the trend observed in figure 18, let us first start with the case  $b/a = 1$ . A Bragg

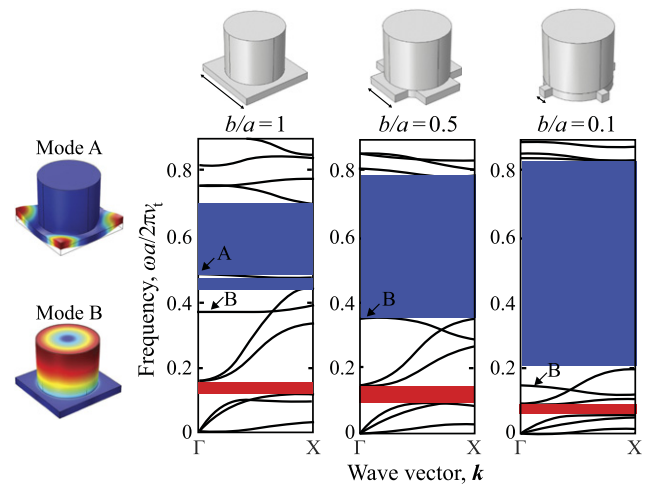


**Figure 18.** Dispersion for pillared phononic crystals connected by thin bars with widths  $b/a = 1$  (left),  $0.5$  (middle), and  $0.1$  (right). The Bragg and hybridization band gaps are respectively marked in blue and red. The geometries of the unit cells are displayed on top of each dispersion curve. The eigenmodes of bands A and B at the  $\Gamma$  point are also represented on the left where the blue and red colors stand for 0 and max values, respectively. Reproduced from [70]. © IOP Publishing Ltd. All rights reserved.

(blue) and a hybridization (red) band gap appear in the dispersion curves along the  $\Gamma X$  direction with relative sizes 0.45 and 0.26, respectively. The relative size of a band gap is defined as  $\Delta\omega/\omega_{\text{center}}$ , where, as defined earlier,  $\Delta\omega$  is the width and  $\omega_{\text{center}}$  the central frequency of the gap. The Bragg band gap is divided into two parts by a narrow band denoted A, for which the eigenmode at the  $\Gamma$  point is also displayed in figure 18. One can clearly notice that this branch A exhibits a high localization in the plate at the four corners of the unit cell. In addition, a relatively flat band B falling in the frequency domain of the bulk bands below the Bragg gap is associated with the torsional resonance of the pillars, as seen from its eigenmode. The presence of band A and the interaction between band B and other bulk bands affect the property of the Bragg gap. To eliminate these two effects, we propose the concept of a tailored metamaterial that consists of a pillar connected by two tunable crossing bars.

Indeed, when the width of the bar reduces to 0.5, the four corners of the unit cell turn into eight new corners of the two crossed bars. Since the distance of the two corners at one edge of the bar is equal to the bar width and decreases, the frequency of mode A moves to a higher frequency, about 0.85 for  $b/a = 0.5$ . Meanwhile, the torsional mode B downshifts to a lower frequency. These two changes result in a wider Bragg band-gap with a drop in the lower band-gap edge—the relative band-gap size increases to 0.76 as seen in the middle panel of figure 18. Meanwhile, the hybridization band gap is also enlarged slightly and moves to lower frequencies with a relative size of 0.41. When the width of the bar further decreases to 0.1, the Bragg band gap extends to the low-frequency domain and its relative size greatly increases to 1.22 while the relative size for the hybridization band gap increases to 0.52. The unit cell with narrow bars makes the pillar easier to rotate and bend, so that band B and the hybridization band gap exhibit

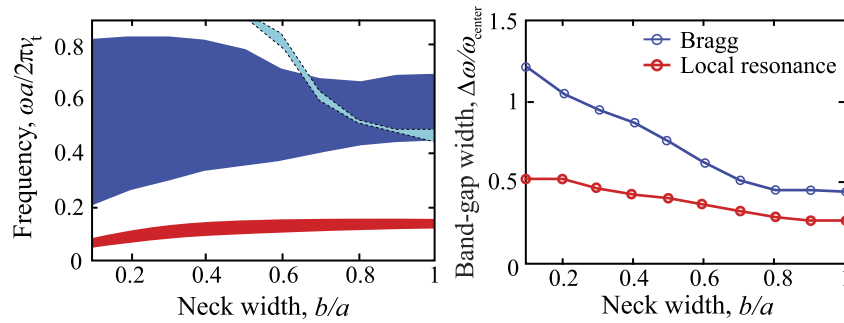


**Figure 19.** (Left) Evolution of the Bragg (blue) and hybridization (red) band gaps as a function of bar width  $b/a$ . Cyan represents band A. (Right) Relative size of band gaps as a function of bar width  $b/a$ . Reproduced from [70]. © IOP Publishing Ltd. All rights reserved

red shift. Such dispersion properties have potential for utilization in subwavelength studies of acoustic/elastic metamaterials. For instance, the torsional mode of the pillars can contribute to the realization of a negative effective shear modulus, which can be further explored for polarization filtering, mode conversion, and abnormal refraction [214].

The evolutions of the Bragg and hybridization band gaps in the  $\Gamma X$  direction as a function of the bar width are summarized in the left panel of figure 19, where band A is shown in cyan. As the bar width reduces, the frequency of mode A drifts outside the Bragg band gap. The Bragg band gap becomes much wider and remarkably extends to the low-frequency domain, hence becoming an extra-wide band gap. The hybridization band gap gradually moves to lower frequencies. The evolutions of the relative sizes of the two gaps are presented in the right panel of figure 19. Since the width of the Bragg gap obviously enlarges when the width  $b/a$  is smaller than 0.7, its relative size almost linearly increases, nearly three times for  $b/a = 0.1$  to 1. On the other hand, the relative size of the hybridization band gap gradually increases and becomes two times higher. As a result, engineering dispersion bands by tuning the width of the cross-connecting bars is proven to be an effective approach for widening and lowering band gaps.

### 3.2. Pillared GRIN phononic plate

**3.2.1. Introduction.** Focusing of acoustic or elastic waves via flat phononic lenses is definitely one of the most striking phenomena that arise from the artificial periodicity of phononic crystals. After the first experimental demonstration of the phenomenon was achieved in 2008 [215], intense activity has developed to optimize the geometrical and physical parameters of acoustical lenses in order to realize exceedingly high spatial resolution [216–221]. These promising perspectives for acoustic imagery relate to the key characteristic that phononic crystals are systems in which one can control the wave propagation at the wavelength scale, making it possible to overcome the diffraction limit. It should be noted that it is not possible for a conventional lens to produce an image containing details that are finer than half the wavelength of the light or sound being focused. This drawback applies regardless of the type of wave, electromagnetic or elastic/acoustic. This is a consequence of the evanescent waves that emerge from the object but that do not contribute to the resolution of the image because

of the exponential decay of their amplitude in any lens made of a positive-index material. In contrast, in lenses with negative index, the evanescent waves have their own amplitude that increases during the transmission through the medium. While the waves decay again down to their initial level after emerging from the lens, they can still contribute to the resolution of the image.

From the perspective of super-resolved imaging—which has emerged as one of the ‘hottest’ topics in the field—phononic crystals suffer from some drawbacks that may prevent them from wide dissemination. First, as a consequence of the exponentially decaying amplitude of the evanescent waves, the super-resolution attribute applies only to near-field imaging. Actually, if the source is located at a distance from the lens that is greater than one wavelength, the decay turns out to be prohibitive to the evanescent component reaching the lens and the super-focusing effect cannot be achieved. Then, in phononic crystals, the negative refraction of elastic waves, which is the starting point of the super-focusing effect, can be controlled through the band structure. In fact, this phenomenon is a direct consequence of band folding and therefore relates to the negative slope of some acoustic branches [222]; only elastic waves with frequencies above the first band gap can contribute to the superlensing effect. Their wavelengths are thus comparable to or even smaller than the period of the phononic crystal, and the propagation therein comes with large and even prohibitive scattering of the waves.

Using phononic crystals to focalize elastic waves with frequencies in the first branch of the Brillouin zone where negative refraction effects are not involved is, however, possible if considering *gradient-index phononic crystals* (GRIN PCs) [152, 223–233]. These 2D systems are engineered with a gradual variation of their constitutive parameters (e.g. filling factors [228, 232, 234], geometry of the inclusions [152], or material properties [223]) along one direction. As a result, they feature a sound velocity gradient along that direction, making it possible for collimation, convergence, or focalization of an incident wave. When an acoustic beam propagates through a 2D GRIN PC, it encounters redirection at every virtual interface between layers, resulting in successive reorientations of the acoustic beam inside the structure. Thus, by gradually modulating the parameters of a GRIN PC, one may create a curved path for the acoustic waves [152, 223, 225, 226, 228–232]. Inspired by

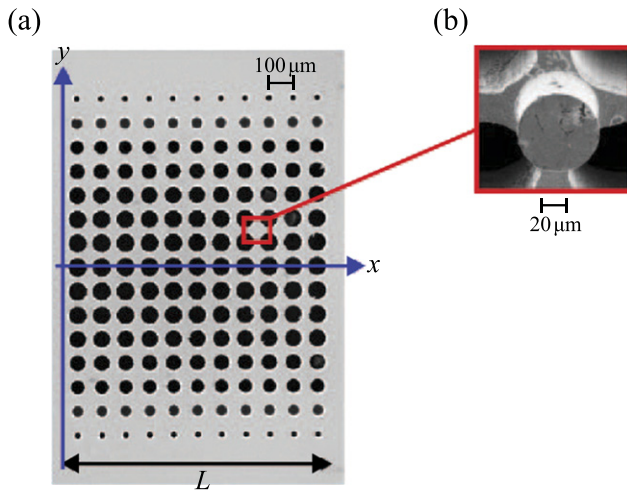


**Figure 20.** (a) Scanning electron microscope (SEM) image of the back side of a sample of a trampoline GRIN structure. (b) SEM image of a silicon pillar centered between four air holes on the front side of the sample. Reprinted figure with permission from [158], Copyright (2016) by the American Physical Society. The width of the sample is denoted by  $L$ .

optical devices that already exist, different designs for acoustic waves have been proposed, including Maxwell's fish eyes [235] and circular Luneburg lenses optimized for simultaneously focalizing the three elastic modes that may propagate in a plate, namely shear horizontal, symmetric, and antisymmetric Lamb modes [154]. However, whether it is for optical waves [236–238] or for elastic waves [152, 223, 228, 232, 234, 239] none of the proposed designs has allowed for overcoming the diffraction limit to date; this is because of total internal reflection of waves with high wavevectors  $k$ , which hinders the transmission to the background for external focusing. On the optics side, it was further proposed to use metamaterials featuring extraordinary refractive properties instead of photonic crystals [229, 231, 233, 240, 241], and the resolution beyond the diffraction limit for visible light was actually demonstrated analytically [240]. However, such success has not been obtained with elastic waves in solids so far [229, 231, 233, 241], nor has it been investigated how large the acoustic refractive index (i.e. ratio of the wave vector in the lens to the wave vector in the background) should be to attain this objective. Metamaterials with local resonances generally fulfill this latter requirement since they may display very slow sound velocity, at least near resonances [19, 26, 30, 75, 86, 96, 130, 131, 144, 221, 242–247]. Besides, depending on the shape and dimensions of the resonant inclusions, the resonances may arise at a very low frequency compared to the Bragg gap, in a region of the reduced Brillouin zone where effective theories apply. This has been demonstrated both theoretically and experimentally, with 2D phononic crystals made out of an array of cylindrical pillars regularly erected on a homogeneous thin slab [26, 86, 96, 130, 131, 144, 246]. This structure, in particular, deserves special attention. Indeed, a single pillar on a plate has compressional and bending resonances that may lead to the dynamic effective modulus and mass density both being negative when a number of them are

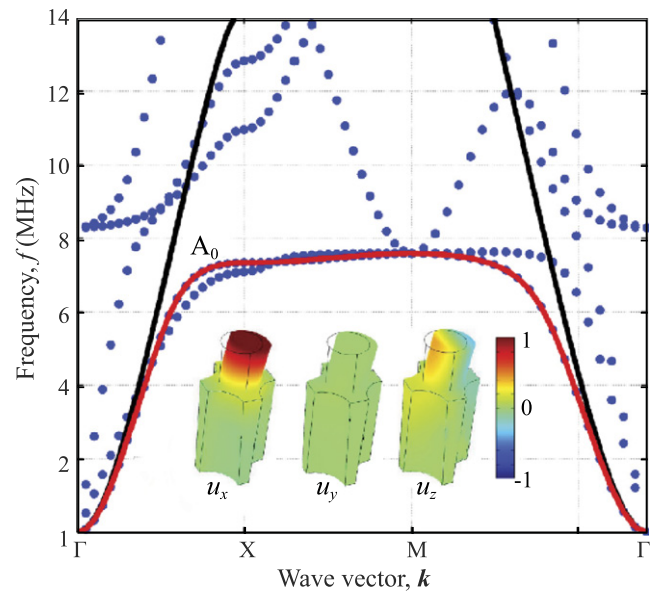


**Figure 21.** Band structure (dotted curves) of the trampoline GRIN structure along the central layer of the acoustic lens. The  $A_0$  band is highlighted by the overlapping red line while the black line indicates the  $A_0$  band along the central layer without pillars. Inset shows the normalized modal displacements of the  $A_0$  mode at the X point in the Brillouin zone. Reprinted figure with permission from [158], Copyright (2016) by the American Physical Society.

gathered to form a metamaterial. Moreover, since the compressional resonant frequency and the bending resonant frequency are mainly sensitive to the height and to the diameter of the pillar respectively, they can be tuned almost independently from each other [100]. When associated with a GRIN phononic lens on a plate, it is expected that the bending resonances and the Lamb waves propagating in the plate exhibit polarization coherency, thus allowing for the enhancement of the evanescent waves and, in turn, for the formation of a spot at the focus containing finer information.

**3.2.2. Beam path in trampoline GRIN structure.** Based on the GRIN phononic plate concept, Zhao *et al* [158] designed acoustic lenses built on a silicon plate by drilling a square lattice of air holes with a period of  $a$  and with radii gradually tailored along the transverse direction, as shown by the SEM image in figure 20(a). An array of identical silicon pillars was erected on one face of the plate, on each junction between each set of four air holes. This represents a combination of the trampoline metamaterial concept [75] and the GRIN concept. The basic unit is shown in figure 20(b). They have shown in reference [158] that such a structure, which we may describe as a *trampoline GRIN structure*, allows for the focalization of an  $A_0$  Lamb mode within the homogeneous substrate behind the metalens, over a spot with a transverse size beyond the diffraction limit.

In the low-frequency region, where the wavelength is much larger than the lattice parameter, the refractive index along each line of inclusions (i.e. the ratio of the wavenumber along  $\Gamma X$  to the wavenumber in the background) was designed to feature a hyperbolic secant profile. This profile, which can be for-

mally written as  $n^2(y) = 1 + (n_0^2 - 1) \operatorname{sech}^2(\alpha y)$  where  $\alpha$  is the gradient coefficient, and  $n_0$  is the refractive index along the central line of inclusions at the working frequency, allows for an exact determination of the acoustic rays. Moreover, a lens with an index featuring a hyperbolic secant profile is free of aberration, i.e. any ray normally incident on the lens converges to a single point on the axis [50, 212].

The band diagram of the trampoline GRIN structure shown in figure 21 explains the formation of a subwavelength spot at the focus of the lens. In this figure, the antisymmetric Lamb mode  $A_0$  is drawn for a structure with (red solid line) and without (black solid line) pillars. The inset displays the normalized modal displacements associated with the  $A_0$  mode for propagation along  $\Gamma X$  at the frequency of the red flat branch. Unambiguously, the hybridization between the  $A_0$  mode in the air/silicon phononic crystal, polarized on the  $x$ - $z$  plane, and the lowest-order flexural resonance of the pillar governs the displacement field—which is totally dominated by a vibration localized on the pillars.

It can be deduced from these dispersion curves that, at resonance, the pillars act as elastic sources emitting in the plate Lamb waves at the frequency of the bending eigenmode [100], which in turn allows for enhancement of the evanescent waves emerging from the lens.

Any ray normally incident on a GRIN lens featuring a refractive index with a secant hyperbolic profile converges to a single point on the axis, at the focal length  $f_{\text{length}}$ . This length only depends on the gradient coefficient  $\alpha$  through  $f_{\text{length}} = \pi/2\alpha$ . However, deviation between the focal distance predicted by this formula and that derived from numerical simulations, or even experimental measurement, may sometimes be significant, even in the homogenization frequency range [152, 223, 228]. There are several reasons for this possible deviation. First, the actual 2D acoustic lenses feature discretized indices, which may be imperfectly represented by a continuous gradient. However, this is probably not the most relevant reason since small deviations of a few percent were observed for a wavelength only five times larger than the period [152, 223, 228]. The observed disagreement between the theory and numerical simulations can be explained to a larger extent by the overall shape of the equifrequency contours (EFCs). Actually, in phononic crystals with large filling factors, the EFCs may depart from a circle, even at low frequency [152, 223, 228]; therefore, analyzing the trajectories in terms of an effective index may not be relevant. Instead, the effects of anisotropy are better described by considering both the group velocity and the  $\mathbf{k}$  vector as the local parameters [248]. Based on the same idea, a Hamiltonian optics approach has been proposed to study light propagation in graded phononic crystals in the short-wavelength regime [249]. However, there have only been a few theoretical works able to perform a quantitative analysis of the ray trajectory in the homogenization range [250]. This was done, for instance, in reference [251] where an empirical approach allowed accurate interpretation of both the position and the size of the spot experimentally measured in GRIN PC lenses with either a

square lattice (the holes have different diameters and are regularly spaced along the  $y$ -axis) or a rectangular lattice (the holes have identical diameter but their separating distance varies along the  $y$ -axis).

Experimental evidence of subdiffraction focusing with the trampoline structure is shown in figure 22(a). In this figure, the maximum of the out-of-plane displacement is measured on the free surface of the lens using an interferometric method. The displacement field is symmetric on both sides of the central layer at  $y = 0$ , with the overall maximum just behind the lens, at the distance  $x = 0.6a$  from the outlet interface. The agreement with the numerical simulations shown in figure 22(b), including both the focal position and the pattern of the displacement field, is excellent.

Figures 22(c) and (d) display experimental and numerical snapshots respectively recorded at a moment when the amplitude is at a maximum at the focus. The phase patterns in the two snapshots are in good agreement with each other. To further analyze the respective roles of the propagative and evanescent waves, the calculated ray trajectories are drawn in figure 22(c): the gray solid lines are for the wave with  $|k_y| < k_{\text{back}}$  along the exit interface ( $k_y$  is the component along the  $y$ -axis of the wave vector in the lens, and  $k_{\text{back}}$  is the wavenumber in the background), leading to propagative waves behind the lens, whereas the red dashed lines represent waves with  $|k_y| > k_{\text{back}}$ , resulting in evanescent waves in the background. The rays corresponding to the propagative waves converge to a small zone just at the focal position as shown by the experimental results in figures 22(a) and (c) and by the numerical results in figures 22(b) and (d), giving rise to an overall maximum displacement just behind the lens. Figure 23 depicts the transverse profile of the normalized maximum  $u_z$ , measured experimentally (circular markers), computed using a finite-element method (solid line), or analytically derived (dashed black line) [252].

The experimental data and the simulation and analytical results are in good agreement with each other. Actually, the full width at half maximum of the central peak equates to  $0.42\lambda_{\text{back}}$ ,  $0.43\lambda_{\text{back}}$ , and  $0.40\lambda_{\text{back}}$ , respectively, i.e. less than half a wavelength, and subdiffraction focusing is achieved. However, the analytical results differ from the other two through the lateral peaks, which are predicted to be smaller and sharper than it was experimentally and numerically found. Actually, it is assumed in reference [55] that there is identical contribution of each component  $k_y$  at the focus. However, in practice, the elastic waves undergo dissipation because of internal reflection and impedance losses at the interface. As a consequence, the normal displacements are smaller in the central portion of the lens  $|y| < 2.5a$  than they are in the edges  $|y| > 2.5a$  (figure 22(d)). In other words, the losses are larger when  $|k_y| < k_{\text{back}}$  than they are when  $|k_y| > k_{\text{back}}$  along the outlet interface. Accordingly, both in simulations and in experiments the focus gathers a rate of propagative (evanescent) waves smaller (larger) than that predicted by the theory; this leads to a focus along the  $y$ -axis featuring large side peaks.

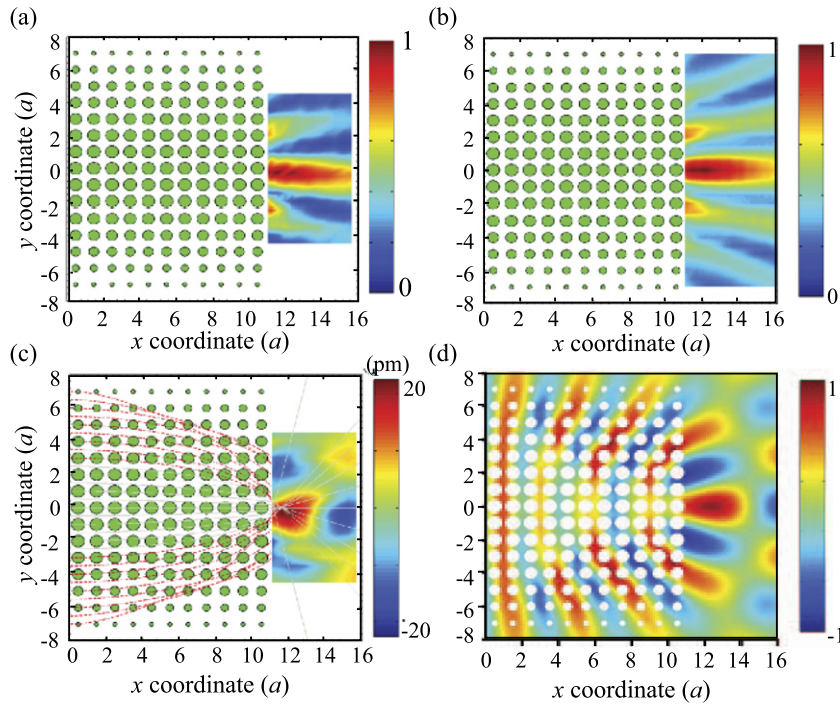


**Figure 22.** (a) Experimental and (b) numerical distribution of the normalized maximum  $u_z$  behind the acoustic lens at the X point in the Brillouin zone (7.2 MHz), together with (c) experimental and (d) numerical snapshots of the near field focusing at 7.2 MHz. (c) Gray solid lines and red dashed lines represent ray trajectories with  $|k_y| < k_{\text{back}}$  and  $|k_y| > k_{\text{back}}$ , respectively. Reprinted figure with permission from [158], Copyright (2016) by the American Physical Society.

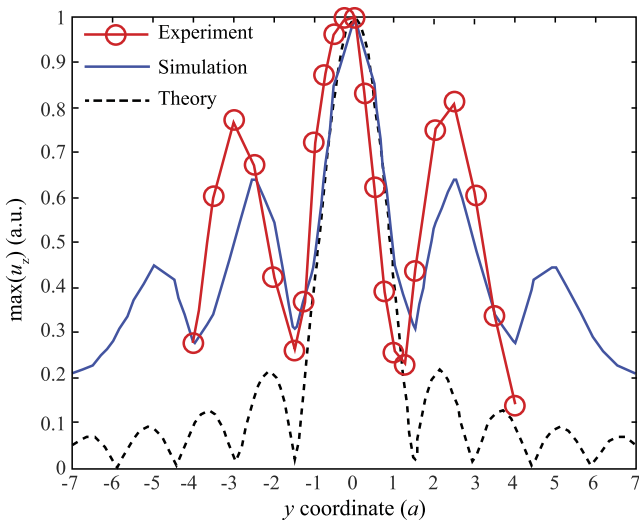


**Figure 23.** Experimental (circle markers), numerical (blue solid line), and theoretical (black dashed line) transverse profiles of the normalized maximum  $u_z$  at the focus. Reprinted figure with permission from [158], Copyright (2016) by the American Physical Society.

#### 4. Metalinge of pillars

A metalinge of pillars may be viewed as a planar metamaterial with a subwavelength thickness; it allows us to ‘shape’ arbitrary wavefronts by introducing in-plane variations in the wave responses. This has potential applications in practice such

as vibration isolation, ultrasonic detection, energy harvesting, and filtering, among others [253–255].

##### 4.1. Properties of a single pillar on a plate

**4.1.1. Basic model.** A pillar may exhibit bending (dipolar) and compressional (monopolar) resonances, which are related to negative effective mass density and elastic modulus for a pillared metamaterial [196]. The vibrational property of a single pillar deserves to be studied as it is the fundamental element of a pillared metastructure.

Let us consider a pillar deposited on a plate, as shown in figure 24(a). The whole structure is made of silicon. Four points are marked on top of the pillar where displacements are detected. We define two orthogonal states  $|\alpha\rangle$  and  $|\beta\rangle$  standing for a compressional and a bending mode, respectively. We assume that they can be combined into two other states  $|\psi_1\rangle = \cos\theta|\alpha\rangle + \sin\theta|\beta\rangle$  and  $|\psi_2\rangle = -\sin\theta|\alpha\rangle + \cos\theta|\beta\rangle$  with a coupling factor  $\theta$ . Then, the vibration on top of the pillar can be defined as  $|\psi\rangle = A e^{i\psi_1} |\psi_1\rangle + B e^{i\psi_2} |\psi_2\rangle$ . For a compressional mode, all points on top of the pillar have the same vibration, so that we can write the vibration of point 1 as

$$|\psi_{p1}\rangle = |\psi\rangle = [A e^{i\psi_1} \cos\theta - B e^{i\psi_2} \sin\theta] |\alpha\rangle + [A e^{i\psi_1} \sin\theta + B e^{i\psi_2} \cos\theta] |\beta\rangle. \quad (4.1)$$

For a bending mode, if the bending direction is along the point 1–point 3 line, the vibration of point 3 can consequently

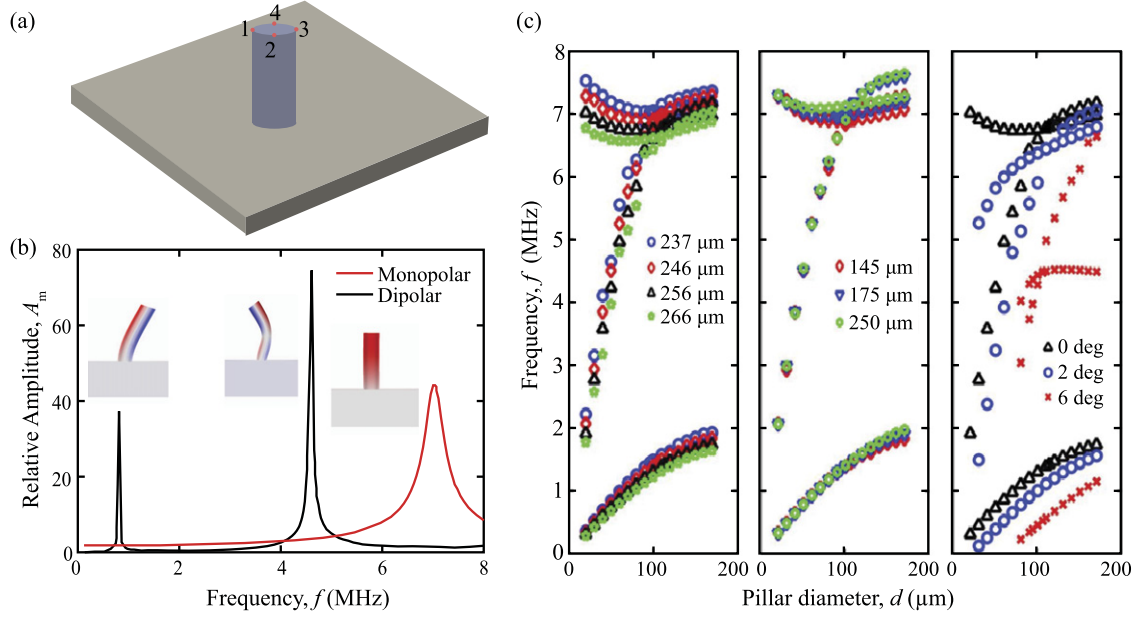


**Figure 24.** (a) Model for a single pillar on top of a plate, (b) resonant mode characterizations and (c) variations of three resonant modes against diameter and height of the pillar (left), thickness of the plate (middle), and conical angle of the plate (right). Reprinted figure with permission from [100], Copyright (2017) by the American Physical Society.

be written as

$$|\psi_{p3}\rangle = [A e^{i\psi_1} \cos \theta - B e^{i\psi_2} \sin \theta] |\alpha\rangle - [A e^{i\psi_1} \sin \theta + B e^{i\psi_2} \cos \theta] |\beta\rangle. \quad (4.2)$$

Therefore, we can further acquire

$$\frac{|\psi_{p1}\rangle + |\psi_{p3}\rangle}{2} = [A e^{i\psi_1} \cos \theta - B e^{i\psi_2} \sin \theta] |\alpha\rangle \quad (4.3)$$

$$\frac{|\psi_{p1}\rangle - |\psi_{p3}\rangle}{2} = [A e^{i\psi_1} \sin \theta + B e^{i\psi_2} \cos \theta] |\beta\rangle. \quad (4.4)$$

From the above two expressions of equations (4.3) and (4.4), we can recover the compressional and bending modes by considering the vibrations at points 1 and 3 with addition and subtraction computations [256].

As an example, we choose the geometric parameters: plate thickness 145  $\mu\text{m}$ , pillar diameter 50  $\mu\text{m}$ , and pillar height 245  $\mu\text{m}$ . The fundamental antisymmetric Lamb wave is excited with the wavefront perpendicular to the point 1–point 3 line. The out-of-plane displacement is detected at points 1 and 3, and operated on with equations (4.3) and (4.4) by normalizing to that of a point on a pure plate without the pillar. The first/second bending and compressional modes are clearly characterized by black and red solid lines in figure 24(b) with the associated vibrating motions, which provides a validation of the above method.

The resonant frequency of the pillar depends on the geometric parameters. From figure 24(c), the bending modes significantly depend on the pillar diameter, especially the second bending mode which will upshift to a much higher frequency, even overlapping the compressional mode, when the diameter increases. In addition, it is seen that the resonant frequency decreases with increasing pillar height, decreasing plate thickness, and increasing conical angle. The most salient feature

is that the frequencies of the second bending and compressional modes will superpose when the diameter of the pillar is around 100  $\mu\text{m}$ , which may provide some useful properties as discussed in the next section.

**4.1.2. Resonant and scattering properties.** When a pillar is in a resonant state, it scatters a wave radially. A scattered wave field can be acquired by subtracting the incident wave field from the total wave field. For the pillar displayed in figure 24(a), the frequency response of three key resonant states is shown in figure 24(b). Their scattered wave fields are derived and presented in figure 25, from where the dipolar and monopolar field properties are observed for bending and compressional modes, respectively. Therefore, the resonant pillar behaves as a point source.

**4.1.3. Huygens–Fresnel principle.** The Huygens–Fresnel principle is a well-known concept in the theory of diffraction which says that each point on a wavefront can be regarded as a secondary-point wave source. Conversely, the interference of a set of point sources will generate a wavefront whose function can be designed. As a simple example, in figure 26 we demonstrate that a line of identical point sources will generate a plane wavefront.

The phase and amplitude of a scattered wave by a compressional pillar mode are exhibited in column (a) upper and lower panels, respectively. Mathematically, five identical point sources are arranged in a line. The resulting field after interference is exhibited in column (b). The same operation but for nine identical point sources is done for column (c). The scattering field by a real line of nine resonant pillars is displayed in column (d). Comparing columns (c) and (d), one can observe that their scattering patterns are almost the same, which generates a plane wavefront as explained by the

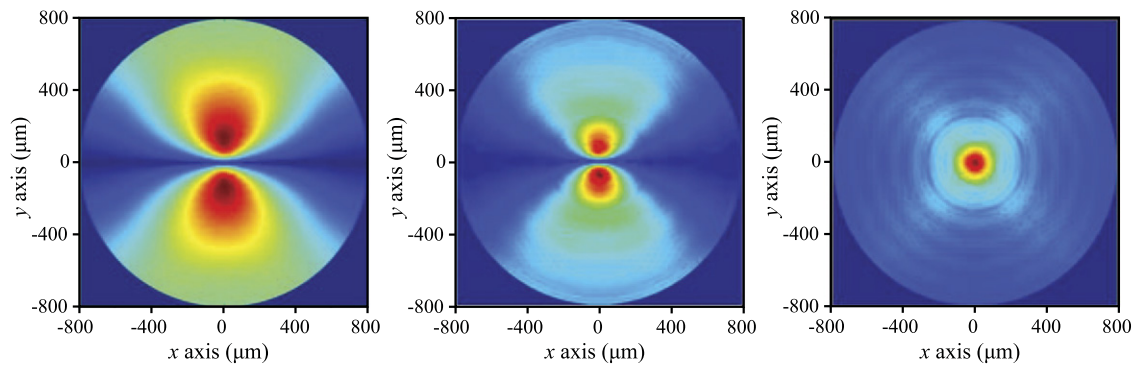


**Figure 25.** Amplitude distribution of the scattered Lamb wave by the pillar at the first (left) and second (middle) bending and compressional (right) resonant modes. The blue and red colors stand for 0 and max values, respectively. Reprinted figure with permission from [100], Copyright (2017) by the American Physical Society.

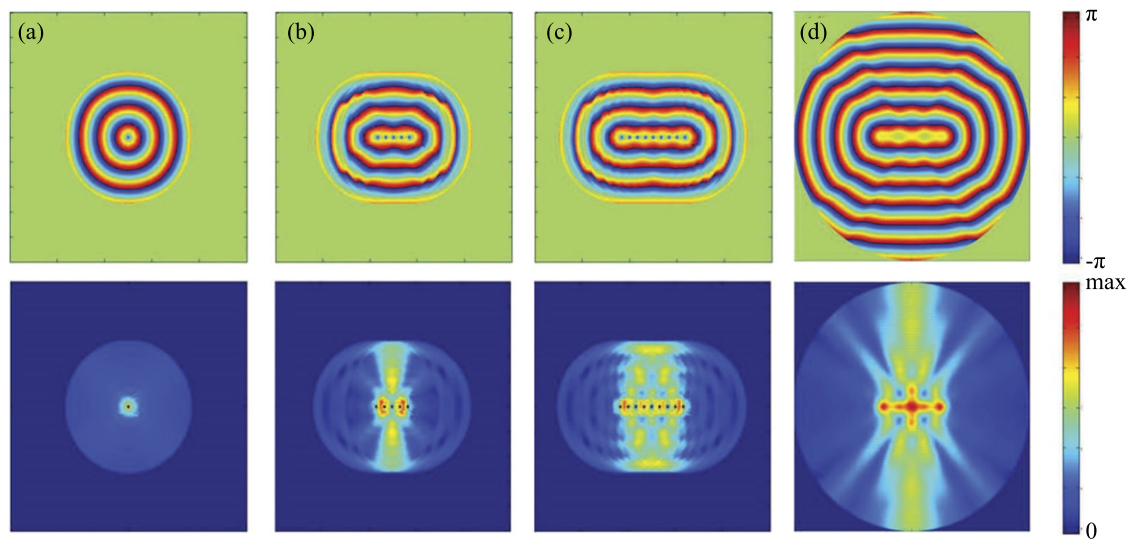


**Figure 26.** Phase (upper panel) and amplitude (lower panel) of the scattered wave for (a) a single pillar at a compressional mode; (b) adding five single sources with an inter-distance of  $200 \mu\text{m}$  numerically; (c) similar to (b) but for nine single sources; (d) one real line of nine pillars with an inter-distance of  $200 \mu\text{m}$ . Reprinted figure with permission from [100], Copyright (2017) by the American Physical Society.

Huygens–Fresnel principle. Any other functional wavefront can be designed by manipulating the phase distribution along the line, being a pillared metasurface.

#### 4.2. Properties of a metaline of pillars

**4.2.1. Metasurface by phase engineering.** Thanks to the Huygens–Fresnel principle, as demonstrated in the previous section, the properties of a line of pillars are discussed in this subsection. We first consider the pillar as in figure 24(b), with an internal distance of  $200 \mu\text{m}$ . The transmission curve and complex phase diagram of a scattered wave normalized to an incident wave are calculated in figure 27(a). One can see that three transmission dips occur corresponding to the first and second bending modes and the compressional mode, as marked in blue, black, and red, respectively. The three intrinsic modes produce ellipses in the complex phase diagram of the scattered field. In this complex plot, when a point is located at the  $+x$ ,  $+y$ ,  $-x$  and  $-y$  axes, this indicates that the phase of the scattered wave is  $0$ ,  $\pi/2$ ,  $\pi$ , and  $-\pi/2$ , respectively, with respect to the incident wave. The three ellipses are

symmetric with respect to  $-x$  axis, but cut the  $-x$  axis at different positions of  $x = -0.92$ ,  $x = -0.59$ , and  $x = -0.96$ , respectively. As the full wave field is a sum of incident and scattered waves, the transmission amplitudes are consequently  $0.08$ ,  $0.41$ , and  $0.04$ , respectively, after destructive interference between the incident and scattered waves.

The second bending mode and the compressional mode can be easily tuned to be superposed by adjusting the diameter, as already shown in figure 24(c). The overlapped mode characterization is displayed in figure 27(b) as black and red solid lines. Although the transmission curve still shows a dip for this superposed mode, the amplitude is much higher than their individual ones at  $0.57$ . From the complex phase diagram, the two ellipses merge into a bigger new ellipse that cuts the  $-x$  axis at  $x = -1.57$ , explaining the amplitude of transmission dip after destructive interference. It should be noted that the phase of the transmitted wave at the superposed frequency is out of phase with respect to the incident wave, which is different from separated modes. The out-of-phase property indicates that a line of pillars is possible for any possible phase within

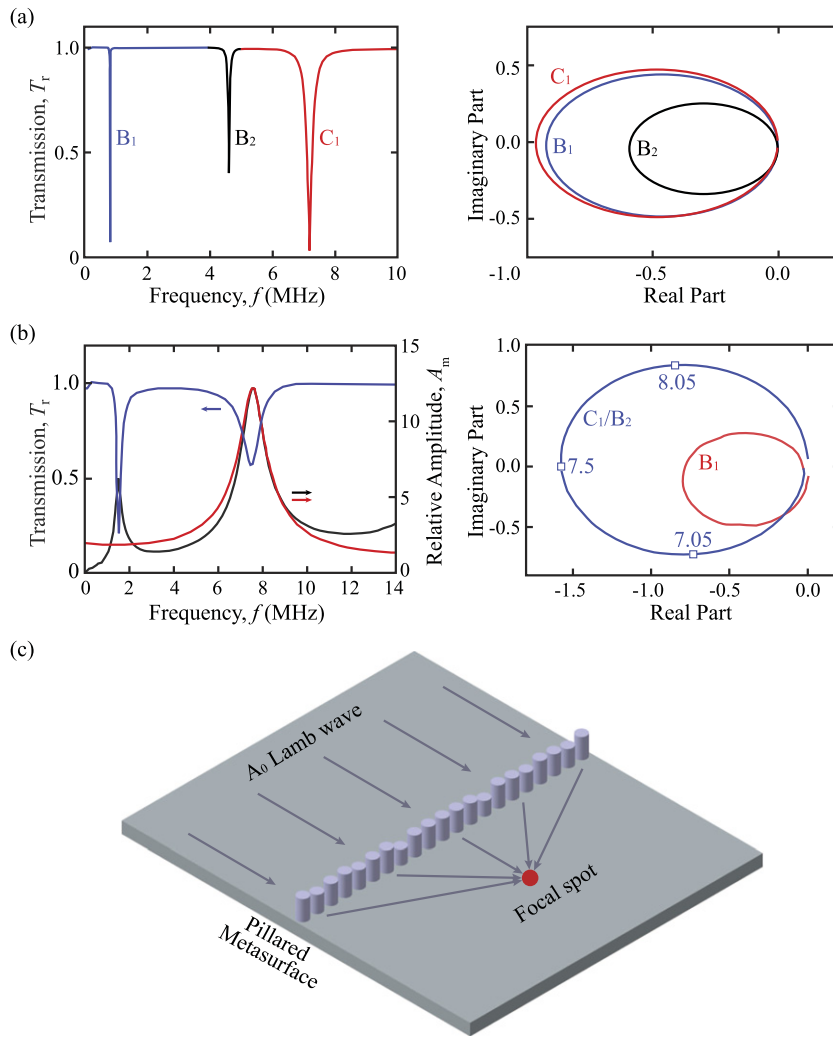


**Figure 27.** (a) (Left) Transmission curve for a line of pillars with three separate intrinsic modes. (Right) Complex phase diagram of the scattered field exhibiting three ellipses corresponding to the three modes. (b) (Left) Transmission and mode characterization curves for a line of pillars for which the second bending and compressional modes are superposed. (Right) Complex phase diagram of the scattered field exhibiting a bigger size ellipse that results from the superposition of the compressional and second bending resonances of the pillars. (c) Illustration of the focusing effect by a line of different pillars the phase of which is designed based on the generalized Snell’s law. Reprinted figure with permission from [100], Copyright (2017) by the American Physical Society.

the range  $[-\pi, \pi]$ ; thus, the generalized Snell’s law can be applied to efficiently design metasurface wavefront functions. The amplitude and phase of the transmitted wave can also be actively controlled by applying an external force on top of the pillar [257].

According to the generalized Snell’s law, the phase response can be locally designed nonlinearly along an interface between the two media, as any possible distribution profile according to the wavefront function’s requirement. In practice, the thickness of the ‘interface’ is much smaller than the working wavelength; thus, a ‘metasurface’ is named. As an example, figure 27(c) shows a line of pillars the local phase responses of which are designed according to a focusing function [258]. The pillared metasurface transfers the incident plane wave into focusing at the other side, being a promising direction for the manipulation of Lamb waves for compact applications [258]. The same function for bulk phononic crys-

tals and metamaterials requires the thickness size to be much larger than the working wavelength.

**4.2.2. Fano resonance and EIT/ATS.** In the previous section, the periodic spacing of the considered metasurface unit is  $200 \mu\text{m}$  with a pillar diameter of  $50 \mu\text{m}$ . Here, we first consider two pillars in the unit cell, which means the interval between two neighboring pillars is  $100 \mu\text{m}$ . Fano resonance appears in this system, originating from the coupling between the neighboring pillars, which results in an asymmetric profile in the transmission curve. If we fix one pillar’s height as  $h = 245 \mu\text{m}$  and change the other pillar’s height to  $h_j/h$ , the evolution of the two dips and the peak in the transmission curve is exhibited in figure 28(a), where the red solid line presents the resonant frequency of the fixed pillar and the green solid line presents the resonant frequency of the varying pillar. The corresponding quality factors are shown in the right panel of figure 28(b).

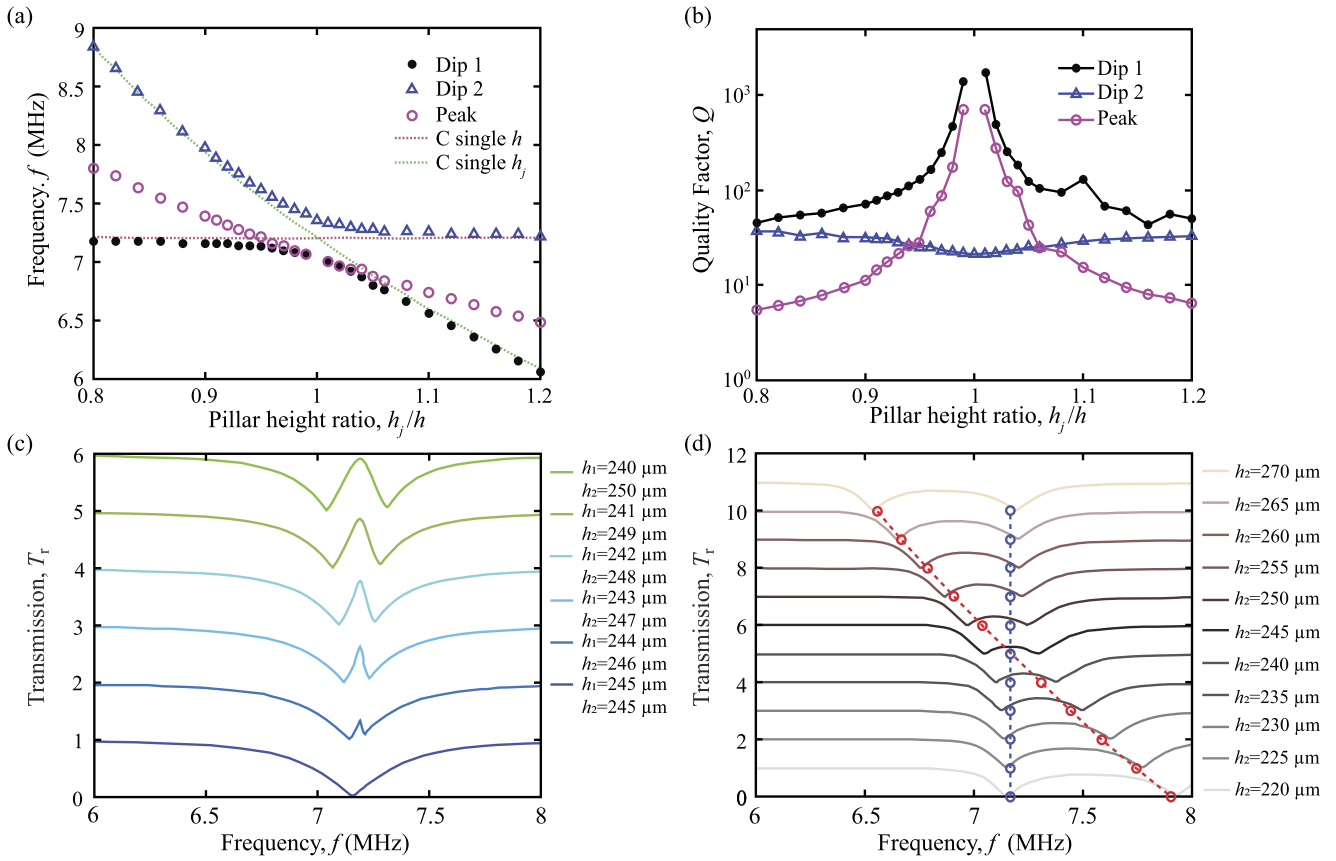


**Figure 28.** (Top) Pillared metasurface with two pillars in one unit cell with a lattice constant of  $200 \mu\text{m}$  (interval  $100 \mu\text{m}$ ): (a) evolution of dips and peak of Fano transmission profile by changing the height of the pillar  $j$  while fixing the height of the other pillar as  $245 \mu\text{m}$ ; (b) corresponding quality factors in (a). (a), (b) Reproduced from [98]. © IOP Publishing Ltd. All rights reserved. (Bottom) Pillared metasurface with two lines of pillars: (c) acoustic analogue of EIT with Fano interference by asymmetrically adjusting the two pillar heights while keeping the two-line distance as  $230 \mu\text{m}$ ; (d) acoustic analog of ATS without Fano interference where only one height is changed while keeping the two-line distance as  $100 \mu\text{m}$ . (c), (d) Reproduced from [112]. © IOP Publishing Ltd. All rights reserved.

When  $h_j$  approaches  $h$ , the two transmission dips avoid crossing each other, and the first dip and the peak get closer to each other with significantly increasing quality factors, about three orders of magnitude higher. In the vicinity of  $h_j = h$ , the quality factor of the Fano resonance tends to be infinity, rendering a ‘trapped mode.’

Then, we consider two lines of pillars to study the interaction of two metasurfaces. When the distance between the two identical lines is  $230 \mu\text{m}$ , Fabry–Pérot resonance appears with a frequency equal to that of the pillars, as the wavelength in the plate is double the distance. The transmission of these three resonators is displayed as a blue solid line in figure 28(c), showing only one dip that reveals the role of Fabry–Pérot resonance as a bound state in the continuum. If we asymmetrically adjust the heights of two pillars, the Fabry–Pérot resonance becomes visible and results in a sharp transmission peak from the original dip, as shown in other solid lines in figure 28(c). The frequencies of the two dips follow the resonant frequencies of the two pillars and the peak is induced by Fano interference from Fabry–Pérot resonance, being an acoustic analog of EIT. When the distance between the two identical lines is  $100 \mu\text{m}$ , the Fabry–Pérot resonance is outside the studied frequency domain, so no Fano interference is

involved. When the two pillars are identical,  $h_1 = h_2 = 245 \mu\text{m}$ , two transmission dips (black solid line in figure 28(d)) are observed with frequencies different from the individual resonant frequencies (red or blue circle-dotted lines). This is a splitting effect by strong coupling between the two resonant pillars, resulting in an acoustic analog of ATS. If  $h_2$  deviates from  $245 \mu\text{m}$ , the coupling effect between the two pillars weakens and finally disappears. As is seen, the two dips exactly meet the individual resonances for  $h_2 = 220 \mu\text{m}$  or  $h_2 = 270 \mu\text{m}$  in figure 28(d), not as ATS anymore.

The transparent windows in the transmission curves for EIT and ATS are usually similar and difficult to discern. Many efforts have been made to realize differences between them using proposed numerical methods in classical systems such as optomechanics, microresonators, photonic crystals, and plasmonics, among others. In our studies, we proposed a fundamental discerning method by utilizing their physical mechanisms. The principle of the method is also extended to an acoustic system with Helmholtz resonators grafted to a tube which is supported by analytical, numerical, and experimental validations as well as the common Akaike information criterion method [180].

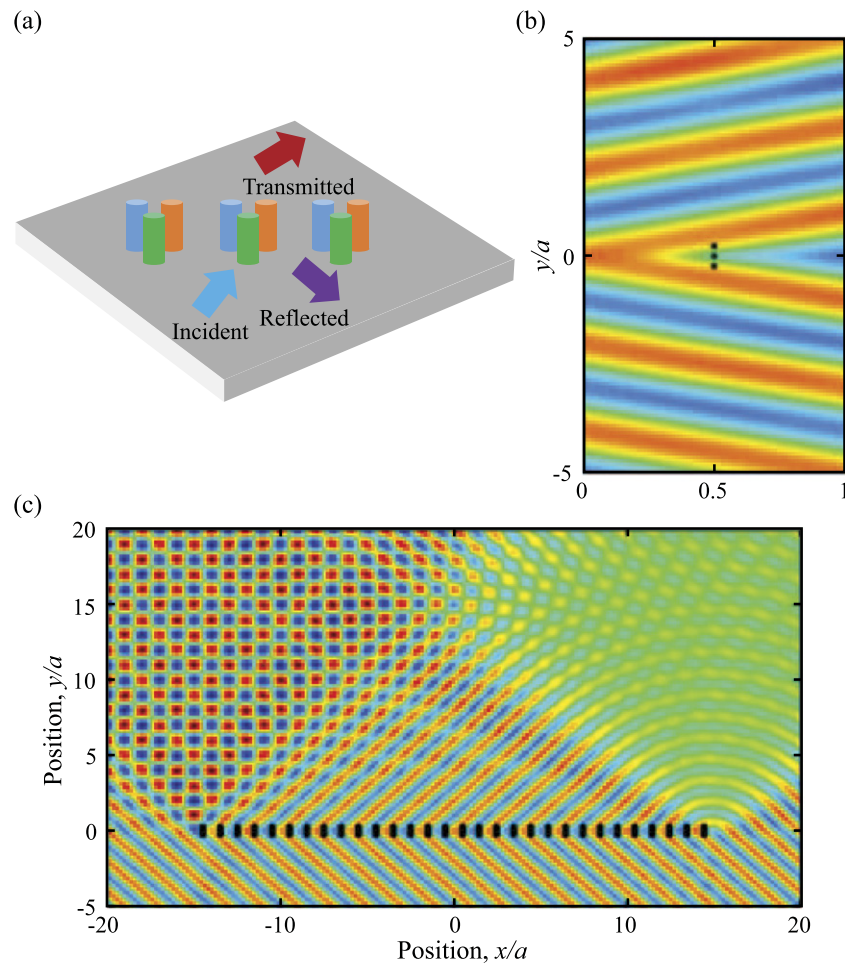


**Figure 29.** Pillared metagrating. (a) Each unit of the grating consists of three pillars. For an incident flexural wave, the grating reflects and refracts with different diffraction modes. (b) Full wave distribution of the grating unit with an incident angle and only the  $n = -1$  refracted diffraction mode. (c) Full wave field function as in (b) but for a finite number of 30 units. The blue and red colors stand for  $-max$  and  $max$  values, respectively. Reprinted figure with permission from [260], Copyright (2019) by the American Physical Society.

**4.2.3. Metagrating by diffraction engineering.** A metasurface requires a gradient profile (e.g. phase response) along the surface to achieve wavefront functions. Another way is to design a grating that can channel a wave at a desired diffraction order while eliminating other orders. The idea was first realized by Torrent [259] with inverse design for an acoustic wave and applied to an acoustic carpet cloak by Jin *et al* [178]. Afterward, it was extended to a flexural wave in a thin plate with a pillar-like resonator [260].

Despite the complex vibrations of an actual pillar configuration, it can be simplified as a mass resonator connected to a plate with a spring. Implementing the Kirchhoff plate equation with Newton's second law and Hooke's law, the equation of motion can be solved for the multiple scattering problem with a given incident wave for periodically arranged pillar scatterers. In other words, if the positions and physical parameters are known, the reflective and refractive properties can be consequently acquired. For the wave function considered,

reflection and transmission coefficients can be first controlled through the grating design, and the physical properties of pillar scatterers may then be inversely derived.

In figure 29(a), a cluster is shown that consists of three different scatterers with a given position pattern that is periodically arranged as a line on a thin plate. For a given frequency and incident angle, the object of the wave function is to keep the  $n = -1$  refractive diffraction order while eliminating all other diffraction orders. In order to obtain a unique solution, the position pattern of the cluster is linear as shown in figure 29(b). The impedance of the scatterers can be finally solved. The field of the diffraction of a plane wave by infinite grating is computed and displayed in figure 29(b), showing the exact  $n = -1$  refractive diffraction effect. In figure 29(c), the full wave distribution for a finite grating of 30 clusters is presented with the same diffraction effect. It should be noted that clusters of different diffraction effects can also be composed in a grating to design focusing lenses, cloaks, etc.

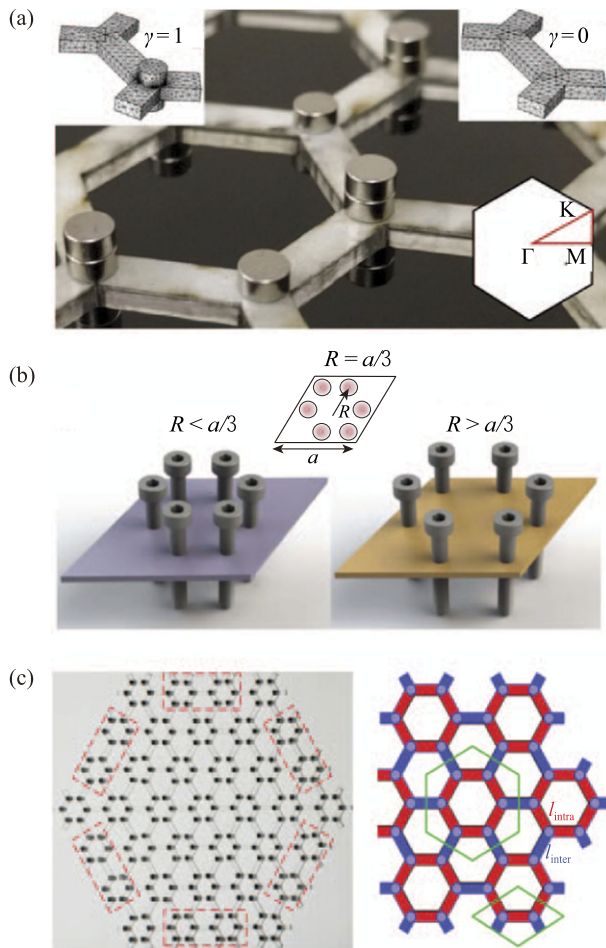


**Figure 30.** (a) Structure exhibiting the acoustic analog of the quantum valley Hall effect for flexural waves by breaking inversion symmetry in the unit cell. Reprinted figure with permission from [166], Copyright (2019) by the American Physical Society. (b) Structure exhibiting the acoustic analog of the pseudospin Hall effect for flexural waves by shrinking the six-resonator unit size. Reproduced from [275]. CC BY 4.0. (c) Elastic higher-order topological insulator with topologically protected corner states by a shrunk unit cell with six resonators. Reprinted figure with permission from [170], Copyright (2019) by the American Physical Society.

## 5. Topological pillared phononic plate

### 5.1. Introduction

Mechanical analogs of topologically protected edge states have been widely studied, including analogs with the quantum Hall, quantum spin Hall, and quantum valley Hall effects for which pioneering bodies of work in condensed matter physics were awarded the Nobel Prize<sup>10</sup>—in 1985 for ‘the discovery of the quantized Hall effect’ [261], in 1998 for ‘the discovery of a new form of quantum fluid with fractionally charged excitations’ [262, 263], and most recently in 2016 for ‘theoretical discoveries of topological phase transitions and topological phase of matter’ [264–266]. The reader is referred to reference [267] as one of the early treatments of topological

systems for elastic waves. Detailed information on the application of topological principles to acoustic/elastic systems is found in recent reviews [268–270] and a recent monograph [271].

Phononic crystal plates consisting of periodic pillars deposited on a thin plate are able to exhibit topologically protected edge states, a concept that originates from electronic systems. An analytical formulation was developed for a pillared phononic plate in terms of flexural waves, by considering the pillar as a point-like resonator connected to the plate by a spring for out-of-plane vibrations [272]. For a honeycomb lattice of such resonators, Torrent *et al* [162] used this analytical formulation and demonstrated Dirac cones due to the lattice symmetry as an elastic analog of graphene and found analytical expressions for both Dirac frequency and velocity. The Dirac cone is protected by inversion symmetry and time-reversal symmetry. By breaking either the inversion symmetry within the honeycomb unit cell or the time-reversal symmetry, the degeneracy at the Dirac point is lifted, giving rise to the opening of a gap. The upper and lower bands surrounding the gap have nonzero Chern number (topological invariant), which reveals a nontrivial property for the gap and allows the existence of topologically protected edge states at the interface between two topologically different crystals. Of note, topological Fano resonance can be generated by combining both topological bright and dark modes in a pillared beam [273, 274].

### 5.2. Topologically protected states

Based on an analytical model of pillar-like point resonators on a plate, Pal and Ruzzene [163] introduced topologically protected edge states by breaking inversion symmetry. This was further experimentally demonstrated with an actual pillar configuration [166], with the geometry shown in figure 30(a). The double-sided hexagon was shown to possess a Dirac cone at the  $K/K'$  point in the Brillouin zone when the masses of the pillars were identical. If the mirror symmetry of the unit cell is broken by introducing different masses (through changing the height of the pillars, for example), the Dirac cone degeneracy is lifted and a nontrivial band gap is formed with valley Chern number of an upper or lower band equal to  $1/2$  or  $-1/2$  at the  $K$  or  $K'$  points, which shows opposite polarizations of their eigenmodes; this illustrates an analogy with the quantum valley Hall effect. The symmetry-broken unit can be further taken to build a finite strip with an interface separating two lattices. The dispersion of the strip supports an interface band in the bulk nontrivial band gap, the eigenmodes of which are localized at the interface units, as a topologically protected edge state. Other investigations of pillared systems examining topologically protected edge modes are found in reference [166–168].

Chaunsali *et al* [164, 275] demonstrated the pseudospin Hall effect for flexural waves with local resonators as shown in figure 30(b). The arrangement of six bolt-like pillars in a hexagonal lattice has different sizes, shrunk or expanded. Since the bigger unit cell with six resonators is chosen instead of the unit cell with two resonators, it is possible for a

<sup>10</sup> Source: <http://nobelprize.org>

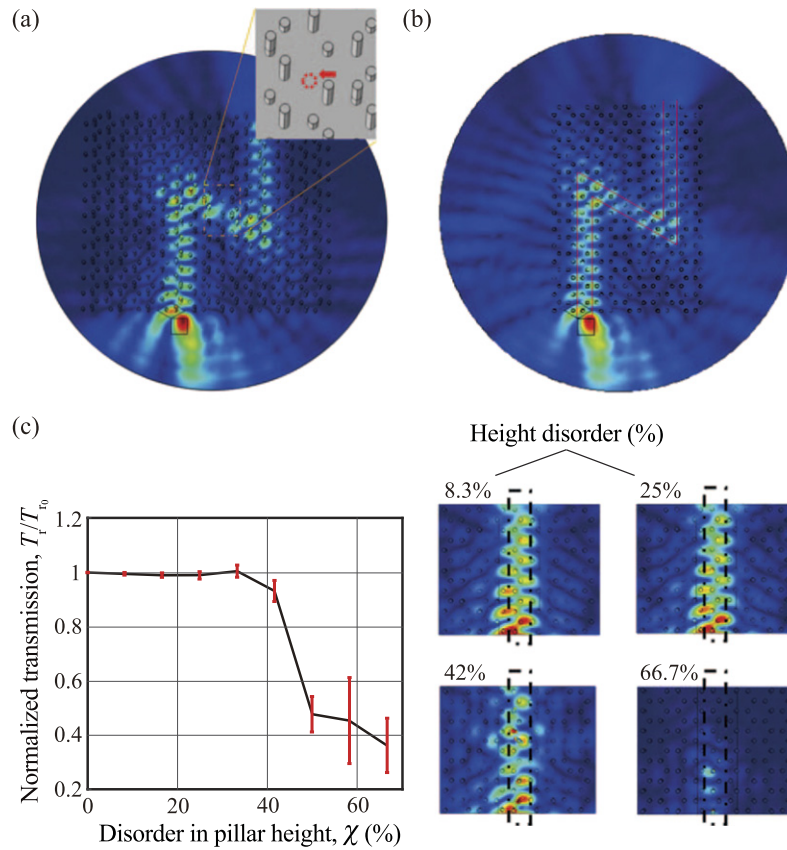


**Figure 31.** (a) Topologically protected zigzag interface state against a defect. (b) Same zigzag state against a minimized bulk size with only one hexagon unit beside the interface. (c) (Left) Transmission property versus height disorder level of the pillars of the interface. (Right) Flexural wave propagation field for four selected height disorders. The blue and red colors stand for 0 and max values, respectively. Reprinted figure with permission from [168], Copyright (2018) by the American Physical Society.

double Dirac cone at the  $\Gamma$  point to be constructed by adjusting the proper radius and zone-folding of bands. It should be noted that it is also possible for the double Dirac cone to occur at the  $K/K'$  point for a patterned plate with proper parameters [276, 277]. A Bragg band gap is formed from the degeneracy of the double Dirac cone when the six resonators expand due to the change in translational periodicity. However, a nontrivial band gap is formed when they shrink and the degenerated bands have a nonzero spin Chern number. Therefore, the emergence of topological edge modes appears at the interface that separates trivial and nontrivial lattices. This bolt–resonator configuration was recently used to construct Kekule-distorted mechanical graphene and a topologically bound state was demonstrated. A mechanical analog of Majorana bound states is also demonstrated by creating a Kekule distortion vortex on a bolt–resonator honeycomb superlattice [278]. Very recently, a double-sided pillared phononic plate drilled with patterned holes was shown to emulate the quantum spin Hall and quantum valley Hall effects with different Lamb modes [279, 280]. The quantitative robustness of topological states in twisted patterns was also studied [281].

Similar to the geometry in figure 30(a), the dispersion of a large unit cell containing six resonators (marked by the green hexagon in figure 30(c)) can exhibit a double Dirac cone at

the  $\Gamma$  point due to band folding. The lattice can be expanded or shrunk by tuning the red and blue connecting bars, which degenerates the double Dirac cone and forms a band gap. A hexagonal sample with shrunken unit cells as shown in figure 30(c) displays gapped edge modes, topological corner modes, and trivial corner modes in the degenerated band gap. When defects are applied to the red-dotted boxes, the trivial corner modes shift frequencies while the edge and topological corner modes are robust [170].

### 5.3. Robustness of topologically protected edge states

Topology is an effective tool to describe the properties of wavefunctions over a band and it may be utilized to produce waveguides that are robust against certain perturbations [269]. It is widely demonstrated that a topologically protected edge state is immune to the backscattering effect, thus enabling it to propagate through a sharp corner without backscattering. With respect to the existence of defects, the topologically protected edge state is robust to such local perturbation without any influence on wave transport. This is illustrated in figure 31(a) where a point defect is added along a zigzag topologically protected edge state.

If local perturbations are strong enough for the nontrivial band gap to be closed or the edge band to be disturbed, the

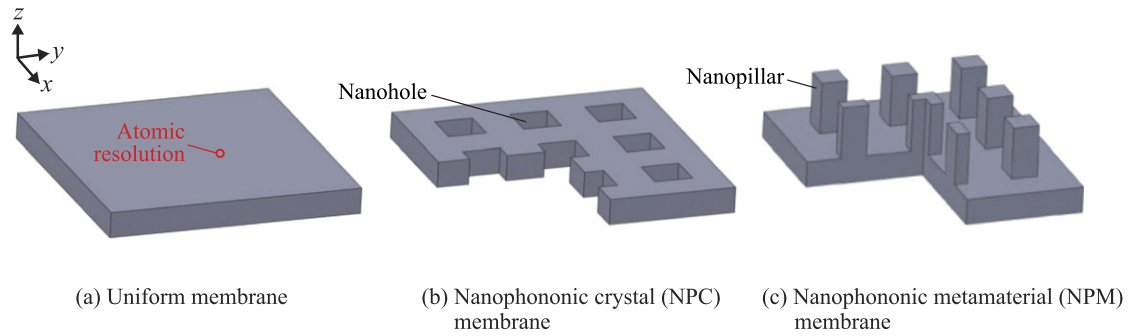


**Figure 32.** Three silicon membrane configurations: (a) uniform, (b) NPC, and (c) NPM.

robustness of the topologically protected edge states will consequently fail to preserve edge propagations. In figure 31(b), we minimize the size of the bulk structures surrounding the zigzag interface. When there is only one hexagon surrounding the interface, more leaky waves are observed, especially at the sharp corners. The wave amplitude decreases significantly after two sharp corners; meanwhile, the zigzag interface propagating is still preserved. It is further found that once the surrounding bulk media for the sharp corners continue to be minimized, the edge wave cannot even pass the first corner and the zigzag interface propagation disappears. It is suggested that two or more hexagons should be considered for the size of the bulk structures in order to preserve the nontrivial band gap [170].

In figure 31(c), we discuss the transmission along a linear edge when all the pillars along the interface are subject to height disorder. A disorder degree of  $x\%$  means that the heights of all the pillars at the interface can randomly be increased or decreased within a range of  $x\%$ . From the left panel of figure 31(c), it is noticed that the transmission through the topologically protected interface state is not affected for a wide range of height disorder and the transmission remains close to unity up to a disorder degree of about 40%. However, an abrupt drop occurs in transmission when the height disorder increases from 40% to 50%, and then the transmission oscillates around 0.4 for a higher degree of disorder. The sudden drop behaves like a transition threshold in the propagating states that can be seen from the wave fields in the right panel of figure 31(c). The transmission is close to unity for values of height disorder of 8.3% and 25%. For higher disorders of 42% and 66%, it is seen that the incident wave hardly enters the interface as the interface mode disappears. As such, the low transmission value is from the wave-reflecting effect at the entrance [170].

## 6. Nanophononic metamaterials: nanopillared membranes for thermal conductivity reduction

### 6.1. Introduction

The previous sections provide a thorough review of pillared phononic crystals, metamaterials, and metasurfaces at the ‘macroscale’ where the phenomena of interest pertain either to acoustic or elastic waves. The length scales relevant to this class of problems are typically of the order of micrometers and

larger, reaching meters, and the frequencies range from hertz to megahertz and possibly gigahertz. The most common and effective modeling framework of macrophononics lies within the continuum hypothesis.

In this section, we transition to a fundamentally different class of problems where we enter into the domain of *nanophononics*. Here, the interest is primarily in heat transfer by conduction; the length scales are in the nanometer range, and the relevant frequencies are in terahertz—often spanning tens of terahertz. Because of the very high frequencies and the size dependence of the underlying physics (among other factors), the modeling paradigm for nanoscale thermal transport is necessarily atomistic. This regime has been investigated within the nanoscale heat transfer community for the past few decades, primarily focusing on low-dimensional materials [282–287] until recently, when a merge with concepts and themes from phononic crystals and metamaterials began taking shape, attracting a growth in cross-disciplinary research.

**6.1.1. Nanophononic crystals.** The notion of a phononic crystal at the nanoscale, i.e. nanophononic crystal (NPC), was first explored in the context of 1D layered crystals [288, 289] and shortly afterward was advanced to two [290–295] and three dimensions [296–298]; see, for example, the figure 32(a) and (b) schematics of a uniform membrane and a membrane in the form of a NPC, respectively. While the interest in macroscopic phononic crystals is usually dominated by the presence of band gaps, at the nanoscale (when a 3D crystal is modeled atomistically) a complete band gap is unlikely to emerge [297]. The interest, instead, is primarily in the flattening of the dispersion curves that arise due to Bragg scattering. Flatter dispersion curves have lower group velocities and this, in turn, leads to a reduction in the lattice thermal conductivity. This mapping between the group velocities and the total lattice thermal conductivity (i.e. not considering thermal transport by electrons) is best understood by examining the integrand in the Boltzmann transport equation following the single-mode-relaxation time approximation [299, 300]; for a membrane-like material, this equation is

$$k_T = \frac{1}{V} \frac{A_c}{4\pi} \sum_m \int_{\kappa} C(\kappa, m) v_g^2(\kappa, m) \tau(\kappa, m) \kappa d\kappa, \quad (6.1)$$

where  $k_T$  is the in-plane lattice thermal conductivity,  $A_c$  is the unit cell base,  $V$  is the total volume of the system,  $C$  is the specific heat, and  $v_g$  and  $\tau$  denote the group velocity and the scattering time constant (lifetime), respectively. The integration is over all phonon wavenumbers for branch number  $m$  and the summation is over all the phonon branches. The division by  $V$  stems from the fact that  $k_T$  is an intrinsic volumetric property [190]. From equation (6.1), it is seen that a prediction of  $k_T$  is constructed by summing over all phonon modes in the spectrum and integrating along the direction of interest over the Brillouin zone. The thermal conductivity is therefore dependent on the phonon band structure, which in turn is affected by the unit cell structure and lattice symmetry. The integrand consists of a product of the specific heat, the group velocity squared, and the lifetime—all quantities defined for each mode of phonon motion as determined by the dispersion spectrum. An NPC membrane consisting of a host semiconducting material, silicon for example, and a periodic array of nanoscale holes or inclusions may exhibit a lower in-plane thermal conductivity compared to a corresponding uniform membrane due to substantial flattenings in the dispersion curves. A practical disadvantage, however, is that the surfaces of the periodic features, e.g. the holes or inclusions, must be very smooth to preserve the phase information required for the Bragg effects to take place—especially when the features are of relatively large sizes compared to the phonon wavelengths [294, 301, 302]. At a more fundamental level, the degree and intensity of group-velocity reductions are limited to what the available Bragg interference patterns can provide, which is somewhat modest, leading usually to an order of magnitude reduction at most [294]. One possibility is to allow the boundaries or interfaces of the holes or inclusions to be rough, which would induce mostly boundary scattering, possibly in combination with some level of Bragg scattering. In this scenario, one may increase the size and concentration of the holes or inclusions to the point where the phonon motion is inhibited excessively by the scattering component. Here, the effective thermal conductivity in the overall medium may be reduced significantly, however at the expense of having extremely small/thin segments of the host material, e.g. in reference [298]. This approach would therefore not be favorable if the interest is to reduce the thermal conductivity without negatively impacting the electrical conductivity—as needed in thermoelectrics [303–305].

**6.1.2. Nanophononic metamaterials.** The notion of a metamaterial for the reduction of the thermal conductivity by local resonances has been introduced by Hussein and co-workers, first in 2014 [186, 187] followed by a series of systematic investigations [188–191, 306]. The underlying concept in this new class of metamaterials, termed NPM, is to intrinsically introduce nanoresonating substructures to a host crystalline material, typically a semiconductor, such that a very large number of local resonances emerge and contribute through several mechanisms to the reduction of the overall lattice thermal conductivity. The local resonances couple with heat-carrying phonon modes of the host medium. This atomic-scale coupling phenomenon gives rise to a resonance hybridization between pairs of the wavenumber-independent vibration

modes of the local substructure (vibrons) and wavenumber-dependent wave modes of the host medium (phonons)<sup>11</sup>. Vibron–phonon couplings create dispersion curve flattenings and, consequently, reductions in the group velocities and hence the overall thermal conductivity. Stronger couplings produce sharper curve flattenings and larger reductions in the group velocities. The local resonances also confine the atomic modal motion within the nanoresonators, which in turn causes further reduction in the thermal conductivity. In addition, the phonon lifetimes drop due to changes in the scattering environment, including both phonon–phonon scattering and boundary scattering, as long as these two processes are kept in moderation to keep the phonon MFP relatively high for the aforementioned wave effects to take place. The power of this approach stems from the fact that the local resonances may be tuned by design to be numerous and span the entire phonon spectrum of the host material, and, moreover, conform in their DOS distribution to the host material phonon DOS (see sections 6.2.1 and 6.4), thus maximizing the intensity of the wave-based mechanism mentioned above and increasing the thermal conductivity reduction. In the limit, the number of local resonances is three times the number of atoms in a unit nanoresonator.

It is worth noting the fundamental contrast with conventional metamaterials where the aim is to generate subwavelength band gaps or create negative long-wave effective properties, as is the case for locally resonant electromagnetic [20, 21], acoustic [19], and elastic [26, 27, 307] metamaterials (sections 2–5 focus on conventional metamaterials). The target in NPM design is to optimally enable the thermal conductivity reduction mechanisms: group velocity reduction, energy localization, and lifetime reduction. Another practical goal is to do so without affecting the electrical properties in order to effectively increase the thermoelectric energy conversion figure of merit  $ZT$  [190, 191].

The NPM configuration proposed in references [186–191] consists of an array of silicon nanopillars distributed on the surface(s) of a freestanding silicon membrane with no interior scatterers; see illustration in figure 32(c). Here, the nanopillars act as the resonating substructures. Since the nanopillars are located outside the main body of the membrane, which serves as the transport zone, the electronic band structure is only mildly affected and electron scattering occurs only near the membrane surfaces and not in the interior. Compared to all common phonon-scattering-based approaches (where the scatterers are in the main body of the transport medium), this NPM configuration therefore provides the unique advantage of practically decoupling the lattice thermal conductivity from the Seebeck coefficient and the electrical conductivity—which is essential to creating significant increases in  $ZT$ . In addition, an NPM in the form of a nanopillared membrane naturally exhibits dimensionality reduction (compared to the bulk form). Therefore, the powerful rewards of resonance-induced thermal

<sup>11</sup> The term ‘phonon’ may generally be used to denote either propagating or localized modes; here we refer to the standing vibration modes associated with a nanoresonator specifically as ‘vibrons.’

conductivity reduction are gained over and above the benefits of phonon confinement [308] and surface roughness in the membrane portion [309] (as well as the benefits to the electrical properties [310]). Equation (6.1) applies to an NPM as it does for an NPC, keeping in consideration that for a nanopillared NPM the volume  $V$  includes both the base membrane and nanopillar portions<sup>12</sup>.

Since the publication of reference [186] in 2014, several investigations of NPMs by other groups have followed. Several papers have computationally examined a variety of NPM configurations for thermal conductivity reduction. Using atomic-level modeling, Wei *et al* explored the effects of varying the nanopillar spacing and dimensions in silicon nanopillared membranes and analyzed mode localization [311]. Xiong *et al* studied silicon NPMs in the form of rods/wires with branching structures and explored the effects of alloying and temperature [312]. More recent investigations of rod/wire-based NPMs were conducted by Ma *et al* considering orthogonal ‘cross junctions’ as nanoresonators [313] and by Zhang *et al* considering spiral extrusions as nanoresonators [314]; Ma *et al* studied local resonant effects in 3D silicon nanowire cages [315]; and Zhu *et al* [316] considered bulk silicon with internal amorphous regions acting as the nanoresonators (see reference [317] for a survey of potential configurations using atomically disordered inclusions). Thermal conductivity reduction in branched nanoribbon materials composed of molybdenum disulfide ( $\text{MoS}_2$ ) was reported by Liu *et al* [318]. Giri and Hopkins [319] and Yang and co-workers [320] extended the NPM theme to carbon nanotubes and graphene sheets, respectively. Another intriguing NPM architecture is based on a graphene sheet decorated with branching fullerene nanoresonators [321]. The impact of nanopillars on the heat capacity was investigated by Iskandar *et al* using both theory and experiments [322]. The NPM concept has also been employed for thermal rectification, in indium arsenide nanowires [323, 324], nanopillared graphene structures [325], and graphene nanoribbons [326]. A range of possible NPM geometric configurations, including 1D, 2D, and 3D systems, is given in reference [187], noting that one of the unique features of NPMs is that they may be realized using a wide range of materials for both the host medium and the nanoresonator medium. Other studies examined NPMs using finite-element analysis as often done for macroscale acoustic or elastic metamaterials [124, 192, 327–329]. While linear continuous modeling may provide some insights, atomistic modeling is necessary for accurate qualitative and quantitative capturing of the effects of the three key NPM mechanisms responsible for thermal conductivity reduction. This can be seen in the inherent dependence of the thermal conductivity on (1) the number, range, and detailed characteristics of the dispersion branches in the phonon band structure, as evidenced in equation (6.1) and the intricate band structures of figures 34(b) and 35 (noting that these figures

<sup>12</sup> An alternative membrane-based NPM configuration involves replacing the nanopillars with nanowalls to serve as the nanoresonators [187, 190, 373]. A nanowall features a larger value of  $V$  compared to a nanopillar which implies a larger number of vibrons and hence stronger thermal conductivity reduction, as well as an opportunity to realize an anisotropic thermal conductivity tensor.

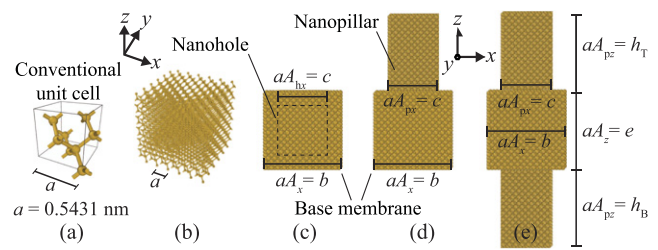


**Figure 33.** (a) Conventional eight-atom unit cell for silicon and unit cells for a (b) uniform membrane, (c) NPC with cubic nanohole, (d) single-pillared NPM, and (e) double-pillared NPM. In (b)–(d), the unit cell is repeated in the  $x$  and  $y$  directions, and the top and bottom surfaces are free. Heat conduction takes place in the in-plane directions along a uniform membrane and, correspondingly, along the membrane portion of an NPM. Reprinted figure with permission from [190], Copyright (2018) by the American Physical Society.

only show a small portion of the spectrum), and (2) the anharmonic interatomic interactions. A study of the convergence of the FE-based thermal conductivity reduction predictions to those obtained by atomic modeling is given in the supplementary material accompanying reference [186]. The importance of atomic resolution and nonlinear effects is further reinforced by observation of the profound size and geometry dependence of the underlying physics of nanoscale thermal transport in NPMs [190].

**6.1.3. NPMs versus NPCs.** Compared to NPCs, NPMs are not dependent on periodicity and phased traveling wave interferences, and are therefore more robust to disorder in the arrangement of the nanoresonators and to surface roughness. Furthermore, the intensity of group-velocity reductions, mode localizations, and controlled lifetime reductions may be continuously enhanced by simply increasing the size and packing efficiency of the nanoresonators [189, 311]. Future research may consider a hybrid between an NPC with nanoholes and an NPM with nanopillars, that is, a nanoscale version of the trampoline configuration of section 3.1.1. In this way, additional Bragg scattering from the nanoholes and relatively lower resonance frequencies from the ‘more compliant’ nanopillars may be realized. As long as there is enough spacing between the nanoholes not to impede the electron transport, it is conceivable that this mixed nanohole–nanopillar configuration would harness better-performing thermoelectric energy conversion compared to only nanopillars.

## 6.2. Lattice dynamics and vibron–phonon couplings

In an NPM, the substructure resonances—denoted as vibrons—are distinct from phonons by virtue of their wavenumber-independent standing-wave character. The frequency spectrum of vibrons may be designed to couple with heat-carrying wavenumber-dependent phonon modes belonging to all or most of the dispersion branches across the full spectrum of the host medium. As described in section 6.1, this atomic-scale coupling mechanism gives rise to a resonance hybridization between pairs of vibrons and phonons. This phenomenon may be demonstrated theoretically using LD calculations on a unit cell of the NPM.

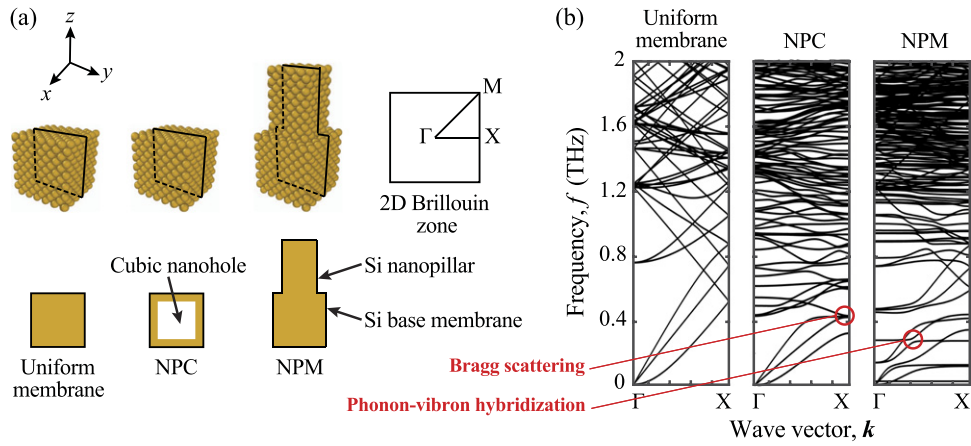


**Figure 34.** (a) Schematics and (b) phonon band structure for a uniform membrane, an NPC membrane, and an NPM membrane. For the NPC, the size of the unit cell is  $3.26 \text{ nm} \times 3.26 \text{ nm} \times 3.26 \text{ nm}$  and the size of the centrally located nanohole is  $2.17 \text{ nm} \times 2.17 \text{ nm} \times 2.17 \text{ nm}$ . For the NPM, the size of the base membrane is  $3.26 \text{ nm} \times 3.26 \text{ nm} \times 3.26 \text{ nm}$  and the size of the centrally located nanopillar is  $2.17 \text{ nm} \times 2.17 \text{ nm} \times 3.26 \text{ nm}$ . The dimensions of the uniform membrane unit cell are  $3.26 \text{ nm} \times 3.26 \text{ nm} \times 3.26 \text{ nm}$ .

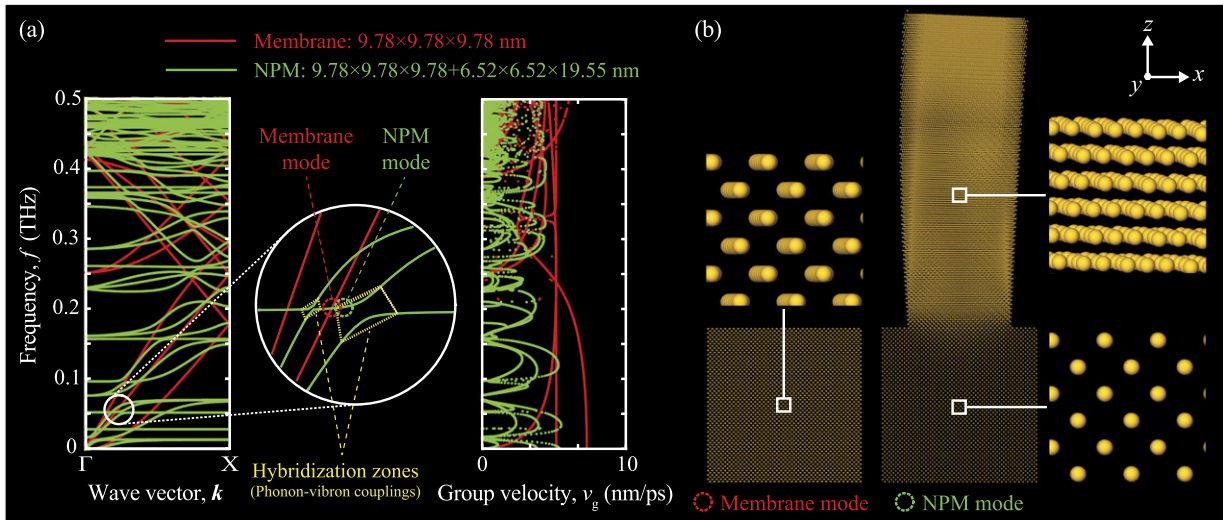
Here, we review the wave propagation characteristics of two freestanding NPM configurations: a membrane with nanopillars (i) on one surface (single-nanopillared) and (ii) on each of the surfaces (double-nanopillared). In all cases, both the base membrane and nanopillar(s) are made of defect-free single-crystal silicon. Figure 33 displays the unit cells of these two configurations as well as the structure of a conventional cell (CC) and a unit cell of a corresponding uniform (unpillared) membrane. The geometry of a membrane with nanopillars on each surface is represented as  $b \times b \times e + c \times c \times h_T + c \times c \times h_B \text{ nm}$  (which may be converted to CC by dividing each dimension by the atomic spacing  $a$ ). The last two terms represent the size of the top and bottom nanopillars, respectively, and these are dropped when representing an unpillared membrane. If only a single nanopillar is included in the unit cell, the nanopillar height is denoted simply by  $h$ . All geometric parameters are pictorially defined in figure 33. Unless explicitly specified, all the analyses presented in this section are at a room temperature of  $T = 300 \text{ K}$ , and the Stillinger–Weber empirical potential is used in all models to represent the interatomic interactions [330]. Additionally, to keep our focus on the core effects of local resonances, we only consider defect-free crystals.

Figure 34 shows a portion of the dispersion curves for an NPM in the form of a nanopillared membrane and, for comparison, the corresponding dispersion curves for an NPC in the form of a membrane with nanoholes. The NPC has the same membrane thickness as the NPM and the cross-sectional size of the nanoholes is chosen to be equal to that of the nanopillars. Moreover, for comparison, dispersion curves for a uniform membrane with the same thickness are shown. Compared to the uniform membrane, the NPC curves appear to be flatter, especially at the rhs edge of the Brillouin zone—this is a manifestation of Bragg scattering. In contrast to the NPC, the NPM features vibron local resonances, appearing as horizontal lines that veer off (i.e. create avoided crossings with) the underlying phonon dispersion curves of the membrane. Because the nanopillars are laid out periodically, curve flattenings at the

edge of the Brillouin zone due to Bragg scattering are also observed. The reader is referred to references [2–4, 6, 22, 24] for more discussion on the difference between a phononic crystal and a locally resonant metamaterial in general, regardless of scale.

Figure 35 provides a more in-depth demonstration of the resonance hybridization phenomenon, as manifested in the phonon band structure, group-velocity distributions, and associated mode shapes. For this purpose, we consider a  $9.78 \times 9.78 \times 9.78 + 6.52 \times 6.52 \times 19.55 \text{ nm}$  NPM unit cell (consisting of 88128 atoms). To economically obtain the phonon band structure for such a large unit cell, we used the reduced Bloch mode expansion technique [331] to solve the corresponding eigenvalue problem over the 0–0.5 THz range. The effects of the phonon–vibron mode coupling phenomenon are clearly displayed in both the dispersion diagram and the corresponding group velocity diagram, as shown in figure 35(a). The profound reduction in the group velocities is evident across the entire frequency range plotted (and the same effect extends throughout the entire spectrum). As noted earlier, a reduction in phonon group velocities directly implies a reduction in the thermal conductivity. Figure 35(b) focuses on a particular mode in the band structure and displays the unit cell mode shape without and with resonance hybridization. The confinement of the atomic motion solely in the nanopillar region represents a case of extreme localization of energy. This localization phenomenon in itself also contributes to the reduction in the thermal conductivity.

*Impact of mode localization on the thermal conductivity.* As noted earlier, while the nanopillar adds modes (vibrons) to the total unit cell system, most of these modes are severely localized (i.e. exhibiting zero group velocity in the band structure except near the phonon–vibron coupling regions). Therefore, even though these modes add to the number of terms summed in equation (6.1), the actual additional quantities that are summed are not significant. Given that the entire integration is finally divided by the total volume of the NPM material



**Figure 35.** Illustration of local resonances and the resonance hybridization phenomenon from an LD perspective. (a) Phonon band structure and group velocity distribution of a silicon membrane with (green) or without (red) silicon nanopillars erected on one surface. (b) Uniform membrane atomic displacements for a heat-carrying phonon mode in the acoustic regime contrasted with NPM atomic displacements of the same mode upon resonance hybridization. Significant motion within the uniform membrane is seen. In contrast, the atomic displacements of the NPM hybridized mode reveal localized nanopillar motion and almost no motion in the base membrane portion. In (a), a zoom-in is provided for two hybridization zones including the one illustrated in (b). A magnification factor of 2000 is applied to the atomic displacements in the mode-shape images. Reprinted figure with permission from [190], Copyright (2018) by the American Physical Society.

in the unit cell (since all atoms contribute to the coupled dispersion spectrum and the specific heat), the net effect on the thermal conductivity is that it decreases. This summarizes the cause of thermal conductivity reduction by atomic-scale mode localization.

**6.2.1. Conformity of phonon and vibron density of states.** As described earlier, the coupling between phonons and vibrons is the key enabling factor for the thermal conductivity reduction mechanisms in an NPM. The phonon motion is confined to the in-plane directions within the base membrane and the vibron motion is limited primarily to the domain of each nanopillar. At each phonon–vibron coupling, the phonon group velocities decrease, a pathway opens up for localization, and the phonon–phonon scattering increases. The more we have of these couplings across the full spectrum, the stronger the net reduction in the thermal conductivity. In figure 36, we examine how the overall size of the nanopillar affects the phonon and vibron DOS distributions, collectively (i.e. when considering the integrated nanopillared membrane unit cell), and separately (i.e. when considering isolated membrane and nanopillar components). For the collective DOS picture, one can observe a subtle change in the DOS distribution due to the addition of a nanopillar. A more refined picture is seen from the separate DOS distributions. A key factor is the degree of phonon DOS and vibron DOS conformity, which may be quantified. For this purpose, we have introduced a metric to represent the inverse of conformity, namely, the *nonconformity factor*  $\hat{R}_{pv}$  [190]. This factor is defined as

$$\hat{R}_{pv} = \|R_{pv} - R_{pp}\|, \quad (6.2)$$

where  $R_{pv}$  is the cross-correlation between the separate phonon and vibron DOS,  $R_{pp}$  is the autocorrelation of the phonon DOS, and  $\| \cdot \|$  denotes the double norm. The reader

may refer to Rabiner and Gold (1975) [332] for the definitions of correlation functions. The nonconformity factor varies between 0 (perfect conformity) and  $\infty$  (no conformity). We see in figure 36 that for the same base membrane size within the unit cell, the value of the nonconformity factor is significantly lower (i.e. the level of conformity is significantly higher) when the size (width and height) of the nanopillars is increased for a given base-membrane thickness. This characteristic of the phonon–vibron conformity provides an opportunity for an upscaling design pathway that creates *vibron compensation* (Honarvar and Hussein 2018) [190]. Vibron compensation is achieved by having the size of the nanopillar increased at a higher rate than that of the base membrane when an NPM is scaled up in size. The outcome is that not only (1) the phonon band structure is enriched with a higher vibrons-to-phonons ratio, but also (2) the level of conformity between the phonon and vibron DOS distributions across the full spectrum is significantly increased. Both these factors lead to increased reduction of the thermal conductivity upon upscaling.

**6.2.2. Size limitation of NPMs.** While the design process of upscaling with vibrons compensation yields improved NPM performance with size, there is a limit to the sizes that may be reached. Improvement in performance will be realized as long as the characteristic length scales of the individual components of an NPM, the base membrane and the nanopillars, are considerably within the span of the phonon MFP distribution at the temperature of interest. As the NPM feature sizes start approaching the far end of the MFP distribution, phonon–phonon scattering mechanisms will dominate and the impact of the resonance-induced mechanisms that reduce the thermal conductivity will gradually diminish. This underscores the design necessity of preserving the NPM system within the realm of the nanoscale.

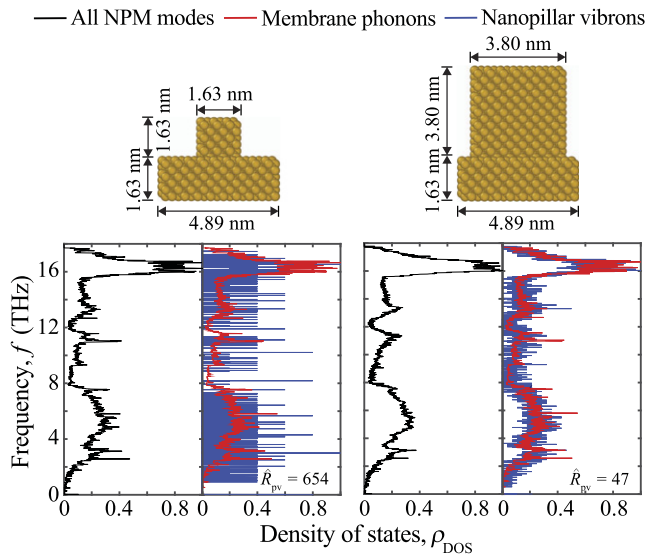


**Figure 36.** (a) Relative DOS distributions of all modes (black), phonons in the base membrane (red), and vibrons in the nanopillars (blue) for an NPM configuration with a small nanopillar, i.e. small  $V_r$  (left), and a large nanopillar, i.e. large  $V_r$  (right). The DOS quantity is denoted  $\rho_{\text{DOS}}$ . The quantity  $V_r$  represents the ratio of the volume of the nanopillar to the volume of the base membrane. The vibron DOS distribution is obtained by considering the nanopillar as an independent nanostructure with free boundary conditions. All quantities are normalized with respect to their maximum values. A large nanopillar with a large packing concentration leads to lower phonon–vibron conformity, which corresponds to lower values of  $R_{\text{pv}}$  and a more intense resonance hybridization effect. Reprinted figure with permission from [190], Copyright (2018) by the American Physical Society.

### 6.3. Molecular dynamics and spectral energy density analysis: evidence of localized resonances and resonance hybridizations

The NPM phonon band structures shown in figures 34(b) and 35 display the occurrence of local resonances, which feature as horizontal lines, and also the resonance hybridization phenomenon, which manifests as avoided crossings between these horizontal lines and the original dispersion curves of the base membrane. These phonon band structure diagrams, however, are obtained by solving an eigenvalue problem for the quasiharmonic (i.e. linear) version of the problem. In reality, the atomic interactions are anharmonic (i.e. nonlinear) at finite temperatures. The anharmonicities give rise to phonon–phonon scattering, which is noncoherent. Furthermore, the top and bottom surfaces of the unit cell are not necessarily ideal surfaces, which implies the possibility of boundary scattering at the surfaces, including the surfaces of the nanopillars. This too is a noncoherent effect.

In order to examine whether the vibrons and the resonance-hybridization mechanism do indeed exist and unfold in the presence of these nonlinearities (and other scattering mechanisms), we resort to equilibrium MD simulations and seek to obtain the dispersion behavior (if it exists) straight from the simulations. This is done by computing the spectral energy density (SED) [333–337], which is a quantity effectively representing the space–time Fourier transform of the simulated nonlinear response. There are two SED formulations reported

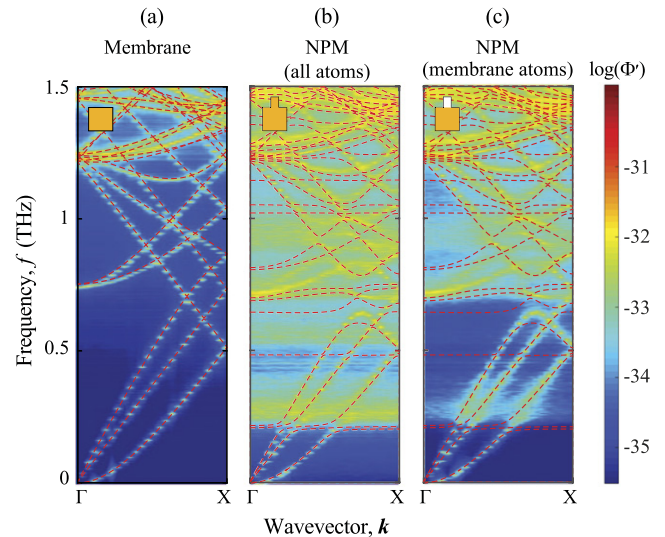


**Figure 37.** Phonon dispersion of an NPM and a corresponding uniform membrane with the same thickness. (a) and (b) show the SED spectrum for the uniform membrane and NPM, respectively. The SED spectrum of the NPM considering only the membrane atoms is displayed in (c). Dispersion curves obtained by quasiharmonic LD calculations are overlaid in dashed red lines. The NPM unit cell dimensions are  $3.26 \times 3.26 \times 3.26 + 1.09 \times 1.09 \times 1.63$  nm; the uniform membrane unit cell dimensions are  $3.26$  nm  $\times$   $3.26$  nm  $\times$   $3.26$  nm. Each inset presents a schematic of the unit cell analyzed, with the orange color representing the portion accounted for in the SED calculation. Reprinted figure with permission from [188], Copyright (2016) by the American Physical Society.

in the literature for phonon transport problems. In one SED formulation, referred to as  $\Phi$ , the MD atom velocities are projected onto the phonon normal modes of the constituent unit cell, which are obtained separately from quasiharmonic LD calculations. In an alternative formulation, referred to as  $\Phi'$ , the SED expression requires knowledge of only the crystal unit cell structure and does not require any *a priori* knowledge of the phonon mode eigenvectors. Both the  $\Phi$  and  $\Phi'$  formulations allow for an accurate prediction of both phonon frequencies and lifetimes [337]. In reference [188], we intentionally seek the  $\Phi'$  version of the technique since it enables us to establish whether or not wave behavior (including local resonances and resonance hybridization) is present in the simulations without any enforcement of wave characteristics in the calculations.

As provided in [333], the SED expression for  $\Phi'$  is a function of wave vector  $\mathbf{k}$  and frequency  $\omega$ , and is given by

$$\Phi'(\mathbf{k}, \omega) = \frac{1}{4\pi\tau_0} \sum_{\alpha}^3 \sum_s^n \frac{m_s}{N} \left| \sum_l^N e^{i\mathbf{k}\cdot\mathbf{r}_0(l)} \int_0^{\tau_0} \dot{u}_{\alpha} \left( \begin{matrix} l \\ s \end{matrix}; t \right) e^{-i\omega t} dt \right|^2, \quad (6.3)$$

where  $m_s$  is the atomic mass (which is the mass of a silicon atom for the cases considered in this section),  $\tau_0$  is the total simulation time,  $\mathbf{r}_0$  is the equilibrium position vector of the  $l$ th unit cell, and  $\dot{u}_{\alpha}$  is the  $\alpha$  component of the velocity of the  $s$ th atom in the  $l$ th unit cell at time  $t$ . There is a total of

$N = N_x \times N_y \times N_z$  unit cells in the simulated computational domain with  $n$  atoms per unit cell. We note that in equation (6.3), the phonon frequencies can only be obtained at the set of allowed wave vectors as dictated by the crystal structure. For our model, the  $\Gamma$ X-path wave vectors are  $k_x = 2\pi j/(N_x A_x)$ ,  $j = 0$  to  $N_x/2$ . We consider a single-nanopillared unit cell of dimensions  $3.26 \times 3.26 \times 3.26 + 1.09 \times 1.09 \times 3.26$  nm, i.e.  $b = 3.26$  nm,  $c = 1.09$ ,  $e = 3.26$  nm, and  $h = 3.26$  nm. For the computational domain, we set  $N_x = 50$  and  $N_y = N_z = 1$ , which gives a  $\Gamma$ X wave-vector resolution of  $\Delta k_x = 0.04$ . Room temperature MD simulations under NVE (constant mass, volume, and energy) ensembles were executed for this system for  $2^{22}$  time steps and based on a time-step increment  $\Delta t = 0.5$  fs. Equation (6.3) is evaluated by computing the SED field corresponding to the velocity trajectories extracted every  $2^5$  steps. The results from these calculations are shown in figure 37. As a reference, the phonon band structure as obtained from standard quasiharmonic LD calculations is shown in dashed red lines in figure 37(a) for a uniform membrane with the same  $t$  and in figures 37(b) and (c) for the NPM. The full SED spectrum is shown in figure 37(a) for the uniform membrane and in figure 37(b) for the NPM. Only the frequency range  $0 \leq \omega \leq 1.5$  THz is shown because higher frequencies are relatively difficult to distinguish in the SED field. This frequency range is responsible for a significant portion of the total lattice thermal conductivity [186]. We observe that the phonon dispersion emerging from the MD simulations matches very well with that obtained by the independent LD calculations, thus providing direct evidence for the existence of vibrons and phonon–vibron coupling. In particular, the first two nanopillar local resonances (present at nearly 0.2 THz) are clearly observed in the NPM SED spectrum, appearing as horizontal lines. Moreover, the interaction of these resonances with the acoustic branches of the underlying membrane are distinctly observed and closely follow the hybridization profiles featured in the LD dispersion curves. Resonance hybridizations are also clearly observed at higher frequencies in the figure where local resonance modes interact with optical dispersion branches.

Given our interest in the effects of the nanopillar resonances on the heat-carrying phonons within the base membrane, we also calculated the SED spectrum for the NPM considering only the contributions of the atoms housed in the base membrane (i.e. discounting the SED contributions of the nanopillar atoms). The outcome of this calculation is shown in figure 37(c), where we see clearly that the nanopillar resonances alter the fundamental nature of the phonon traveling waves within the membrane. These alterations in the phonon band structure result in a significant reduction in the phonon group velocities at each location in the band structure where an interaction takes place, and in mode localization around and away from the coupling regions. Both these effects contribute significantly to a reduction in the in-plane lattice thermal conductivity as analyzed in the next subsection. While phonon–phonon and phonon–boundary scatterings are still important mechanisms in the membrane-based systems

we have considered, the results are consistent with the understanding that the MFP distribution for silicon at room temperature comfortably spans, at a minimum, the length scale of the membrane thickness [338]. Such an MFP distribution is sufficiently broad to allow at least a portion of the nanopillar standing waves to impact the phonons traveling in-plane across the entire cross section of the membrane.

#### 6.4. Thermal conductivity predictions: size effects and the vibron compensatory effect

In this section, we review some recent predictions we obtained for the reduction in the thermal conductivity of NPMs at room temperature, and consider (1) the effect of the size of the nanopillar (for example, by varying its height) while keeping the base membrane thickness and the nanopillar lattice spacing constant, and (2) the effect of the membrane thickness while keeping the nanopillar-height-to-membrane-thickness aspect ratio constant. For this purpose, we used equilibrium MD simulations followed by post-processing of the results using the Green–Kubo (GK) [339–341] method. In the GK method, the lattice thermal conductivity tensor is calculated from the heat current autocorrelation function (HCACF) by

$$\mathbf{k}_T = \frac{1}{k_B V T^2} \int \langle \mathbf{J}(0) \otimes \mathbf{J}(t) \rangle dt, \quad (6.4)$$

where  $k_B$  is the Boltzmann constant,  $V$  is the total volume of the system including both base membrane and nanopillar portions (as defined earlier),  $\mathbf{J}$  is the heat current vector (in units of energy times length per unit time) computed over all atoms in the system, and  $\otimes$  denotes the tensor product operation. Following common notation,  $T$  is the temperature and  $t$  is the time. The integrand represents the time average of the HCACF. The evaluation of the heat current vector is done using the stress-based formula

$$\mathbf{J} = - \sum \mathbf{S}_i \mathbf{v}_i, \quad (6.5)$$

where  $\mathbf{S}_i$  and  $\mathbf{v}_i$ , respectively, denote the virial stress tensor and the velocity vector for atom  $i$ .

The equilibrium MD simulations were conducted on a set of NPM models and corresponding uniform membrane models (similar to the configurations shown in figure 33). The computational domain for the NPM and uniform membrane models consists in each case of one unit cell with standard periodic boundary conditions applied at the in-plane boundaries and free boundary conditions applied at the top and bottom surfaces in the  $z$ -direction [188–190]. The results we present are for systems that were initially equilibrated for 1 ns, with a time step  $\Delta t = 0.8$  fs, under the NPT ensemble (zero-pressure cell size based on constant number of atoms, pressure, and temperature). The simulations were subsequently allowed to run under the NVE ensemble for an additional 6 ns to collect heat fluxes that were recorded every 4 fs. The 6 ns time span is sufficiently long compared to the longest phonon lifetime to reliably predict the thermal conductivity. With these parameters, the HCACFs generally converged within the first 1 ns, with the rate of convergence depending on the type of material system (e.g. uniform membrane or NPM). The smaller the value

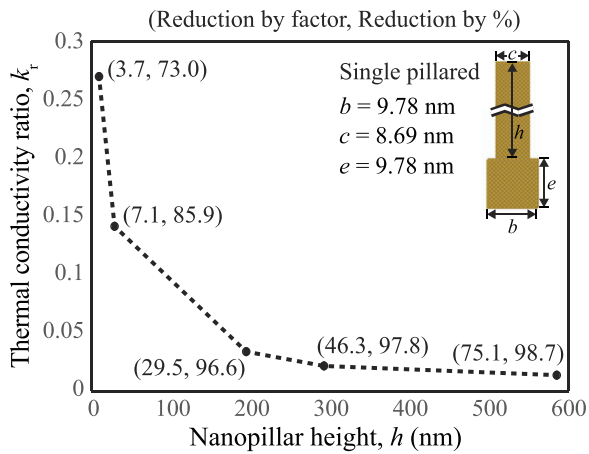


**Figure 38.** Thermal conductivity ratio  $k_r$  versus nanopillar height for a membrane with a thickness of 9.78 nm. Numbers in parentheses indicate the thermal conductivity reduction due to addition of the nanopillar, given as a multiplication factor (first number) and as a percentage (second number). Due to the elevated  $V_r$  values, the curve demonstrates very strong dependence of the thermal conductivity reduction on the nanopillar height. Reprinted figure with permission from [190], Copyright (2018) by the American Physical Society.

of the predicted thermal conductivity, the shorter the convergence time. LAMMPS software [342] was used for the implementation of the simulations. To minimize modeling error, we focused our attention on the reduction of the thermal conductivity when a nanopillar (or more) is added to an otherwise uniform membrane. This reduction is expressed as the ratio  $k_r = k_{\text{NPM}}/k_{\text{uniform}}$ , where  $k_{\text{NPM}}$  and  $k_{\text{uniform}}$  denote the in-plane lattice thermal conductivity of the NPM and corresponding uniform membrane, respectively.

First, we examined an NPM unit cell with the following dimensions: 9.78 nm  $\times$  9.78 nm  $\times$  9.78 nm for the base membrane and 8.69 nm  $\times$  8.69 nm  $\times$  9.78 nm for a single nanopillar. The predicted  $k_r$  for this configuration is 0.27; this corresponds to a reduction in thermal conductivity by 73% (a factor of 3.7) compared to a uniform membrane with the same thickness. A valid question concerning this result is whether the nanopillars cause this reduction primarily due to the introduction of local resonances, or if it is simply due to the changes incurred to the scattering environment. To address this question, we considered a few more NPM configurations with the same dimensions except for the nanopillar height, which was varied. The  $k_r$  predictions for these systems are plotted in figure 38, where we see a significant dependence on the nanopillar height. The drop in  $k_r$  extends from the already significant value of 73% reduction (with a 9.78 nm tall single nanopillar, which is the same height as the membrane thickness) to a significant value of 98.7% reduction (with a 586.5 nm tall nanopillar, which is 60 times taller than the membrane thickness). The latter value corresponds to a factor of 75.1 reduction compared to a uniform membrane with the same thickness. The display of such strong dependence on the nanopillar height is consistent with what we expect from the local resonance mechanism because, as described earlier, the number of local resonances (vibrons) is proportional

to the nanoresonator size, and therefore a tall nanopillar produces more sizable mode localizations as well as more group-velocity reductions for the heat-carrying phonons compared to a short nanopillar. These results are obtained by comparing, and replottting in a different format, several data points reported in [190]. The observed dependency on nanopillar height is in contrast to the conclusions drawn in [328] where the authors select for their analysis data points from [190] that correspond to an NPM with a smaller membrane thickness and smaller nanopillar-to-base membrane volume fraction—where the effect of increasing the nanopillar height is less profound.

The overall size of the NPM determines the strength of the dependency of  $k_r$  on the nanopillar height [190]. To examine this aspect of the problem, we refer to a broader set of results from reference [190], where we consider three sets of NPMs of different membrane thicknesses and nanopillar spacings and widths, for both cases with a single nanopillar (top) and cases with double nanopillars (top and bottom). Using compact notation, the cases we consider are NPMs with the following dimensions:  $6\alpha \times 6\alpha \times 6\alpha + (6\alpha - 2) \times (6\alpha - 2) \times 6\alpha$  CC,  $6\alpha \times 6\alpha \times 6\alpha + (6\alpha - 2) \times (6\alpha - 2) \times 6\alpha^2$  CC, and  $6\alpha \times 6\alpha \times 6\alpha + (6\alpha - 2) \times (6\alpha - 2) \times 6\alpha\beta$  CC (for single nanopillars) or  $6\alpha \times 6\alpha \times 6\alpha + (6\alpha - 2) \times (6\alpha - 2) \times 6\alpha\beta + (6\alpha - 2) \times (6\alpha - 2) \times 6\alpha\beta$  CC (for double nanopillars), where CC denotes units of conventional cells,  $\alpha$  is a scaling size factor, and  $\beta = h/e$ . Figure 39 provides a summary of the results for a selection of NPM configurations corresponding to  $\alpha = 1, 2, \text{ and } 3$  and  $\beta = 20, 30, \text{ and } 60$ . To guide the eye, schematics of the considered unit cells are shown in figures 39(a) and (b). As explained in [190], the higher the value of  $\alpha$  in these cases, the greater the reduction in thermal conductivity obtained by an increase in nanopillar height. In other words, the larger the value of  $\alpha$ , the more delayed the saturation of  $k_r$  with nanopillar height. This is because the larger the width of the base membrane, the more width is available for a nanopillar with a given height—this attribute is encoded in selecting the nanopillar width to be  $(6\alpha - 2) \times (6\alpha - 2)$ , instead of, for example,  $5\alpha \times 5\alpha$ . A larger nanopillar width corresponds to a larger volume and number of atoms, which in turn means more vibrons are available for contribution to the thermal conductivity reduction. The ratio of nanopillar volume to base membrane volume  $V_r$  is ultimately the key quantity that determines the performance of a nanopillared NPM.

Figure 39(c) collects the results for the largest  $h$  in each of the three  $\alpha$  sets. For the double-nanopillar case with a membrane thickness of  $e = 9.78$  nm and a nanopillar height of 586.55 nm, an exceptionally strong value of thermal conductivity reduction is recorded: a factor of 130.0 reduction compared to a corresponding uniform membrane. Not only is this a very promising result for thermoelectric energy conversion, it is also advantageous from a practical point of view because it demonstrates the ability to maintain high performance with upscaling of the size of the NPM unit cell—via the vibron

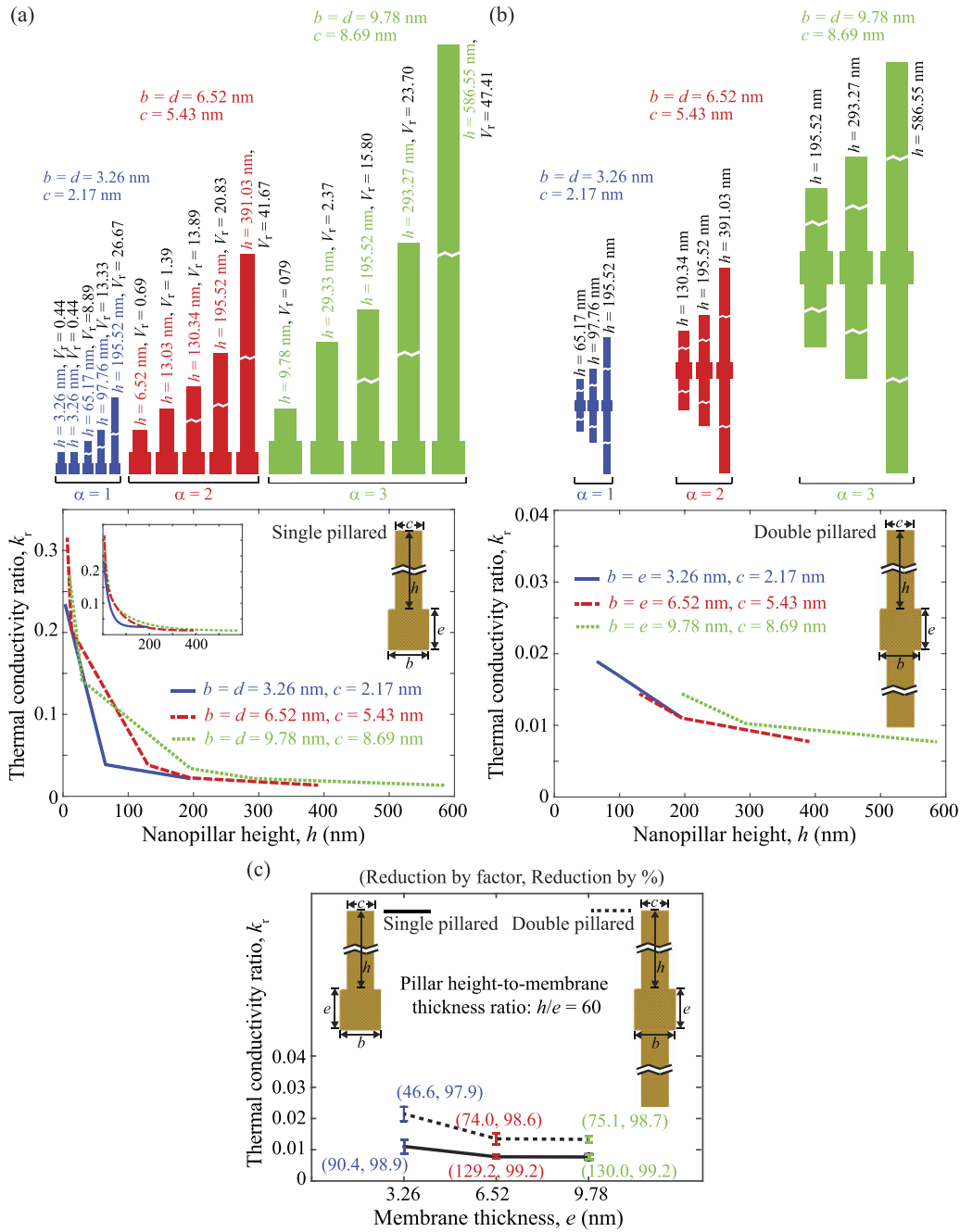


**Figure 39.** Thermal conductivity ratio  $k_r$  versus nanopillar height for a variety of (a) single-pillared and (b) double-pillared membranes with progressively increasing membrane thickness, nanopillar spacing, nanopillar width, and nanopillar height. The relative geometries are based on the  $\alpha$ -formulae provided in the text;  $V_r$  values are noted. (c) Thermal conductivity ratio  $k_r$  versus membrane thickness for configuration  $6a \times 6a \times 6a + (6\alpha - 2) \times (6\alpha - 2) \times 6\alpha\beta + (6\alpha - 2) \times (6\alpha - 2) \times 6\alpha\beta$  CC (single) and  $6a \times 6a \times 6a + (6\alpha - 2) \times (6\alpha - 2) \times 6\alpha\beta$  CC (double) and a nanopillar height selected such that the aspect ratio is  $\beta = h/e = 60$ . Numbers in parentheses indicate the thermal conductivity reduction due to addition of the nanopillar, given as a multiplication factor (first number) and as a percentage (second number). It is shown that the onset of saturation with nanopillar height is delayed as we advance the  $\alpha$  value in these formulae. Reprinted figure with permission from [190], Copyright (2018) by the American Physical Society.

compensation scheme described earlier. This latter advantage is vital for enabling industrial-scale deployment for waste heat conversion to electricity and for cooling and refrigeration.

As discussed in section 6.2.1, the degree of conformity between the phonon and vibron DOS directly influences the strength of the thermal conductivity reduction. High conformity means more matching between the nanopillar local reso-

nance frequencies and the base membrane phonon dispersion curves. This, in turn, means a greater decrease in  $k_r$  due to higher occurrence of the three resonance-related effects mentioned earlier: namely, the phonon group velocity reductions, the mode localizations, and the reduction in lifetimes associated with the changes in the dispersion curves. MD simulations with the same run-time parameters mentioned above were conducted on the two NPM unit cells featured in figure 36. The

unit cell with the smaller nanopillar (shown in figure 36(a)) has a nonconformity factor of  $\hat{R}_{pv} = 654$  and a value of  $k_r = 0.41$ . In contrast, the unit cell with the larger nanopillar (shown in figure 36(b)) has a nonconformity factor of  $\hat{R}_{pv} = 47$  and a value of  $k_r = 0.19$ . This confirms the direct correlation between phonon–vibron DOS conformity and reduction in thermal conductivity.

A recent study of NPMs produced results that are perfectly explained by the phonon–vibron DOS conformity measure and its relation to the strength of thermal conductivity reduction. Ma *et al* [320] investigated a graphene nanoribbon with a periodic arrangement of branched substructures acting as nanoresonators. The substructures, also referred to as pillars in their work, branched out perpendicularly from the sides along the main axis of the nanoribbon. Several MD simulations were conducted where in each simulation a different isotope of carbon was used for the atoms forming the pillars, while all atoms in the central region of the graphene sheet (i.e. the backbone region where the pillars are branching from) was formed from  $C^{12}$ . The thermal conductivity along the axis of the nanoribbon was calculated for each case. The results showed that the lowest thermal conductivity is for the case where the isotope used in the pillars was  $C^{12}$ , i.e. the same isotope as the one used in the central region. As the isotope mass in the pillars was decreased or increased from  $C^{12}$ , the level of thermal conductivity reduction decreased (i.e. the absolute thermal conductivity increased compared to the optimal case). This result provides an indication that the prime cause of thermal conductivity reduction is the presence of pillar local resonances. When the pillars and the central regions are made out of the same carbon isotope, the degree of conformity between the phonon and vibron DOS is maximized, similar to the case shown in figure 36(b). As the isotope of the pillars deviates from that of the central region, the pillar vibron DOS distribution alters due to shifts in the local resonances, and therefore deviates from the DOS of the phonons propagating in the central region. The degree of conformity weakens as the value of the difference in atomic mass between the pillar and central region isotopes increases. The lower the conformity, the less intense the mode localization, resonance hybridizations, and resonance-related lifetime drops, and therefore the smaller the reduction in thermal conductivity. A possible exception would be a case where the mass of the nanopillar atoms is significantly higher than the mass of the base membrane atoms to cause very substantial reductions in the frequencies of the vibrons, which as a net effect might be favorable for thermal conductivity reduction. The results by Ma *et al* [320] also suggest that the reduction cannot be primarily due to boundary scattering. This is because their pillar sizes and shapes are kept constant; thus, if boundary scattering was the prime effect then the thermal conductivity reduction verses pillar isotope value curve would have been mostly constant rather than exhibiting a strong minimum value at the point where the isotopes of the pillars and the central region are equal. For the analysis of this system to be complete, the effects of interface scattering across materials with dissimilar isotopes should also be taken into account.

## 6.5. Summary

In this section, the concept of an NPM has been reviewed and discussed with a focus on the particular configuration of a nanopillared membrane. Similar to the pillared elastic metamaterials discussed in the previous sections, at the nanoscale we also benefit from the phenomenon of local resonance and its coupling with the underlying dispersion curves of the base membrane (or plate). The differences, however, are both fundamental and numerous. First, NPMs are engineered to manipulate nanoscale thermal transport properties; therefore, they are necessarily formed at very small scales corresponding to frequencies reaching a few terahertz. This is in significant contrast to the frequencies at least an order of magnitude lower at larger size scales. Second, the interest here is not in subwavelength band gaps and/or effective properties. Instead, the target resonance-induced effects are (1) the flattenings of the dispersion curves, (2) the mode localizations (within the nanopillars), and (3) the moderate reductions in the phonon lifetimes due to changes in the dispersion curves. The notion of phonon lifetimes in itself underscores yet another key contrast with most macroscale metamaterials, because it is a manifestation of the highly nonlinear nature of nanoscale thermal transport. Third, and of critical importance, all these effects take place due to the presence of an extremely large number of local resonances, referred to as vibrons in this context, that span the entire frequency spectrum covered by the phonon dispersion curves characterizing wave motion in the host medium. Unlike macroscopic metamaterials, an NPM benefits from local resonances in both the subwavelength and superwavelength regimes. When the unit cell of the nanopillared membrane is designed such that (1) the number of vibrons is maximized and (2) the overall conformity between the vibron and phonon DOS across the spectrum is maximized, the total impact of these three effects in turn is maximized, and so is the reduction in the in-plane lattice thermal conductivity of the NPM.

Maximizing these NPM design factors requires the ratio  $V_r$  of nanopillar volume to base membrane volume to be as large as possible. A large nanoresonator increases both the number of vibrons and the DOS conformity factor; the latter is illustrated in figure 36. Increasing  $V_r$  requires the membrane width in the unit cell to be as large as possible, as this enables ample increase in nanopillar width. The rewards of increasing the nanopillar height become more significant for wider-sized NPM unit cells, as illustrated in figure 39. Increasing the base membrane size, however, should not reach the point where the ratio of noncoherent-to-coherent phonon transport becomes excessively large [190]. Key to this limitation is the range and distribution of the phonon MFP at the temperature of interest. As the dimensions of the NPM components increase, less of the phonon MFP distribution becomes available for the resonance-induced wave effects to take place. An immense advantage of silicon is that it exhibits a wide MFP that ranges from a few nanometers to a few micrometers at room temperature [338]. It is also noteworthy that as the size of the nanopillar increases in width and/or height, eventually the spectrum starts to become saturated with vibrons, which

also contributes to the slowing rate of the thermal conductivity reduction observed in figure 38. The reader is referred to reference [190] for a comprehensive investigation on the impact of base membrane and nanopillar size on the reduction of thermal conductivity in NPMs.

## 7. Summary and perspective

Since the seminal works published in 2008 on pillared plates, pillared materials and surfaces have been witnessing continuous growth as a new form of phononic crystals, metamaterials, and metasurfaces by researchers from a broad range of disciplines. In these systems, numerous avenues are available for manipulation of wave dispersion along the base plate or substrate by tailoring the local resonance properties of the branching pillar(s). This platform continues to inspire new fundamental and applied research. In this review, we first gave an overview of the historical developments as well as the current state of the art of pillared phononic crystals, metamaterials, and metasurfaces. Then, we reviewed the mechanism for opening a low-frequency hybridization band gap and discussed its tunability and applications such as waveguiding. The interaction with electromagnetic waves was covered, especially considering the simultaneous existence of phononic and photonic band gaps, a phenomenon which has been termed phoXonic band gaps. The support of elastoplasmonic interaction was also presented with an elaboration on the fundamental coupling mechanisms between localized plasmon modes and elastic modes. In addition, the tunability and application of WGMs and liquid compressional modes were discussed for phononic crystal plates with hollow pillars. In the third section, we reviewed the metamaterial aspect of pillared plates. Trampoline and tailored metamaterial plates were analyzed for widening and lowering band gaps. We reviewed acoustic metalenses with locally resonant pillars and discussed how these allow for nearfield subdiffraction focusing. It was explained that polarization coherence between flexural resonances of the pillars and the antisymmetric Lamb mode in a base plate enhances the evanescent wave along the interface through elastic energy re-emitted by the resonators. In the fourth section, we discussed how intrinsic resonances of a single pillar or a line of pillars can provide a second source to emit Lamb waves that interfere with incident Lamb waves, a mechanism that results in a dip in amplitude and/or phase change of the transmitted wave. Wavefront manipulation by phase and diffraction engineering of pillared metasurfaces was reviewed. The existence and behavior of Fano resonance, EIT, and ATS were also discussed. In the fifth section, the basic concept of a topological mechanism for a pillared phononic plate was described. We reviewed the robustness of topologically protected edge states against backscattering, defects, and random perturbations. In the sixth section, the concept of an NPM for thermal conductivity reduction was reviewed. Unlike macroscopic metamaterials, including pillared acoustic/elastic metamaterials, an NPM is a highly nonlinear medium that utilizes resonances across the entire spectrum and not only in the subwavelength regime. The NPM resonances may be in the millions. We provided an overview of the three resonance-induced effects that

cause thermal conductivity reduction in a nanopillared membrane: namely, group velocity reduction of the heat-carrying phonons in the base membrane, mode localizations in the nanopillars, and controlled reductions in the lifetimes due to changes in the dispersion curves. We also discussed the key aspect of size dependence in this class of problems, and how NPM design may be optimized for sustained performance with upscaling in size up to the limit where the transport transitions from primarily wave-based to completely diffusive transport.

Pillared phononic crystals, metamaterials, and metasurfaces have been proven to provide a fertile platform for a wide range of novel physical phenomena and potentially high-impact applications in industry and everyday life. A nonexhaustive list of some challenges, opportunities, and open topics for the future includes:

- (a) A pillar can be regarded as a complex resonator exhibiting a multitude of compressional, bending, and torsional modes with different orders. By combining plate theory and the plane-wave expansion method, simplified mathematical models considering out-of-plane displacement (antisymmetric Lamb mode) and a pillar's compressional mode were developed [162, 164, 343]. However, there is still an opportunity for the development of rigorous mathematical treatments—using techniques such as the homogenization method and the multiple scattering method—considering in-plane displacements and the pillar's full modes using 3D continuous elastic models. Full utilization of a 3D pillar's diverse modal content will provide new prospects for applications. Furthermore, the realization of resonating attachments in the form of mechanical mechanisms that induce inertial amplification is an area that has tremendous potential for new prospects in band-gap engineering [44].
- (b) The interplay between local resonances and dissipation triggers a rich dynamical regime. Known as *metadamping* [344, 345], this interplay may be tuned to enhance [344–350] or reduce [346–349] dissipation compared to a statically equivalent material. The tuning of metadamping with a 3D pillar adds to the complexity of the problem due to the presence of a crowded band structure and numerous resonance hybridizations. Future work will finetune this design process to realize practical configurations for effective *loss engineering*. Analogous avenues may also be pursued in examining the interplay between local resonances and nonlinearity [351–353].
- (c) Most studies of pillared phononic crystals and metamaterials consider pillars arranged on a periodic lattice. On the other hand, random systems have rich physical properties in their own right and also a potentially wide spectrum of applications. Random induced effects on band gaps, localizations, acoustic transmission, mode conversion, phase transition, and nanoscale thermal transport, among others, provide potential for new advancements in applied physics or related disciplines. This can take shape in the form of disordered pillared phononic crystals or completely random pillared metamaterials, since the key local resonance effects do not depend on periodicity.

- (d) Robust wave phenomena under topological protection in a pillared platform provide a range of yet-to-be-explored avenues. In addition to the conventional elastic wave theory based on Newtonian equations, topological concepts provide new tools to describe band theory and to synthesize wave functionality based on novel properties. As long as introduced local perturbations are not overly strong to close nontrivial band gaps, the generalized properties of wavefunctions sweeping a band described by topology are conserved against these local perturbations. In a pillared platform, there is strong potential in achieving robust elastic wave states as a mechanical analog of higher-order topological insulators, Anderson topological insulators, topological bound states in a continuum, and topological phases in Moiré superlattices, among others. A wide range of applications such as nanomechanical devices, on-chip phononic networks, and information processing stand to benefit from this quantum-mechanics-inspired track of research.
- (e) There is a growing interest in the field of metasurfaces where very thin (subwavelength) structures with a modulation of the transmission and reflection (phase and amplitude) properties of the constitutive unit cells enable various functionalities for anomalous refraction and imaging. The rich resonant properties of an array of pillars open opportunities towards design of a metaline of pillars [258]—in analogy to a metasurface—to steer elastic waves (Lamb waves, Rayleigh waves, transverse beam waves, etc) in configurations exhibiting salient properties, for example, nonlocally resonant [348, 354–358], non-Hermitian [359, 360], and parity-time symmetry systems [361, 362]. Promising diverse applications such as cloaking, energy absorbing, asymmetric transmission, realization of topological states or bound states in a continuum, wave isolation, focusing, wave deflection, and energy harvesting, among others, can be achieved at different size scales and with the possibility of controlled interaction with other physical fields. The pillar platform is naturally of particular interest in view of the engineering applications of Lamb waves and SAWs.
- (f) Deep learning, which is an artificial intelligence method for the exploration of new horizons of recognition and processing of data, is growing significantly and penetrating multiple disciplines such as device design in optics [363], acoustics [364], plasmonics [365, 366] and metamaterials [367]. With the help of deep learning and large-data science, pillared phononic crystals, for example, will be able to detect and predict objects faster and more efficiently [368], or be used for inverse design of topological edge states [369]. More opportunities for pillared phononic crystals, metamaterials, and metasurfaces are anticipated in this area.
- (g) The upscaling of NPMs and their effective integration into practical thermoelectric device architectures are two key steps for the near future. This presents both a rich material physics problem because of the inherent size effects of conductive thermal transport, and a challenging

technological problem because of the need for both high efficiency and low cost for industrial competitiveness.

The notion of a surface represents a fundamental natural boundary for a material. In this article, we reviewed an emerging and vibrant body of research dedicated to the physics of 2D and semi-infinite acoustic/elastic/condensed-matter media featuring surfaces enriched with substructures designed to manipulate the very nature of surface waves and related phenomena. The science of surface vibrational resonances is taking shape as a thriving subdiscipline of phononics and applied physics. While rooted in boundary effects, the scope of this area of research appears boundless for the foreseeable future.

## Acknowledgments

This work was supported by the National Natural Science Foundation of China (Grant No. 11902223), the Shanghai Pujiang Program (Grant No. 19PJ1410100), the program for Professor of Special Appointment (Eastern Scholar) at Shanghai Institutions of Higher Learning, the High-Level Foreign Expert Program of Tongji University, and the Fundamental Research Funds for the Central Universities. The work was also supported by the Advanced Research Projects Agency-Energy (ARPA-E) Grant No. DE-AR0001056. Y Jin and M I Hussein are grateful to graduate students in their groups for their assistance in proofreading the manuscript.

## ORCID iDs

Yabin Jin  <https://orcid.org/0000-0002-6991-8827>  
 Yan Pennec  <https://orcid.org/0000-0002-4719-9913>  
 Bernard Bonello  <https://orcid.org/0000-0003-4375-4235>  
 Hossein Honarvar  <https://orcid.org/0000-0002-1592-2759>  
 Leonard Dobrzynski  <https://orcid.org/0000-0002-4508-1305>  
 Bahram Djafari-Rouhani  <https://orcid.org/0000-0001-6983-9689>  
 Mahmoud I Hussein  <https://orcid.org/0000-0002-6583-1425>

## References

- [1] Johnson S G and Joannopoulos J D 2001 *Photonic Crystals: The Road from Theory to Practice* (Berlin: Springer)
- [2] Deymier P A 2013 *Acoustic Metamaterials and Phononic Crystals* (Berlin: Springer)
- [3] Laude V 2015 *Phononic Crystals: Artificial Crystals for Sonic, Acoustic, and Elastic Waves* (Berlin: de Gruyter & Co)
- [4] Khelif A and Adibi A 2015 *Phononic Crystals: Fundamentals and Applications* (Berlin: Springer)
- [5] Sánchez-Dehesa J and Krokhn A 2016 Introduction to acoustics of phononic crystals. Homogenization at low frequencies *Phononic Crystals: Fundamentals and Applications* ed A Khelif and A Adibi (New York: Springer) pp 1–21
- [6] Phani A S and Hussein M I 2017 *Dynamics of Lattice Materials* (New York: Wiley)
- [7] Bloch F 1929 Über die quantenmechanik der elektronen in kristallgittern *Z. Phys.* **52** 555–600

- [8] Yablonovitch E 1987 Inhibited spontaneous emission in solid-state physics and electronics *Phys. Rev. Lett.* **58** 2059–62
- [9] John S 1987 Strong localization of photons in certain disordered dielectric superlattices *Phys. Rev. Lett.* **58** 2486
- [10] Sigalas M M and Economou E N 1992 Elastic and acoustic wave band structure *J. Sound Vib.* **158** 377–82
- [11] Sigalas M and Economou E N 1993 Band structure of elastic waves in two dimensional systems *Solid State Commun.* **86** 141–3
- [12] Kushwaha M S, Halevi P, Dobrzynski L and Djafari-Rouhani B 1993 Acoustic band structure of periodic elastic composites *Phys. Rev. Lett.* **71** 2022–5
- [13] Mead D M 1996 Wave propagation in continuous periodic structures: research contributions from Southampton *J. Sound. Vib.* **190** 495–524
- [14] Royer D, Morgan D P and Dieulesaint E 1999 *Elastic Waves in Solids I: Free and Guided Propagation* (Berlin: Springer)
- [15] Brillouin L 2003 *Wave Propagation in Periodic Structures: Electric Filters and Crystal Lattices* (New York: Dover)
- [16] Pennec Y and Djafari-Rouhani B 2016 Fundamental properties of phononic crystal *Phononic Crystals: Fundamentals and Applications* ed A Khelif and A Adibi (New York: Springer) pp 23–50
- [17] Gorishnyy T, Maldovan M, Ullal C and Thomas E 2005 Sound ideas *Phys. World* **18** 24
- [18] Alonso-Redondo E, Schmitt M, Urbach Z, Hui C M, Sainidou R, Rembert P, Matyjaszewski K, Bockstaller M R and Fytas G 2015 A new class of tunable hypersonic phononic crystals based on polymer-tethered colloids *Nat. Commun.* **6** 8309
- [19] Liu Z, Zhang X, Mao Y, Zhu Y Y, Yang Z, Chan C T and Sheng P 2000 Locally resonant sonic materials *Science* **289** 1734
- [20] Pendry J B, Holden A J, Robbins D J and Stewart W J 1999 Magnetism from conductors and enhanced nonlinear phenomena *IEEE Trans. Microw. Theory Tech.* **47** 2075–84
- [21] Smith D R, Padilla W J, Vier D C, Nemat-Nasser S C and Schultz S 2000 Composite medium with simultaneously negative permeability and permittivity *Phys. Rev. Lett.* **84** 4184–7
- [22] Pennec Y, Vasseur J O, Djafari-Rouhani B, Dobrzyński L and Deymier P A 2010 Two-dimensional phononic crystals: examples and applications *Surf. Sci. Rep.* **65** 229–91
- [23] Maldovan M 2013 Sound and heat revolutions in phononics *Nature* **503** 209–17
- [24] Hussein M I, Leamy M J and Ruzzene M 2014 Dynamics of phononic materials and structures: historical origins, recent progress, and future outlook *Appl. Mech. Rev.* **66** 040802
- [25] Ma G and Sheng P 2016 Acoustic metamaterials: From local resonances to broad horizons *Sci. Adv.* **2** e1501595
- [26] Pennec Y, Djafari-Rouhani B, Larabi H, Vasseur J O and Hladky-Hennion A C 2008 Low-frequency gaps in a phononic crystal constituted of cylindrical dots deposited on a thin homogeneous plate *Phys. Rev. B* **78** 104105
- [27] Wu T-T, Huang Z-G, Tsai T-C and Wu T-C 2008 Evidence of complete band gap and resonances in a plate with periodic stubbed surface *Appl. Phys. Lett.* **93** 111902
- [28] Oudich M, Senesi M, Assouar M B, Ruzenne M, Sun J-H, Vincent B, Hou Z and Wu T-T 2011 Experimental evidence of locally resonant sonic band gap in two-dimensional phononic stubbed plates *Phys. Rev. B* **84** 165136
- [29] Khales H, Hassen-Bey A and Khelif A 2013 Evidence of ultrasonic band gap in aluminum phononic crystal beam *J. Vib. Acoust.* **135** 041007
- [30] Rupin M, Lemoult F, Lerosey G and Roux P 2014 Experimental demonstration of ordered and disordered multiresonant metamaterials for Lamb waves *Phys. Rev. Lett.* **112** 234301
- [31] Rupin M, Roux P, Lerosey G and Lemoult F 2015 Symmetry issues in the hybridization of multi-mode waves with resonators: an example with Lamb waves metamaterial *Sci. Rep.* **5** 13714
- [32] Achaoui Y, Khelif A, Benchabane S, Robert L and Laude V 2011 Experimental observation of locally-resonant and Bragg band gaps for surface guided waves in a phononic crystal of pillars *Phys. Rev. B* **83** 104201
- [33] Hsu J-C 2011 Low-frequency forbidden bands in phononic crystal plates with Helmholtz resonators *Japan. J. Appl. Phys.* **50** 07HB01
- [34] Li Y, Zhu L and Chen T 2017 Plate-type elastic metamaterials for low-frequency broadband elastic wave attenuation *Ultrasonics* **73** 34–42
- [35] Zhang H-b, Chen J-j and Han X 2012 Lamb wave band gaps in a homogenous plate with periodic tapered surface *J. Appl. Phys.* **112** 054503
- [36] Chen J-j, Zhang H-b and Han X 2013 Local resonance broadband gap in a homogeneous plate with periodic truncated cones *Japan. J. Appl. Phys.* **52** 034301
- [37] Oudich M, Li Y, Assouar B M and Hou Z 2010 A sonic band gap based on the locally resonant phononic plates with stubs *New J. Phys.* **12** 083049
- [38] Hu A, Zhang X, Wu F and Yao Y 2014 Enlargement of the locally resonant Lamb wave band gap of the phononic crystal plate at the deep sub-wavelength scale *Mater. Res. Express* **1** 045801
- [39] Crut A, Maioli P, Del Fatti N and Vallée F 2015 Acoustic vibrations of metal nano-objects: time-domain investigations *Phys. Rep.* **549** 1–43
- [40] Zhao H-J, Guo H-W, Gao M-X, Liu R-Q and Deng Z-Q 2016 Vibration band gaps in double-vibrator pillared phononic crystal plate *J. Appl. Phys.* **119** 014903
- [41] Li S, Chen T, Wang X, Li Y and Chen W 2016 Expansion of lower-frequency locally resonant band gaps using a double-sided stubbed composite phononic crystals plate with composite stubs *Phys. Lett. A* **380** 2167–72
- [42] Li L and Cai A 2016 Control of the low-frequency vibrations of elastic metamaterial shafts with discretized arc-rubber layers *Japan. J. Appl. Phys.* **55** 067301
- [43] Sugino C, Leadenham S, Ruzzene M and Erturk A 2016 On the mechanism of bandgap formation in locally resonant finite elastic metamaterials *J. Appl. Phys.* **120** 134501
- [44] Frandsen N M M, Bilal O R, Jensen J S and Hussein M I 2016 Inertial amplification of continuous structures: large band gaps from small masses *J. Appl. Phys.* **119** 124902
- [45] Lu K, Wu J H, Jing L, Gao N and Guan D 2017 The two-degree-of-freedom local resonance elastic metamaterial plate with broadband low-frequency bandgaps *J. Phys. D: Appl. Phys.* **50** 095104
- [46] Huang Z-G 2011 Silicon-based filters, resonators and acoustic channels with phononic crystal structures *J. Phys. D: Appl. Phys.* **44** 245406
- [47] Wang X-P, Jiang P, Chen T-N and Zhu J 2015 Tuning characteristic of band gap and waveguide in a multi-stub locally resonant phononic crystal plate *AIP Adv.* **5** 107141
- [48] Zou K, Ma T-X and Wang Y-S 2016 Investigation of complete bandgaps in a piezoelectric slab covered with periodically structured coatings *Ultrasonics* **65** 268–76
- [49] Zhou C, Sai Y and Chen J 2016 Tunable Lamb wave band gaps in two-dimensional magnetoelastic phononic crystal slabs by an applied external magnetostatic field *Ultrasonics* **71** 69–74
- [50] Jiang P 2017 Low-frequency band gap and defect state characteristics in a multi-stub phononic crystal plate with slit structure *J. Appl. Phys.* **121** 015106
- [51] Ma J, Hou Z and Assouar B M 2014 Opening a large full phononic band gap in thin elastic plate with resonant units *J. Appl. Phys.* **115** 093508
- [52] Zhang S, Hui Wu J and Hu Z 2013 Low-frequency locally resonant band-gaps in phononic crystal plates with periodic spiral resonators *J. Appl. Phys.* **113** 163511

- [53] Ming C, Chen J, Han X and Zhang H 2013 Lamb wave band gaps in a homogenous plate with periodic Gaussian surfaces *Phys. Scr.* **88** 035601
- [54] El Hassouani Y *et al* 2010 Dual phononic and photonic band gaps in a periodic array of pillars deposited on a thin plate *Phys. Rev. B* **82** 155405
- [55] Pourabolghasem R, Khelif A, Mohammadi S, Eftekhari A A and Adibi A 2014 Physics of band-gap formation and its evolution in the pillar-based phononic crystal structures *J. Appl. Phys.* **116** 013514
- [56] Miranda E J P Jr, Nobrega E D, Ferreira A H R and Dos Santos J M C 2019 Flexural wave band gaps in a multi-resonator elastic metamaterial plate using Kirchhoff–Love theory *Mech. Syst. Signal Process.* **116** 480–504
- [57] Hsu J-C 2011 Local resonances-induced low-frequency band gaps in two-dimensional phononic crystal slabs with periodic stepped resonators *J. Phys. D: Appl. Phys.* **44** 055401
- [58] Khelif A, Achaoui Y and Aoubiza B 2012 Surface acoustic waves in pillars-based two-dimensional phononic structures with different lattice symmetries *J. Appl. Phys.* **112** 033511
- [59] Assouar M B, Sun J-H, Lin F-S and Hsu J-C 2014 Hybrid phononic crystal plates for lowering and widening acoustic band gaps *Ultrasonics* **54** 2159–64
- [60] Zhang Z, Han X and Ji G 2017 The bandgap controlling by geometrical symmetry design in hybrid phononic crystal *Int. J. Mod. Phys. B* **32** 1850034
- [61] Achaoui Y, Laude V, Benchabane S and Khelif A 2013 Local resonances in phononic crystals and in random arrangements of pillars on a surface *J. Appl. Phys.* **114** 104503
- [62] Celli P and Gonella S 2015 Manipulating waves with LEGO bricks: a versatile experimental platform for metamaterial architectures *Appl. Phys. Lett.* **107** 081901
- [63] Assouar B and Oudich M 2012 Enlargement of a locally resonant sonic band gap by using double-sided stubbed phononic plates *Appl. Phys. Lett.* **100** 123506
- [64] Wang P, Chen T-N, Yu K-P and Wang X-P 2013 Lamb wave band gaps in a double-sided phononic plate *J. Appl. Phys.* **113** 053509
- [65] Zhao H-J, Guo H-W, Li B-Y, Deng Z-Q and Liu R-Q 2015 Flexural vibration band gaps in a double-side phononic crystal plate *J. Appl. Phys.* **118** 044906
- [66] Song A, Wang X, Chen T, Jiang P and Bao K 2016 Low-frequency bandgaps of two-dimensional phononic crystal plate composed of asymmetric double-sided cylinder stubs *Int. J. Mod. Phys. B* **30** 1650029
- [67] Li S, Xi Y, Chen T and Wang X 2017 Modulating Lamb wave band gaps using an elastic metamaterial plate *Acoust. Phys.* **63** 508–16
- [68] Jin Y, Fernez N, Pennec Y, Bonello B, Moiseyenko R P, Hémon S, Pan Y and Djafari-Rouhani B 2016 Tunable waveguide and cavity in a phononic crystal plate by controlling whispering-gallery modes in hollow pillars *Phys. Rev. B* **93** 054109
- [69] Jin Y, Pennec Y, Pan Y and Djafari-Rouhani B 2016 Phononic crystal plate with hollow pillars actively controlled by fluid filling *Crystals* **6** 64
- [70] Jin Y, Pennec Y, Pan Y and Djafari-Rouhani B 2017 Phononic crystal plate with hollow pillars connected by thin bars *J. Phys. D: Appl. Phys.* **50** 035301
- [71] Li Y, Chen T, Wang X, Yu K and Chen W 2014 Propagation of Lamb waves in one-dimensional radial phononic crystal plates with periodic corrugations *J. Appl. Phys.* **115** 054907
- [72] Shu F, Liu Y, Wu J and Wu Y 2016 Band gap in tubular pillar phononic crystal plate *Ultrasonics* **71** 172–6
- [73] Wang T-T, Wang Y-F, Wang Y-S and Laude V 2017 Tunable fluid-filled phononic meta-strip *Appl. Phys. Lett.* **111** 041906
- [74] Wang Y-F, Wang T-T, Wang Y-S and Laude V 2017 Reconfigurable phononic-crystal circuits formed by coupled acoustoelastic resonators *Phys. Rev. Appl.* **8** 014006
- [75] Bilal O R and Hussein M I 2013 Trampoline metamaterial: local resonance enhancement by springboards *Appl. Phys. Lett.* **103** 111901
- [76] Ma C, Guo J and Liu Y 2015 Extending and lowering band gaps in one-dimensional phononic crystal strip with pillars and holes *J. Phys. Chem. Solids* **87** 95–103
- [77] Coffy E, Lavergne T, Addouche M, Euphrasie S, Vairac P and Khelif A 2015 Ultra-wide acoustic band gaps in pillar-based phononic crystal strips *J. Appl. Phys.* **118** 214902
- [78] Bilal O R, Foehr A and Daraio C 2017 Observation of trampoline phenomena in 3D-printed metamaterial plates *Extreme Mech. Lett.* **15** 103–7
- [79] Coffy E, Euphrasie S, Addouche M, Vairac P and Khelif A 2017 Evidence of a broadband gap in a phononic crystal strip *Ultrasonics* **78** 51–6
- [80] Casadei F, Delpero T, Bergamini A, Ermanni P and Ruzzene M 2012 Piezoelectric resonator arrays for tunable acoustic waveguides and metamaterials *J. Appl. Phys.* **112** 064902
- [81] Jin Y, Bonello B and Pan Y 2014 Acoustic metamaterials with piezoelectric resonant structures *J. Phys. D: Appl. Phys.* **47** 245301
- [82] Bergamini A, Delpero T, Simoni L D, Lillo L D, Ruzzene M and Ermanni P 2014 Phononic crystal with adaptive connectivity *Adv. Mater.* **26** 1343–7
- [83] Bergamini A E, Zündel M, Flores Parra E A, Delpero T, Ruzzene M and Ermanni P 2015 Hybrid dispersive media with controllable wave propagation: a new take on smart materials *J. Appl. Phys.* **118** 154310
- [84] Zhou W, Wu Y and Zuo L 2015 Vibration and wave propagation attenuation for metamaterials by periodic piezoelectric arrays with high-order resonant circuit shunts *Smart Mater. Struct.* **24** 065021
- [85] Chen S, Fan Y, Fu Q, Wu H, Jin Y, Zheng J and Zhang F 2018 A review of tunable acoustic metamaterials *Appl. Sci.* **8** 1480
- [86] Khelif A, Achaoui Y, Benchabane S, Laude V and Aoubiza B 2010 Locally resonant surface acoustic wave band gaps in a two-dimensional phononic crystal of pillars on a surface *Phys. Rev. B* **81** 214303
- [87] Khelif A, Achaoui Y and Aoubiza B 2011 In-plane confinement and waveguiding of surface acoustic waves through line defects in pillars-based phononic crystal *AIP Adv.* **1** 041404
- [88] Oudich M and Badreddine Assouar M 2012 Surface acoustic wave band gaps in a diamond-based two-dimensional locally resonant phononic crystal for high frequency applications *J. Appl. Phys.* **111** 014504
- [89] Li Y and Hou Z 2013 Surface acoustic waves in a two-dimensional phononic crystal slab with locally resonant units *Solid State Commun.* **173** 19–23
- [90] Guo Y, Schubert M and Dekorsy T 2016 Finite element analysis of surface modes in phononic crystal waveguides *J. Appl. Phys.* **119** 124302
- [91] Zhang D, Zhao J, Bonello B, Zhang F, Yuan W, Pan Y and Zhong Z 2017 Investigation of surface acoustic wave propagation in composite pillar based phononic crystals within both local resonance and Bragg scattering mechanism regimes *J. Phys. D: Appl. Phys.* **50** 435602
- [92] Ash B, Worsfold S, Vukusic P and Nash G 2017 A highly attenuating and frequency tailorable annular hole phononic crystal for surface acoustic waves *Nat. Commun.* **8** 174
- [93] Djafari Rouhani B, Pennec Y, El Boudouti E H, Vasseur J, El Hassouani Y, Li C, Akjouj A and Bria D 2011 Band gap engineering in simultaneous phononic and photonic crystal slabs *Appl. Phys. A* **103** 735–9

- [94] Laude V, Belkhir A, Alabiad A F, Addouche M, Benchabane S, Khelif A and Baida F I 2017 Extraordinary nonlinear transmission modulation in a doubly resonant acousto-optical structure *Optica* **4** 1245–50
- [95] Wu T T, Hsu J C and Sun J H 2011 Phononic plate waves *IEEE Trans. Ultrason., Ferroelect., Freq. Control* **58** 2146–61
- [96] Oudich M, Djafari-Rouhani B, Pennec Y, Assouar M B and Bonello B 2014 Negative effective mass density of acoustic metamaterial plate decorated with low frequency resonant pillars *J. Appl. Phys.* **116** 184504
- [97] Williams E G, Roux P, Rupin M and Kuperman W 2015 Theory of multiresonant metamaterials for a 0 Lamb waves *Phys. Rev. B* **91** 104307
- [98] Assouar B, Oudich M and Zhou X 2016 Acoustic metamaterials for sound mitigation *C. R. Phys.* **17** 524–32
- [99] Yan Z Y and Wu J H 2017 Ultra-low-frequency broadband of a new-type acoustic metamaterial beams with stiffness array *J. Phys. D: Appl. Phys.* **50** 355104
- [100] Jin Y, Bonello B, Moiseyenko R P, Pennec Y, Boyko O and Djafari-Rouhani B 2017 Pillar-type acoustic metasurface *Phys. Rev. B* **96** 104311
- [101] Jin Y, El Boudouti E H, Pennec Y and Djafari-Rouhani B 2017 Tunable Fano resonances of Lamb modes in a pillared metasurface *J. Phys. D: Appl. Phys.* **50** 425304
- [102] Goffaux C, Sánchez-Dehesa J, Yeyati A L, Lambin P, Khelif A, Vasseur J O and Djafari-Rouhani B 2002 Evidence of Fano-like interference phenomena in locally resonant materials *Phys. Rev. Lett.* **88** 225502
- [103] Anguiano S *et al* 2017 Micropillar resonators for optomechanics in the extremely high 19–95 GHz frequency range *Phys. Rev. Lett.* **118** 263901
- [104] Oudich M, Djafari-Rouhani B, Bonello B, Pennec Y and Sarry F 2017 Phononic crystal made of multilayered ridges on a substrate for Rayleigh waves manipulation *Crystals* **7** 372
- [105] Oudich M, Djafari-Rouhani B, Bonello B, Pennec Y, Hemaïdia S, Sarry F and Beyssen D 2018 Rayleigh waves in phononic crystal made of multilayered pillars: confined modes, Fano resonances, and acoustically induced transparency *Phys. Rev. Appl.* **9** 034013
- [106] Wu T T, Chun-Shao L and Ting-Wei L 2013 Band gap and local resonances of Love waves in a piezoelectric substrate coated with phononic guiding layer *2013 IEEE Int. Ultrasonics Symp. (IUS)* 2133–5
- [107] Bonhomme J, Oudich M, Djafari-Rouhani B, Sarry F, Pennec Y, Bonello B, Beyssen D and Charette P G 2019 Love waves dispersion by phononic pillars for nano-particle mass sensing *Appl. Phys. Lett.* **114** 013501
- [108] Kushwaha M S, Akjouj A, Djafari-Rouhani B, Dobrzynski L and Vasseur J O 1998 Acoustic spectral gaps and discrete transmission in slender tubes *Solid State Commun.* **106** 659–63
- [109] Al-Wahsh H, Akjouj A, Djafari-Rouhani B, Vasseur J O, Dobrzynski L and Deymier P A 1999 Large magnonic band gaps and defect modes in one-dimensional comblike structures *Phys. Rev. B* **59** 8709–19
- [110] Djafari-Rouhani B, Vasseur J O, Akjouj A, Dobrzynski L, Kushwaha M S, Deymier P A and Zemmouri J 1998 Giant stop bands and defect modes in one-dimensional waveguide with dangling side branches *Prog. Surf. Sci.* **59** 255–64
- [111] El Boudouti E H, Mrabti T, Al-Wahsh H, Djafari-Rouhani B, Akjouj A and Dobrzynski L 2008 Transmission gaps and Fano resonances in an acoustic waveguide: analytical model *J. Phys.: Condens. Matter* **20** 255212
- [112] Jin Y, Pennec Y and Djafari-Rouhani B 2018 Acoustic analogue of electromagnetically induced transparency and Autler–Townes splitting in pillared metasurfaces *J. Phys. D: Appl. Phys.* **51** 494004
- [113] Hein S, Koch W and Nannen L 2012 Trapped modes and Fano resonances in two-dimensional acoustical duct-cavity systems *J. Fluid Mech.* **692** 257–87
- [114] Dobrzynski L, Djafari-Rouhani B, Akjouj A, Vasseur J O and Zemmouri J 1999 Resonant tunnelling of acoustic waves between two slender tubes *Europhys. Lett.* **46** 467
- [115] Ash J and Robertson W M 2005 Acoustic band gap measurements in waveguides with periodic resonant structures *Z. Kristallogr.-Cryst. Mater.* **220** 824–8
- [116] Lee K J B, Jung M K and Lee S H 2012 Highly tunable acoustic metamaterials based on a resonant tubular array *Phys. Rev. B* **86** 184302
- [117] Wang Y-F, Laude V and Wang Y-S 2014 Coupling of evanescent and propagating guided modes in locally resonant phononic crystals *J. Phys. D: Appl. Phys.* **47** 475502
- [118] Hladky-Hennion A-C, Vasseur J, Djafari-Rouhani B and de Billy M 2008 Sonic band gaps in one-dimensional phononic crystals with a symmetric stub *Phys. Rev. B* **77** 104304
- [119] Hladky-Hennion A-C, Granger C, Vasseur J and de Billy M 2010 Propagation of elastic waves in one-dimensional periodic stubbed waveguides *Phys. Rev. B* **82** 104307
- [120] Yao Y, Hou Z, Wu F and Fu X 2010 The band structure and propagation property of Lamb waves in stubbed waveguides *Wave Motion* **47** 343–9
- [121] Yao Y, Hou Z, Wu F and Zhang X 2011 Low-frequency band gaps in one-dimensional thin phononic crystal plate with periodic stubbed surface *Physica B* **406** 2249–53
- [122] Wang X F, Kushwaha M S and Vasilopoulos P 2001 Tunability of acoustic spectral gaps and transmission in periodically stubbed waveguides *Phys. Rev. B* **65** 035107
- [123] Li W and Chen K 2006 Phonon heat transport through periodically stubbed waveguides *Phys. Lett. A* **357** 378–83
- [124] Xie Z-X, Liu J-Z, Yu X, Wang H-B, Deng Y-X, Li K-M and Zhang Y 2015 Tunability of acoustic phonon transmission and thermal conductance in three dimensional quasi-periodically stubbed waveguides *J. Appl. Phys.* **117** 114308
- [125] Djafari-Rouhani B, Pennec Y and Larabi H 2010 Band structure and phonon transport in a phononic crystal made of a periodic array of dots on a membrane *IUTAM Symposium on Recent Advances of Acoustic Waves in Solids, IUTAM Bookseries* (Berlin: Springer) pp 127–38
- [126] Addouche M, Al-Lethawe M A, Choujaa A and Khelif A 2014 Superlensing effect for surface acoustic waves in a pillar-based phononic crystal with negative refractive index *Appl. Phys. Lett.* **105** 023501
- [127] Yan X, Zhu R, Huang G L and Yuan F G 2013 Focusing flexural Lamb waves by designing elastic metamaterials bonded on a plate *Proc. SPIE* **8695** Health Monitoring of Structural and Biological Systems 2013, 86952P (17 April 2013) SPIE2013
- [128] Al-Lethawe M A, Addouche M, Khelif A and Guenneau S 2012 All-angle negative refraction for surface acoustic waves in pillar-based two-dimensional phononic structures *New J. Phys.* **14** 123030
- [129] Rupin M, Catheline S and Roux P 2015 Super-resolution experiments on Lamb waves using a single emitter *Appl. Phys. Lett.* **106** 024103
- [130] Pennec Y, Djafari-Rouhani B, Larabi H, Akjouj A, Gillet J, Vasseur J and Thabet G 2009 Phonon transport and waveguiding in a phononic crystal made up of cylindrical dots on a thin homogeneous plate *Phys. Rev. B* **80** 144302
- [131] Wu T-C, Wu T-T and Hsu J-C 2009 Waveguiding and frequency selection of Lamb waves in a plate with a periodic stubbed surface *Phys. Rev. B* **79** 104306
- [132] Oudich M, Assouar M B and Hou Z 2010 Propagation of acoustic waves and waveguiding in a two-dimensional locally resonant phononic crystal plate *Appl. Phys. Lett.* **97** 193503

- [133] Hsu J-C, Wu T-T and Hsu H-S 2013 Measurement of frequency gaps and waveguiding in phononic plates with periodic stepped cylinders using pulsed laser generated ultrasound *J. Appl. Phys.* **113** 083511
- [134] Addouche M, Al-Lethawe M A, Elayouch A and Khelif A 2014 Subwavelength waveguiding of surface phonons in pillars-based phononic crystal *AIP Adv.* **4** 124303
- [135] Shelke A, Banerjee S, Zhenhua T and Yu L 2015 Spiral Lamb waveguide for spatial filtration of frequencies in a confined space *Exp. Mech.* **55** 1199–209
- [136] Jiang P, Wang X-P, Chen T-N and Zhu J 2015 Band gap and defect state engineering in a multi-stub phononic crystal plate *J. Appl. Phys.* **117** 154301
- [137] Yin J, Zhang S, Zhang H W and Chen B S 2015 Band structure and transmission characteristics of complex phononic crystals by multi-level substructure scheme *Int. J. Mod. Phys. B* **29** 1550013
- [138] Dehghanasiri R, Pourabolghasem R, Eftekhar A A and Adibi A 2016 Integrated phononic crystal resonators based on adiabatically-terminated phononic crystal waveguides *AIP Adv.* **6** 121603
- [139] Feng D, Jiang W, Xu D, Xiong B and Wang Y 2017 Micro-silicon phononic crystal with locally resonant theory *Appl. Phys. Lett.* **110** 171902
- [140] Pourabolghasem R, Dehghanasiri R, Eftekhar A A and Adibi A 2018 Waveguiding effect in the gigahertz frequency range in pillar-based phononic-crystal slabs *Phys. Rev. Appl.* **9** 014013
- [141] Yuan W T, Zhao J F, Bonello B, Djafari-Rouhani B, Zhang X Q, Pan Y D and Zhong Z 2018 Compact waveguide and guided beam pattern based on the whispering-gallery mode of a hollow pillar in a phononic crystal plate *Phys. Rev. Appl.* **10** 034010
- [142] Assouar B, Senesi M, Oudich M, Ruzzene M and Hou Z 2012 Broadband plate-type acoustic metamaterial for low-frequency sound attenuation *Appl. Phys. Lett.* **101** 173505
- [143] Oudich M, Zhou X and Badreddine Assouar M 2014 General analytical approach for sound transmission loss analysis through a thick metamaterial plate *J. Appl. Phys.* **116** 193509
- [144] Pourabolghasem R, Mohammadi S, Eftekhar A A, Khelif A and Adibi A 2014 Experimental evidence of high-frequency complete elastic bandgap in pillar-based phononic slabs *Appl. Phys. Lett.* **105** 231908
- [145] Gliozzi A S, Miniaci M, Chiappone A, Bergamini A, Morin B and Descrovi E 2020 Tunable photo-responsive elastic metamaterials *Nat. Commun.* **11** 2576
- [146] Colombi A, Roux P, Guenneau S, Gueguen P and Craster R V 2016 Forests as a natural seismic metamaterial: Rayleigh wave bandgaps induced by local resonances *Sci. Rep.* **6** 19238
- [147] Colquitt D J, Colombi A, Craster R V, Roux P and Guenneau S R L 2017 Seismic metasurfaces: subwavelength resonators and Rayleigh wave interaction *J. Mech. Phys. Solids* **99** 379–93
- [148] Colombi A, Craster R V, Colquitt D, Achaoui Y, Guenneau S, Roux P and Rupin M 2017 Elastic wave control beyond band-gaps: shaping the flow of waves in plates and half-spaces with subwavelength resonant rods *Frontiers Mech. Eng.* **3** 10
- [149] Carrara M, Cacan M R, Toussaint J, Leamy M J, Ruzzene M and Erturk A 2013 Metamaterial-inspired structures and concepts for elastoacoustic wave energy harvesting *Smart Mater. Struct.* **22** 065004
- [150] Qi S, Oudich M, Li Y and Assouar B 2016 Acoustic energy harvesting based on a planar acoustic metamaterial *Appl. Phys. Lett.* **108** 263501
- [151] De Ponti J M, Colombi A, Ardito R, Braghin F, Corigliano A and Craster R V 2020 Graded elastic metasurface for enhanced energy harvesting *New J. Phys.* **22** 013013
- [152] Zhao J, Marchal R, Bonello B and Boyko O 2012 Efficient focalization of antisymmetric Lamb waves in gradient-index phononic crystal plates *Appl. Phys. Lett.* **101** 261905
- [153] Jin Y, Torrent D, Pennec Y, Pan Y and Djafari-Rouhani B 2015 Simultaneous control of the  $S_0$  and  $A_0$  Lamb modes by graded phononic crystal plates *J. Appl. Phys.* **117** 244904
- [154] Jin Y, Torrent D, Pennec Y, Pan Y and Djafari-Rouhani B 2016 Gradient index devices for the full control of elastic waves in plates *Sci. Rep.* **6** 24437
- [155] Jin Y, Torrent D, Pennec Y, Lévêque G, Pan Y and Djafari-Rouhani B 2016 Multimodal and omnidirectional beam splitters for Lamb modes in elastic plates *AIP Adv.* **6** 121602
- [156] Jin Y, Torrent D and Djafari-Rouhani B 2017 Invisible omnidirectional lens for flexural waves in thin elastic plates *J. Phys. D: Appl. Phys.* **50** 225301
- [157] Jin Y, Djafari-Rouhani B and Torrent D 2019 Gradient index phononic crystals and metamaterials *Nanophotonics* **8** 685
- [158] Zhao J, Bonello B and Boyko O 2016 Focusing of the lowest-order antisymmetric Lamb mode behind a gradient-index acoustic metalens with local resonators *Phys. Rev. B* **93** 174306
- [159] Colombi A 2016 Resonant metalenses for flexural waves in plates *J. Acoust. Soc. Am.* **140** EL423–8
- [160] Colombi A, Colquitt D, Roux P, Guenneau S and Craster R V 2016 A seismic metamaterial: the resonant metawedge *Sci. Rep.* **6** 27717
- [161] Guo Y, Hettich M and Dekorsy T 2017 Guiding of elastic waves in a two-dimensional graded phononic crystal plate *New J. Phys.* **19** 013029
- [162] Torrent D, Mayou D and Sánchez-Dehesa J 2013 Elastic analog of graphene: Dirac cones and edge states for flexural waves in thin plates *Phys. Rev. B* **87** 115143
- [163] Pal R K and Ruzzene M 2017 Edge waves in plates with resonators: an elastic analogue of the quantum valley Hall effect *New J. Phys.* **19** 025001
- [164] Chaunsali R, Chen C-W and Yang J 2018 Subwavelength and directional control of flexural waves in zone-folding induced topological plates *Phys. Rev. B* **97** 054307
- [165] Yu S-Y *et al* 2016 Surface phononic graphene *Nat. Mater.* **15** 1243–7
- [166] Vila J, Pal R K and Ruzzene M 2017 Observation of topological valley modes in an elastic hexagonal lattice *Phys. Rev. B* **96** 134307
- [167] Chen J-J, Huo S-Y, Geng Z-G, Huang H-B and Zhu X-F 2017 Topological valley transport of plate-mode waves in a homogenous thin plate with periodic stubbed surface *AIP Adv.* **7** 115215
- [168] Jin Y, Torrent D and Djafari-Rouhani B 2018 Robustness of conventional and topologically protected edge states in phononic crystal plates *Phys. Rev. B* **98** 054307
- [169] Yan M, Lu J, Li F, Deng W, Huang X, Ma J and Liu Z 2018 On-chip valley topological materials for elastic wave manipulation *Nat. Mater.* **17** 993–8
- [170] Fan H, Xia B, Tong L, Zheng S and Yu D 2019 Elastic higher-order topological insulator with topologically protected corner states *Phys. Rev. Lett.* **122** 204301
- [171] Wang Z, Wei Q, Xu H-Y and Wu D-J 2020 A higher-order topological insulator with wide bandgaps in Lamb-wave systems *J. Appl. Phys.* **127** 075105
- [172] Li Y, Liang B, Gu Z-m, Zou X-y and Cheng J-c 2013 Reflected wavefront manipulation based on ultrathin planar acoustic metasurfaces *Sci. Rep.* **3** 2546
- [173] Tang K, Qiu C, Ke M, Lu J, Ye Y and Liu Z 2014 Anomalous refraction of airborne sound through ultrathin metasurfaces *Sci. Rep.* **4** 6517

- [174] Xie Y, Wang W, Chen H, Konneker A, Popa B-I and Cummer S A 2014 Wavefront modulation and subwavelength diffractive acoustics with an acoustic metasurface *Nat. Commun.* **5** 5553
- [175] Liang B, Cheng J-C and Qiu C-W 2018 Wavefront manipulation by acoustic metasurfaces: from physics and applications *Nanophotonics* **7** 1191
- [176] Assouar B, Liang B, Wu Y, Li Y, Cheng J-C and Jing Y 2018 Acoustic metasurfaces *Nat. Rev. Mater.* **3** 460–72
- [177] Jin Y, Kumar R, Poncelet O, Mondain-Monval O and Brunet T 2019 Flat acoustics with soft gradient-index metasurfaces *Nat. Commun.* **10** 143
- [178] Jin Y, Fang X, Li Y and Torrent D 2019 Engineered diffraction gratings for acoustic cloaking *Phys. Rev. Appl.* **11** 011004
- [179] Yu N, Genevet P, Kats M A, Aieta F, Tetienne J-P, Capasso F and Gaburro Z 2011 Light propagation with phase discontinuities: generalized laws of reflection and refraction *Science* **334** 333–7
- [180] Cheng Y, Jin Y, Zhou Y, Hao T and Li Y 2019 Distinction of acoustically induced transparency and Autler–Townes splitting by Helmholtz resonators *Phys. Rev. Appl.* **12** 044025
- [181] Graczykowski B, Mielcarek S, Trzaskowska A, Sarkar J, Hakonen P and Mroz B 2012 Tuning of a hypersonic surface phononic band gap using a nanoscale two-dimensional lattice of pillars *Phys. Rev. B* **86** 085426
- [182] Mielcarek S, Trzaskowska A, Graczykowski B and Sarkar J 2012 Hypersonic surface waves in 2D titanium nanostructure on silicon *Phys. Status Solidi RRL* **6** 175–7
- [183] Trzaskowska A, Mielcarek S and Sarkar J 2013 Band gap in hypersonic surface phononic lattice of nickel pillars *J. Appl. Phys.* **114** 134304
- [184] Graczykowski B, Sledzinska M, Alzina F, Gomis-Bresco J, Reparaz J, Wagner M and Torres C S 2015 Phonon dispersion in hypersonic two-dimensional phononic crystal membranes *Phys. Rev. B* **91** 075414
- [185] Yudistira D, Boes A, Graczykowski B, Alzina F, Yeo L, Torres C S and Mitchell A 2016 Nanoscale pillar hypersonic surface phononic crystals *Phys. Rev. B* **94** 094304
- [186] Davis B L and Hussein M I 2014 Nanophononic metamaterial: thermal conductivity reduction by local resonance *Phys. Rev. Lett.* **112** 055505
- [187] Hussein M I and Davis B L 2016 Nanophononic metamaterials, *US Patent No.* 9417465 B2
- [188] Honarvar H and Hussein M I 2016 Spectral energy analysis of locally resonant nanophononic metamaterials by molecular simulations *Phys. Rev. B* **93** 081412
- [189] Honarvar H, Yang L and Hussein M I 2016 Thermal transport size effects in silicon membranes featuring nanopillars as local resonators *Appl. Phys. Lett.* **108** 263101
- [190] Honarvar H and Hussein M I 2018 Two orders of magnitude reduction in silicon membrane thermal conductivity by resonance hybridizations *Phys. Rev. B* **97** 195413
- [191] Hussein M I and Honarvar H 2018 Resonant thermal transport in nanophononic metamaterials *Handbook of Materials Modeling: Applications: Current and Emerging Materials* (New York: Springer) pp 1–21
- [192] Anufriev R, Yanagisawa R and Nomura M 2017 Aluminium nanopillars reduce thermal conductivity of silicon nanobeams *Nanoscale* **9** 15083–8
- [193] Xiao Y, Mace B R, Wen J and Wen X 2011 Formation and coupling of band gaps in a locally resonant elastic system comprising a string with attached resonators *Phys. Lett. A* **375** 1485–91
- [194] Rughunanan L, Mace B, Sorokin V and du Toit D 2020 On the behaviour of infinite, periodic, mono-coupled waveguides using a transmission coefficient phase method *Mech. Syst. Signal Process.* **135** 106409
- [195] Liu L and Hussein M I 2011 Wave motion in periodic flexural beams and characterization of the transition between Bragg scattering and local resonance *J. Appl. Mech.* **79** 011003
- [196] Wang W, Bonello B, Djafari-Rouhani B, Pennec Y and Zhao J 2018 Double-negative pillared elastic metamaterial *Phys. Rev. Appl.* **10** 064011
- [197] Rayleigh L 1910 CXII. The problem of the whispering gallery *London, Edinburgh Dublin Phil. Mag. J. Sci.* **20** 1001–4
- [198] Foreman M R, Swaim J D and Vollmer F 2015 Whispering gallery mode sensors *Adv. Opt. Photonics* **7** 168–240
- [199] Li F, Xuan M, Wu Y and Bastien F 2013 Acoustic whispering gallery mode coupling with Lamb waves in liquid *Sensors Actuators A* **189** 335–8
- [200] Peng B, Özdemir Ş K, Chen W, Nori F and Yang L 2014 What is and what is not electromagnetically induced transparency in whispering-gallery microcavities *Nat. Commun.* **5** 5082
- [201] Gomis-Bresco J *et al* 2014 A one-dimensional optomechanical crystal with a complete phononic band gap *Nat. Commun.* **5** 4452
- [202] Mrabti A, Lévêque G, Akjouj A, Pennec Y, Djafari-Rouhani B, Nicolas R, Maurer T and Adam P-M 2016 Elastoplasmonic interaction in metal–insulator–metal localized surface plasmon systems *Phys. Rev. B* **94** 075405
- [203] Noual A, Akiki R, Pennec Y, El Boudouti E H and Djafari-Rouhani B 2020 Surface acoustic waves-localized plasmon interaction in pillared phononic crystals *Phys. Rev. Appl.* **13** 024077
- [204] Johnson S G, Fan S, Villeneuve P R, Joannopoulos J D and Kolodziejski L A 1999 Guided modes in photonic crystal slabs *Phys. Rev. B* **60** 5751
- [205] Schuller J A, Barnard E S, Cai W, Jun Y C, White J S and Brongersma M L 2010 Plasmonics for extreme light concentration and manipulation *Nat. Mater.* **9** 193–204
- [206] Alabastri A, Malerba M, Calandrini E, Manjavacas A, De Angelis F, Toma A and Proietti Zaccaria R 2017 Controlling the heat dissipation in temperature-matched plasmonic nanostructures *Nano Lett.* **17** 5472–80
- [207] Soavi G, Tempra I, Pantano M F, Cattoni A, Collin S, Biagioni P, Pugno N M and Cerullo G 2016 Ultrasensitive characterization of mechanical oscillations and plasmon energy shift in gold nanorods *ACS Nano* **10** 2251–8
- [208] Girard A, Lermé J, Gehan H, Mermet A, Bonnet C, Cottancin E, Crut A and Margueritat J 2019 Inelastic light scattering by multiple vibrational modes in individual gold nanodimers *J. Phys. Chem. C* **123** 14834–41
- [209] Yi C *et al* 2017 Vibrational coupling in plasmonic molecules *Proc. Natl Acad. Sci. USA* **114** 11621
- [210] Sigmund O and Søndergaard Jensen J 2003 Systematic design of phononic band-gap materials and structures by topology optimization *Phil. Trans. R. Soc. A* **361** 1001–19
- [211] Hussein M I, Hamza K, Hulbert G M, Scott R A and Saitou K 2006 Multiobjective evolutionary optimization of periodic layered materials for desired wave dispersion characteristics *Struct. Multidiscip. Optim.* **31** 60–75
- [212] Bilal O R and Hussein M I 2011 Ultrawide phononic band gap for combined in-plane and out-of-plane waves *Phys. Rev. E* **84** 065701
- [213] Li Y, Chen T, Wang X, Xi Y and Liang Q 2015 Enlargement of locally resonant sonic band gap by using composite plate-type acoustic metamaterial *Phys. Lett. A* **379** 412–6
- [214] Wang W, Bonello B, Djafari-Rouhani B, Pennec Y and Zhao J 2020 Elastic stubbed metamaterial plate with torsional resonances *Ultrasonics* **106** 106142
- [215] Sukhovich A, Jing L and Page J H 2008 Negative refraction and focusing of ultrasound in two-dimensional phononic crystals *Phys. Rev. B* **77** 014301
- [216] Ke M, Liu Z, Qiu C, Wang W, Shi J, Wen W and Sheng P 2005 Negative-refraction imaging with two-dimensional phononic crystals *Phys. Rev. B* **72** 064306

- [217] He Z, Heng Y, Peng S, Ding Y, Ke M and Liu Z 2009 Acoustic collimating beams by negative refraction in two-dimensional phononic crystal *J. Appl. Phys.* **105** 116105
- [218] He Z, Li X, Mei J and Liu Z 2009 Improving imaging resolution of a phononic crystal lens by employing acoustic surface waves *J. Appl. Phys.* **106** 026105
- [219] Pierre J, Boyko O, Belliard L, Vasseur J O and Bonello B 2010 Negative refraction of zero order flexural Lamb waves through a two-dimensional phononic crystal *Appl. Phys. Lett.* **97** 121919
- [220] Veres I A, Berer T, Matsuda O and Burgholzer P 2012 Focusing and subwavelength imaging of surface acoustic waves in a solid-air phononic crystal *J. Appl. Phys.* **112** 053504
- [221] Christensen J and de Abajo F J G 2012 Anisotropic metamaterials for full control of acoustic waves *Phys. Rev. Lett.* **108** 124301
- [222] Notomi M 2000 Theory of light propagation in strongly modulated photonic crystals: refraction like behavior in the vicinity of the photonic band gap *Phys. Rev. B* **62** 10696
- [223] Lin S-C S, Huang T J, Sun J-H and Wu T-T 2009 Gradient-index phononic crystals *Phys. Rev. B* **79** 094302
- [224] Deng K, Ding Y, He Z, Zhao H, Shi J and Liu Z 2009 Graded negative index lens with designable focal length by phononic crystal *J. Phys. D: Appl. Phys.* **42** 185505
- [225] Climente A, Torrent D and Sánchez-Dehesa J 2010 Sound focusing by gradient index sonic lenses *Appl. Phys. Lett.* **97** 104103
- [226] Martin T P, Nicholas M, Orris G J, Cai L-W, Torrent D and Sánchez-Dehesa J 2010 Sonic gradient index lens for aqueous applications *Appl. Phys. Lett.* **97** 113503
- [227] Peng S, He Z, Jia H, Zhang A, Qiu C, Ke M and Liu Z 2010 Acoustic far-field focusing effect for two-dimensional graded negative refractive-index sonic crystals *Appl. Phys. Lett.* **96** 263502
- [228] Wu T-T, Chen Y-T, Sun J-H, Lin S-C S and Huang T J 2011 Focusing of the lowest antisymmetric Lamb wave in a gradient-index phononic crystal plate *Appl. Phys. Lett.* **98** 171911
- [229] Zigoneanu L, Popa B-I and Cummer S A 2011 Design and measurements of a broadband two-dimensional acoustic lens *Phys. Rev. B* **84** 024305
- [230] Lin S-C S, Tittmann B R and Huang T J 2012 Design of acoustic beam aperture modifier using gradient-index phononic crystals *J. Appl. Phys.* **111** 123510
- [231] Li Y, Liang B, Tao X, Zhu X-F, Zou X-Y and Cheng J-C 2012 Acoustic focusing by coiling up space *Appl. Phys. Lett.* **101** 233508
- [232] Chang T M, Dupont G, Enoch S and Guenneau S 2012 Enhanced control of light and sound trajectories with three-dimensional gradient index lenses *New J. Phys.* **14** 035011
- [233] Yan X, Zhu R, Huang G and Yuan F-G 2013 Focusing guided waves using surface bonded elastic metamaterials *Appl. Phys. Lett.* **103** 121901
- [234] Ye Y, Ke M, Li Y, Wang T and Liu Z 2013 Focusing of spoof surface-acoustic-waves by a gradient-index structure *J. Appl. Phys.* **114** 154504
- [235] Yuan B-G, Tian Y, Cheng Y and Liu X-J 2016 An acoustic Maxwell's fish-eye lens based on gradient-index metamaterials *Chin. Phys. B* **25** 104301
- [236] Kurt H and Citrin D S 2007 Graded index photonic crystals *Opt. Express* **15** 1240–53
- [237] Gao H, Zhang B, Johnson S G and Barbastathis G 2012 Design of thin-film photonic metamaterial Luneburg lens using analytical approach *Opt. Express* **20** 1617–28
- [238] Do K-V, Le Roux X, Marris-Morini D, Vivien L and Cassan E 2012 Experimental demonstration of light bending at optical frequencies using a non-homogenizable graded photonic crystal *Opt. Express* **20** 4776–83
- [239] Climente A, Torrent D and Sánchez-Dehesa J 2014 Gradient index lenses for flexural waves based on thickness variations *Appl. Phys. Lett.* **105** 064101
- [240] Ma C, Escobar M A and Liu Z 2011 Extraordinary light focusing and Fourier transform properties of gradient-index metalenses *Phys. Rev. B* **84** 195142
- [241] Torrent D, Pennec Y and Djafari-Rouhani B 2014 Effective medium theory for elastic metamaterials in thin elastic plates *Phys. Rev. B* **90** 104110
- [242] Li J, Fok L, Yin X, Bartal G and Zhang X 2009 Experimental demonstration of an acoustic magnifying hyperlens *Nat. Mater.* **8** 931
- [243] Yao S, Zhou X and Hu G 2010 Investigation of the negative-mass behaviors occurring below a cut-off frequency *New J. Phys.* **12** 103025
- [244] Zhu J, Christensen J, Jung J, Martin-Moreno L, Yin X, Fok L, Zhang X and Garcia-Vidal F J 2011 A holey-structured metamaterial for acoustic deep-subwavelength imaging *Nat. Phys.* **7** 52
- [245] Lu D and Liu Z 2012 Hyperlenses and metalenses for far-field super-resolution imaging *Nat. Commun.* **3** 1205
- [246] Zhu R, Liu X, Huang G, Huang H-H and Sun C 2012 Microstructural design and experimental validation of elastic metamaterial plates with anisotropic mass density *Phys. Rev. B* **86** 144307
- [247] Lemoult F, Kaina N, Fink M and Lerosey G 2013 Wave propagation control at the deep subwavelength scale in metamaterials *Nat. Phys.* **9** 55
- [248] Centeno E, Cassagne D and Albert J-P 2006 Mirage and super-bending effect in two-dimensional graded photonic crystals *Phys. Rev. B* **73** 235119
- [249] Cassan E, Do K-V, Caer C, Marris-Morini D and Vivien L 2011 Short-wavelength light propagation in graded photonic crystals *J. Lightwave Technol.* **29** 1937–43
- [250] Halevi P, Krokhin A A and Arriaga J 1999 Photonic crystal optics and homogenization of 2D periodic composites *Phys. Rev. Lett.* **82** 719
- [251] Zhao J, Bonello B, Marchal R and Boyko O 2014 Beam path and focusing of flexural Lamb waves within phononic crystal-based acoustic lenses *New J. Phys.* **16** 063031
- [252] Luo C, Johnson S G, Joannopoulos J and Pendry J 2003 Sub-wavelength imaging in photonic crystals *Phys. Rev. B* **68** 045115
- [253] Zhu H, Walsh T F and Semperlotti F 2018 Total-internal-reflection elastic metasurfaces: design and application to structural vibration isolation *Appl. Phys. Lett.* **113** 221903
- [254] Chen Y, Li X, Nassar H, Hu G and Huang G 2018 A programmable metasurface for real time control of broadband elastic rays *Smart Mater. Struct.* **27** 115011
- [255] Rong J, Ye W, Zhang S and Liu Y 2020 Frequency-coded passive multifunctional elastic metasurfaces *Adv. Funct. Mater.* **30** 2005285
- [256] Jin Y 2017 Design of acoustic artificial structured materials: piezoelectric superlattice, gradient index lens, pillar based phononic crystal plate, *PhD Thesis* University of Lille 1, France
- [257] Wang W, Bonello B, Djafari-Rouhani B, Fang X, Pennec Y, Zhao J and Jin Y 2020 Active control of the transmission of Lamb waves through an elastic metamaterial *J. Appl. Phys.* **128** 065107
- [258] Jin Y, Wang W, Khelif A, Djafari-Rouhani B 2021 Elastic metasurface for deep and robust subwavelength focusing and imaging *Phys. Rev. Appl.* **15** 024005
- [259] Torrent D 2018 Acoustic anomalous reflectors based on diffraction grating engineering *Phys. Rev. B* **98** 060101

- [260] Packo P, Norris A N and Torrent D 2019 Inverse grating problem: efficient design of anomalous flexural wave reflectors and refractors *Phys. Rev. Appl.* **11** 014023
- [261] Klitzing K v, Dorda G and Pepper M 1980 New method for high-accuracy determination of the fine-structure constant based on quantized Hall resistance *Phys. Rev. Lett.* **45** 494–7
- [262] Tsui D C, Stormer H L and Gossard A C 1982 Two-dimensional magneto transport in the extreme quantum limit *Phys. Rev. Lett.* **48** 1559–62
- [263] Laughlin R B 1983 Anomalous quantum Hall effect: an incompressible quantum fluid with fractionally charged excitations *Phys. Rev. Lett.* **50** 1395–8
- [264] Kosterlitz J M and Thouless D J 1972 Long range order and metastability in two dimensional solids and superfluids. (Application of dislocation theory) *J. Phys. C: Solid State Phys.* **5** L124–6
- [265] Kosterlitz J M and Thouless D J 1973 Ordering, metastability and phase transitions in two-dimensional systems *J. Phys. C: Solid State Phys.* **6** 1181–203
- [266] Thouless D J, Kohmoto M, Nightingale M P and den Nijs M 1982 Quantized Hall conductance in a two-dimensional periodic potential *Phys. Rev. Lett.* **49** 405–8
- [267] Wang P, Lu L and Bertoldi K 2015 Topological phononic crystals with one-way elastic edge waves *Phys. Rev. Lett.* **115** 104302
- [268] Zhang X, Xiao M, Cheng Y, Lu M-H and Christensen J 2018 Topological sound *Commun. Phys.* **1** 97
- [269] Ma G, Xiao M and Chan C 2019 Topological phases in acoustic and mechanical systems *Nat. Rev. Phys.* **1** 281
- [270] Nassar H, Yousefzadeh B, Fleury R, Ruzzene M, Alù A, Daraio C, Norris A N, Huang G and Haberman M R 2020 Nonreciprocity in acoustic and elastic materials *Nat. Rev. Mater.* **5** 667–85
- [271] Deymier P and Runge K 2017 *Sound Topology, Duality, Coherence and Wave-Mixing* (Berlin: Springer)
- [272] Xiao Y, Wen J and Wen X 2012 Flexural wave band gaps in locally resonant thin plates with periodically attached spring–mass resonators *J. Phys. D: Appl. Phys.* **45** 195401
- [273] Wang W, Jin Y, Wang W, Bonello B, Djafari-Rouhani B and Fleury R 2020 Robust Fano resonance in a topological mechanical beam *Phys. Rev. B* **101** 024101
- [274] Jin Y, Wang W and Djafari-Rouhani B 2020 Asymmetric topological state in an elastic beam based on symmetry principle *Int. J. Mech. Sci.* **186** 105897
- [275] Chaunsali R, Chen C-W and Yang J 2018 Experimental demonstration of topological waveguiding in elastic plates with local resonators *New J. Phys.* **20** 113036
- [276] Mousavi S H, Khanikaev A B and Wang Z 2015 Topologically protected elastic waves in phononic metamaterials *Nat. Commun.* **6** 8682
- [277] Miniaci M, Pal R, Morvan B and Ruzzene M 2018 Experimental observation of topologically protected helical edge modes in patterned elastic plates *Phys. Rev. X* **8** 031074
- [278] Chen C W, Lera N, Chaunsali R, Torrent D, Alvarez J V, Yang J, San-Jose P and Christensen J 2019 Mechanical analogue of a Majorana bound state *Adv. Mater.* **31** 1904386
- [279] Wang W, Bonello B, Djafari-Rouhani B and Pennec Y 2019 Topological valley, pseudospin, and pseudospin-valley protected edge states in symmetric pillared phononic crystals *Phys. Rev. B* **100** 140101
- [280] Wang W, Bonello B, Djafari-Rouhani B and Pennec Y 2019 Polarization-dependent and valley-protected Lamb waves in asymmetric pillared phononic crystals *J. Phys. D: Appl. Phys.* **52** 505302
- [281] Jin Y, Wang W, Wen Z, Torrent D and Djafari-Rouhani B 2020 Topological states in twisted pillared phononic plates *Extreme Mech. Lett.* **39** 100777
- [282] Chen G 2000 Phonon heat conduction in nanostructures *Int. J. Therm. Sci.* **39** 471–80
- [283] Balandin A A 2005 Nanophononics: phonon engineering in nanostructures and nanodevices *J. Nanosci. Nanotech.* **5** 1015–22
- [284] Li N, Ren J, Wang L, Zhang G, Hänggi P and Li B 2012 Colloquium: phononics: manipulating heat flow with electronic analogs and beyond *Rev. Mod. Phys.* **84** 1045–66
- [285] Cahill D G *et al* 2014 Nanoscale thermal transport: II. 2003–2012 *Appl. Phys. Rev.* **1** 011305
- [286] Volz S *et al* 2016 Nanophononics: state of the art and perspectives *Eur. Phys. J. B* **89** 15
- [287] Li Y, Li W, Han T, Zheng X, Li J, Li B, Fan S and Qiu C-W 2020 Transforming heat transfer with thermal metamaterials and devices (arXiv:2008.07964)
- [288] Cleland A N, Schmidt D R and Yung C S 2001 Thermal conductance of nanostructured phononic crystals *Phys. Rev. B* **64** 172301
- [289] McGaughey A J H, Hussein M I, Landry E S, Kaviany M and Hulbert G M 2006 Phonon band structure and thermal transport correlation in a layered diatomic crystal *Phys. Rev. B* **74** 104304
- [290] Tang J, Wang H-T, Lee D H, Fardy M, Huo Z, Russell T P and Yang P 2010 Holey silicon as an efficient thermoelectric material *Nano Lett.* **10** 4279–83
- [291] Yu J-K, Mitrovic S, Tham D, Varghese J and Heath J R 2010 Reduction of thermal conductivity in phononic nanomesh structures *Nat. Nanotech.* **5** 718
- [292] He Y, Donadio D, Lee J-H, Grossman J C and Galli G 2011 Thermal transport in nanoporous silicon: interplay between disorder at mesoscopic and atomic scales *ACS Nano* **5** 1839–44
- [293] Maldovan M 2013 Narrow low-frequency spectrum and heat management by thermocrystals *Phys. Rev. Lett.* **110** 025902
- [294] Alaie S, Goettler D F, Su M, Leseman Z C, Reinke C M and El-Kady I 2015 Thermal transport in phononic crystals and the observation of coherent phonon scattering at room temperature *Nat. Commun.* **6** 7228
- [295] Lacatena V, Haras M, Robillard J-F, Monfray S, Skotnicki T and Dubois E 2015 Toward quantitative modeling of silicon phononic thermocrystals *Appl. Phys. Lett.* **106** 114104
- [296] Gillet J-N, Chalopin Y and Volz S 2009 Atomic-scale three-dimensional phononic crystals with a very low thermal conductivity to design crystalline thermoelectric devices *J. Heat Transfer* **131** 043206
- [297] Davis B L and Hussein M I 2011 Thermal characterization of nanoscale phononic crystals using supercell lattice dynamics *AIP Adv.* **1** 041701
- [298] Yang L, Yang N and Li B 2014 Extreme low thermal conductivity in nanoscale 3D Si phononic crystal with spherical pores *Nano Lett.* **14** 1734–8
- [299] Ashcroft N W and Mermin N D 1976 *Solid State Physics* (New York: Holt, Rinehart and Winston)
- [300] Srivastava G P 1990 *The Physics of Phonons* (London: Taylor and Francis)
- [301] Jain A, Yu Y-J and McGaughey A J H 2013 Phonon transport in periodic silicon nanoporous films with feature sizes greater than 100 nm *Phys. Rev. B* **87** 195301
- [302] Wagner M R, Graczykowski B, Reparaz J S, El Sachat A, Sledzinska M, Alzina F and Sotomayor Torres C M 2016 Two-dimensional phononic crystals: disorder matters *Nano Lett.* **16** 5661–8
- [303] Chen G, Dresselhaus M S, Dresselhaus G, Fleurial J-P and Caillat T 2003 Recent developments in thermoelectric materials *Int. Mater. Rev.* **48** 45–66
- [304] Vineis C J, Shakouri A, Majumdar A and Kanatzidis M G 2010 Nanostructured thermoelectrics: big efficiency gains from small features *Adv. Mater.* **22** 3970–80
- [305] Rowe D M 2018 *Thermoelectrics Handbook: Macro to Nano* (Boca Raton, FL: CRC Press)

- [306] Hussein M I, Tsai C N and Honarvar H 2019 Thermal conductivity reduction in a nanophononic metamaterial versus a nanophononic crystal: a review and comparative analysis *Adv. Funct. Mater.* **30** 1906718
- [307] Liu Z, Chan C T and Sheng P 2002 Three-component elastic wave band-gap material *Phys. Rev. B* **65** 165116
- [308] Boukai A I, Bunimovich Y, Tahir-Kheli J, Yu J-K, Goddard W A III and Heath J R 2008 Silicon nanowires as efficient thermoelectric materials *Nature* **451** 168
- [309] Neogi S *et al* 2015 Tuning thermal transport in ultrathin silicon membranes by surface nanoscale engineering *ACS Nano* **9** 3820–8
- [310] Dresselhaus M S, Chen G, Tang M Y, Yang R G, Lee H, Wang D Z, Ren Z F, Fleurial J-P and Gogna P 2007 New directions for low-dimensional thermoelectric materials *Adv. Mater.* **19** 1043–53
- [311] Wei Z, Yang J, Bi K and Chen Y 2015 Phonon transport properties in pillared silicon film *J. Appl. Phys.* **118** 155103
- [312] Xiong S, Sääskilähti K, Kosevich Y A, Han H, Donadio D and Volz S 2016 Blocking phonon transport by structural resonances in alloy-based nanophononic metamaterials leads to ultralow thermal conductivity *Phys. Rev. Lett.* **117** 025503
- [313] Ma D, Arora A, Deng S, Xie G, Shiomi J and Yang N 2019 Quantifying phonon particle and wave transport in silicon nanophononic metamaterial with cross junction *Mater. Today Phys.* **8** 56–61
- [314] Zhang H, Sun B, Hu S, Wang H, Cheng Y, Xiong S, Volz S and Ni Y 2020 Novel phonon resonator based on surface screw thread for suppressing thermal transport of Si nanowires *Phys. Rev. B* **101** 205418
- [315] Ma D, Ding H, Meng H, Feng L, Wu Y, Shiomi J and Yang N 2016 Nano-cross-junction effect on phonon transport in silicon nanowire cages *Phys. Rev. B* **94** 165434
- [316] Zhu T, Swaminathan-Gopalan K, Cruse K J, Stephani K and Ertekin E 2018 Vibrational energy transport in hybrid ordered/disordered nanocomposites: hybridization and avoided crossings of localized and delocalized modes *Adv. Funct. Mater.* **28** 1706268
- [317] Hussein M I 2017 Phononic metamaterials comprising atomically disordered resonators, *US Patent No.* 10283689
- [318] Liu Y-Y, Zeng Y-J, Jia P-Z, Cao X-H, Jiang X and Chen K-Q 2018 An efficient mechanism for enhancing the thermoelectricity of nanoribbons by blocking phonon transport in 2D materials *J. Phys.: Condens. Matter* **30** 275701
- [319] Giri A and Hopkins P E 2018 Giant reduction and tunability of the thermal conductivity of carbon nanotubes through low-frequency resonant modes *Phys. Rev. B* **98** 045421
- [320] Ma D, Wan X and Yang N 2018 Unexpected thermal conductivity enhancement in pillared graphene nanoribbon with isotopic resonance *Phys. Rev. B* **98** 245420
- [321] Giri A and Hopkins P E 2019 Resonant phonon modes in fullerene functionalized graphene lead to large tunability of thermal conductivity without impacting the mechanical properties *J. Appl. Phys.* **125** 205102
- [322] Iskandar A, Gwiazda A, Huang Y, Kazan M, Bruyant A, Tabbal M and Lerondel G 2016 Modification of the phonon spectrum of bulk Si through surface nanostructuring *J. Appl. Phys.* **120** 095106
- [323] Liu Y-Y, Zhou W-X, Tang L-M and Chen K-Q 2014 An important mechanism for thermal rectification in graded nanowires *Appl. Phys. Lett.* **105** 203111
- [324] Liu Y-Y, Zhou W-X and Chen K-Q 2015 Conjunction of standing wave and resonance in asymmetric nanowires: a mechanism for thermal rectification and remote energy accumulation *Sci. Rep.* **5** 17525
- [325] Yang X, Yu D, Cao B and To A C 2017 Ultrahigh thermal rectification in pillared graphene structure with carbon nanotube-graphene intramolecular junctions *ACS Appl. Mater. Interfaces* **9** 29–35
- [326] Chen X-K, Liu J, Xie Z-X, Zhang Y, Deng Y-X and Chen K-Q 2018 A local resonance mechanism for thermal rectification in pristine/branched graphene nanoribbon junctions *Appl. Phys. Lett.* **113** 121906
- [327] Li B, Tan K T and Christensen J 2017 Tailoring the thermal conductivity in nanophononic metamaterials *Phys. Rev. B* **95** 144305
- [328] Anufriev R and Nomura M 2018 Phonon and heat transport control using pillar-based phononic crystals *Sci. Technol. Adv. Mater.* **19** 863–70
- [329] Li B, Tan K T and Christensen J 2018 Heat conduction tuning by hyperbranched nanophononic metamaterials *J. Appl. Phys.* **123** 205105
- [330] Stillinger F H and Weber T A 1985 Computer simulation of local order in condensed phases of silicon *Phys. Rev. B* **31** 5262–71
- [331] Hussein M I 2009 Reduced Bloch mode expansion for periodic media band structure calculations *Proc. R. Soc. A* **465** 2825–48
- [332] Rabiner L R and Gold B 1975 *Theory and Application of Digital Signal Processing* vol 1975 (Englewood Cliffs, NJ: Prentice-Hall)
- [333] Thomas J A, Turney J E, Iutzi R M, Amon C H and McGaughey A J H 2010 Predicting phonon dispersion relations and lifetimes from the spectral energy density *Phys. Rev. B* **81** 081411
- [334] McGaughey A J H and Larkin J M 2014 Predicting phonon properties from equilibrium molecular dynamics simulations *Annu. Rev. Heat Transfer* **17** 49–87
- [335] Wang T, Madsen G K H and Hartmaier A 2014 Atomistic study of the influence of lattice defects on the thermal conductivity of silicon *Modelling Simul. Mater. Sci. Eng.* **22** 035011
- [336] Larkin J M, Turney J E, Massicotte A D, Amon C H and McGaughey A J H 2014 Comparison and evaluation of spectral energy methods for predicting phonon properties *J. Comput. Theor. Nanosci.* **11** 249–56
- [337] Feng T, Qiu B and Ruan X 2015 Anharmonicity and necessity of phonon eigenvectors in the phonon normal mode analysis *J. Appl. Phys.* **117** 195102
- [338] Esfarjani K, Chen G and Stokes H T 2011 Heat transport in silicon from first-principles calculations *Phys. Rev. B* **84** 085204
- [339] Helfand E 1960 Transport coefficients from dissipation in a canonical ensemble *Phys. Rev.* **119** 1–9
- [340] Zwanzig R 1965 Time-correlation functions and transport coefficients in statistical mechanics *Annu. Rev. Phys. Chem.* **16** 67–102
- [341] Ladd A J C, Moran B and Hoover W G 1986 Lattice thermal conductivity: a comparison of molecular dynamics and anharmonic lattice dynamics *Phys. Rev. B* **34** 5058
- [342] Plimpton S 1995 Fast parallel algorithms for short-range molecular dynamics *J. Comput. Phys.* **117** 1–19
- [343] Xiao Y, Wen J and Wen X 2012 Flexural wave band gaps in locally resonant thin plates with periodically attached spring–mass resonators *J. Phys. D: Appl. Phys.* **45** 195401
- [344] Hussein M I and Frazier M J 2013 Metadamping: an emergent phenomenon in dissipative metamaterials *J. Sound Vib.* **332** 4767–74
- [345] Bacquet C L, Al Ba'ba'aa H, Frazier M J, Nouh M and Hussein M I 2018 Metadamping: dissipation emergence in elastic metamaterials *Adv. Appl. Mech.* **51** 115–64

- [346] Frazier MJ and Hussein MI 2015 Viscous-to-viscoelastic transition in photonic crystal and metamaterial band structures *J. Acoust. Soc. Am.* **138** 3169–80
- [347] Bacquet C L and Hussein M I 2018 Dissipation engineering in metamaterials by localized structural dynamics (arXiv:1809.04509)
- [348] DePauw D, AlBa'ba'a H and Nouh M 2018 Metadamping and energy dissipation enhancement via hybrid photonic resonators *Extreme Mech. Lett.* **18** 36–44
- [349] Aladwani A and Nouh M 2020 Mechanics of metadamping in flexural dissipative metamaterials: analysis and design in frequency and time domains *Int. J. Mech. Sci.* **173** 105459
- [350] Aladwani A and Nouh M 2021 Strategic damping placement in viscoelastic bandgap structures: dissecting the metadamping phenomenon in multiresonator metamaterials *J. Appl. Mech.* **88** 021003
- [351] Lazarov B S and Jensen J S 2007 Low-frequency band gaps in chains with attached non-linear oscillators *Int. J. Non-Linear Mech.* **42** 1186–93
- [352] Khajehtourian R and Hussein M I 2014 Dispersion characteristics of a nonlinear elastic metamaterial *AIP Adv.* **4** 124308
- [353] Silva P B, Leamy M J, Geers M G D and Kouznetsova V G 2019 Emergent subharmonic band gaps in nonlinear locally resonant metamaterials induced by autoparametric resonance *Phys. Rev. E* **99** 063003
- [354] Hu G, Tang L, Das R, Gao S and Liu H 2017 Acoustic metamaterials with coupled local resonators for broadband vibration suppression *AIP Adv.* **7** 025211
- [355] Beli D, Arruda J R F and Ruzzene M 2018 Wave propagation in elastic metamaterial beams and plates with interconnected resonators *Int. J. Solids Struct.* **139–140** 105–20
- [356] Esmaeel G and Fazelzadeh S A 2019 Wave propagation in one-dimensional infinite acoustic metamaterials with long-range interactions *Acta Mech.* **230** 4453–61
- [357] Quan L and Alu A 2019 Hyperbolic sound propagation over nonlocal acoustic metasurfaces *Phys. Rev. Lett.* **123** 244303
- [358] Zhu H, Patnaik S, Walsh T, Jared B and Semperlotti F 2020 Nonlocal elastic metasurfaces: enabling broadband wave control via intentional nonlocality *Proc. Natl Acad. Sci. USA* **117** 26099–108
- [359] Rosa M I N and Ruzzene M 2020 Dynamics and topology of non-Hermitian elastic lattices with non-local feedback control interactions *New J. Phys.* **22** 053004
- [360] Scheibner C, Irvine W T M and Vitelli V 2020 Non-Hermitian band topology and skin modes in active elastic media *Phys. Rev. Lett.* **125** 118001
- [361] Rosa M I N, Mazzotti M and Ruzzene M 2021 Exceptional points and enhanced sensitivity in PT-symmetric continuous elastic media *J. Mech. Phys. Solids* **149** 104325
- [362] Christensen J, Willatzen M, Velasco V R and Lu M H 2016 Parity-time synthetic photonic media *Phys. Rev. Lett.* **116** 207601
- [363] Lin X, Rivenson Y, Yardimci N T, Veli M, Luo Y, Jarrahi M and Ozcan A 2018 All-optical machine learning using diffractive deep neural networks *Science* **361** 1004–8
- [364] Han J H *et al* 2018 Machine learning-based self-powered acoustic sensor for speaker recognition *Nano Energy* **53** 658–65
- [365] Ballard Z S, Shir D, Bhardwaj A, Bazargan S, Sathianathan S and Ozcan A 2017 Computational sensing using low-cost and mobile plasmonic readers designed by machine learning *ACS Nano* **11** 2266–74
- [366] Malkiel I, Mrejen M, Nagler A, Arieli U, Wolf L and Suchowski H 2018 Plasmonic nanostructure design and characterization via deep learning *Light Sci. Appl.* **7** 60
- [367] Ma W, Cheng F and Liu Y 2018 Deep-learning-enabled on-demand design of chiral metamaterials *ACS Nano* **12** 6326–34
- [368] Pennec Y, Jin Y and Djafari-Rouhani B 2019 Phononic and photonic crystals for sensing applications *Adv. Appl. Mech.* **52** 105–45
- [369] He L, Wen Z, Jin Y, Torrent D, Zhuang X and Rabczuk T 2021 Inverse design of topological metaplates for flexural waves with machine learning *Mater. Des.* **199** 109390
- [370] Hussein M I and El-Kady I 2011 Preface to special topic: Selected articles from Phononics 2011: The First International Conference on Phononic Crystals, Metamaterials and Optomechanics, 29 May–2 June 2011, Santa Fe, NM *AIP Adv.* **1** 041301
- [371] Hsu J C and Wu T T 2007 Lamb waves in binary locally resonant phononic plates with two-dimensional lattices *Appl. Phys. Lett.* **90** 201904
- [372] Nouh M, Aldraihem O and Baz A 2015 Wave propagation in metamaterial plates with periodic local resonances *J. Sound Vib.* **341** 53–73
- [373] Neogi S and Donadio D 2020 Anisotropic in-plane phonon transport in silicon membranes guided by nanoscale surface resonators *Phys. Rev. Appl.* **14** 024004



**Yabin Jin** currently is the Eastern Scholar Professor at Tongji University, China. He received two PhD degrees, from Tongji University, China and University of Lille, France in March 2017. He joined Tongji University in September 2018 after holding a postdoc position at the University of Bordeaux, France from April 2017 to August 2018. He leads a research group studying elastic wave-structure interactions, mechanical metamaterials with multifunctional integration, and machine learning based inverse design. He published about 30 papers as the first or corresponding author in well-known international journals including *Nature Communications*, *Physical Review B/Applied*, *Nanophotonics*, *Extreme Mechanics Letters*. He was an invited professor of the University of Lille in 2020, and was awarded Seal of Excellence by the European Commission (2018), Tongji Innovation Award (2018), Hundred Young Talents by Tongji University (2018), Pujiang Talent by Shanghai Government (2019), 1st Prize of Outstanding Young Scholar by the Shanghai Society of Theoretical and Applied Mechanics (2020).



**Yan Pennec** is a Professor at the University of Lille, France. He received a permanent position as an assistant professor in 1994 just after completing his PhD defense at the University of Le Mans, France. He is affiliated to the Institute of Electronic, Microelectronic and Nanotechnology (IEMN) where he conducts his research on simulation of wave propagations in phononic, photonic, and plasmonic nanostructures and their interactions through optomechanical and phoXonic devices. He was promoted to the rank of Full Professor at the University of Lille in 2014. He has participated in several national and European research projects as scientific partner and Work Package leader. He has published more than 120 papers in international refereed journals and about 10 review articles and book chapters. Since 2015, he leads the theory group EPHONI at IEMN.



**Bernard Bonello** received his PhD degree in Physics from Pierre and Marie Curie University, Paris, in 1989 and accreditation to direct researches (HDR) in 2000. Soon after he received his PhD degree, he joined the French Council for Scientific Research (CNRS) as research scientist to study elastic properties of micro and nanostructures. In 1992, he had a one year stay in Florence, Italy as an invited researcher at the European Laboratory for Nonlinear Spectroscopy. He was appointed senior research scientist at CNRS in 2010. Since 2003, he heads the research group for phononic crystals and elastic metamaterials at the Institut des NanoSciences de Paris. Between 2012 and 2017, he was Program Officer at the French Agency for Research (ANR), representing the agency in the European network for new materials (M-ERA program). Dr. Bernard Bonello participated as principal investigator or as group leader in several national and European research projects. He is the author or co-author of more than 100 peer reviewed articles and proceedings.



**Hossein Honarvar** is a postdoctoral researcher at JILA and the Department of Physics, University of Colorado Boulder (CU Boulder), USA. In 2018, he received his PhD from the Phononics Laboratory at the Smead Department of Aerospace Engineering Sciences, CU Boulder. He received his B.S. degree from the University of Tehran, Iran (2011) and M.S. degree from the University of New Mexico, USA (2013). In 2016, he received the Teets Family Endowed Doctoral Fellowship in Micro/Nano Systems at CU Boulder. His research involves fundamental studies of phonon thermal transport using atomistic theories and simulations in close collaboration with experimentalists.



**Leonard Dobrzynski** obtained his Doctorate from the University Paris, France. He started his scientific career as an assistant professor at the Catholic University of Lille, France. Throughout his career, he joined the Atomic Energy Establishment in Saclay, the National Centre for Scientific Research in Lille, the USA National Science Foundation, the University of California in Irvine, the Institute Laue-Langevin in Grenoble, the Spanish National Centre for Scientific Research in Madrid, and more. He is presently a CNRS Emeritus Research Professor at the University of Lille. He is editor of the Garland Handbook of Surfaces and Interfaces and of the Elsevier Interface Transmission Tutorial Book Series, co-founder of *Surface Science Reports*, and co-author of the books *Surface Phonons and Polaritons*, *Phononics*, *Magnonics*, and *Photonics*.



**Bahram Djafari-Rouhani** is an Emeritus Professor of Physics at the University of Lille, France. After his doctoral degrees (PhD in 1974 and Doctorat d'Etat in 1978) at the University of Paris-Orsay and a post-doctoral position at the University of Gent, Belgium, he held a research position at the French National Center for Scientific Research (CNRS). In 1985, he became Professor at the University of Mulhouse before moving to the University of Lille in 1990. He led a theory group on the modelling of wave propagation and elementary excitations in heterogeneous and nanostructured materials, with a particular focus on the topics of phononic crystals and acoustic metamaterials, optomechanics, photonics, and plasmonics. He has published more than 350 peer-reviewed papers and about 30 review articles and book chapters. He was involved in several European and national projects. He is a board member of the International Phononic Society (IPS) and was awarded the Bloch Prize at the conference Phononics 2013. Currently, he is a member of the editorial boards of *Physical Review Applied* and *Applied Sciences*.



**Mahmoud I Hussein** is the Alvah and Harriet Hovlid Professor at the Smead Department of Aerospace Engineering Sciences at the University of Colorado Boulder, USA. He holds a courtesy faculty appointment in the Department of Physics and an affiliate faculty appointment in the Department of Applied Mathematics, and he serves as the Faculty Director of the Pre-Engineering Program at the College of Engineering and Applied Science. He received a BS degree from the American University in Cairo, Egypt (1994) and MS degrees from Imperial College, London, UK (1995) and the University of Michigan–Ann Arbor, USA (1999, 2002). In 2004, he received a PhD degree from the University of Michigan, after which he spent a year and a half as a postdoctoral researcher at the same university, followed by two years at the University of Cambridge as a postdoctoral research associate. His research focuses on the dynamics of materials and structures, especially phononic crystals and locally resonant phononic metamaterials, at both the continuum and atomistic scales. He received a DARPA Young Faculty Award in 2011, an NSF CAREER award in 2013, and in 2017 was honored with a Provost's Faculty Achievement Award for Tenured Faculty at CU Boulder. He has co-edited a book titled *Dynamics of Lattice Materials* published by Wiley. He is a Fellow of ASME and served from 2014 to 2020 as an associate editor for the *ASME Journal of Vibration and Acoustics*. He is the founding vice president of the International Phononics Society (IPS) and in 2011 has co-established the Phononics 20xx conference series which is held every two years.